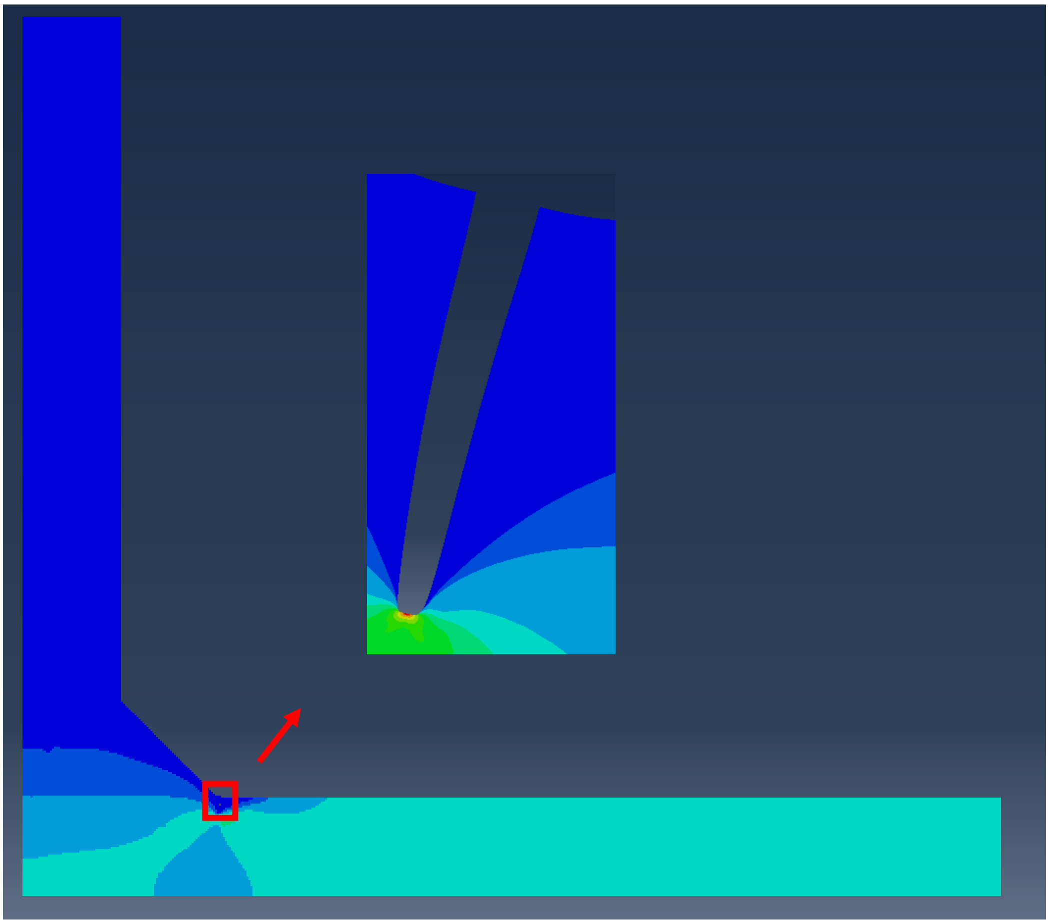

Influence of weld toe radius and steel grade on the fatigue life of fillet welds analysed by a strain based approach

Master's thesis in the Master's Program Naval Architecture and Ocean Engineering

GABOR GULYAS

Department of Mechanics and Maritime Sciences
CHALMERS UNIVERSITY OF TECHNOLOGY
Gothenburg, Sweden 2018

MASTER’S THESIS

Influence of weld toe radius and steel grade on the fatigue life of fillet welds analysed by a strain based approach

GABOR GULYAS

Department of Mechanics and Maritime Sciences
Division of Marine Technology
CHALMERS UNIVERSITY OF TECHNOLOGY
Gothenburg, Sweden 2018

Influence of weld toe radius and steel grade on the fatigue life of fillet welds analysed by a strain based approach
GABOR GULYAS

Master's Thesis
Department of Mechanics and Maritime Sciences
Division of Marine Technology
Chalmers University of Technology
SE-412 96 Gothenburg
Telephone +46 31 772 1000

Cover: Visual representation of geometry case with R=1 mm toe radius under 300 MPa nominal load, scaling factor 10

Gothenburg, Sweden 2018

Influence of weld toe radius and steel grade on the fatigue life of fillet welds analysed by a strain based approach

GABOR GULYAS
Department of Mechanics and Maritime Sciences
Division of Marine Technology
Chalmers University of Technology

ABSTRACT

The Thesis project deals with the fatigue life of fully penetrated fillet welds and the effects of the weld toe radius in two different steels such as HSS (High Strength Steel) and LSS (Low Strength Steel). A localised strain based approach was used for the fatigue strength assessment. This approach applies a step by step discrete crack growth simulation for the total fatigue damage process (crack initiation and propagation) within the LCF (Low Cycle Fatigue) and HCF (High Cycle Fatigue) range, respectively. The model considers the effects of the microstructure, i.e. hardness and grain size for the two material, and the toe radius (R= 1 mm and 0.01 mm).

Using Abaqus, the FEM analysis was carried out on a simplified parametric model of the fillet welds created with Matlab. The resulting stress and strain values were averaged using a characteristic length of the material, and the summation of the cycles, estimated by the Coffin-Manson relation for each discrete step, gave the overall fatigue life of the welded structure.

The predicted fatigue strength and the shape of the S-N curve for both materials are in line with expectations. However, due to the material model used, where the strain vs life curves of the two materials differ significantly in the LCF range but seem to be similar at HCF one, the resulting S-N curves differ. The smooth-weld, R= 1 mm without any initial cracks seem to have a higher FAT class for both materials, whereas the weld with R= 0.01 mm gave a lower FAT class than the IIW recommended values. Also, the long crack propagation rate is reasonably in line with the recommendations for fillet welds. The differences of the short crack initiation and propagation period are significant for the two materials, whereas the long crack propagation and final fracture showed fairly similar behaviour.

The initiation period in the presence of a larger toe radius, R= 1 mm lasts longer and is more dominant for the HSS material than for the LSS material. Hence, for this geometry, the HSS material could offer a better fatigue resistance. On the contrary, a smaller toe radius, R= 0.01 mm, or the presence of initial cracks of the size of 0.1 or 0.2 mm, seems to significantly lower the fatigue strength more for the HSS, than for the LSS weldments. This result shows the high dependency on the geometry, related to the actual material and implies that, due to the higher notch sensitivity of HSS, the fatigue strength will be lower for the R= 0.01 mm case than for the R = 1 mm. This tendency is not prominent in the LSS material.

Keywords*: fatigue, strain-based approach, short fatigue crack, propagation, fillet weld, weld radius, high strength steel*

ACKNOWLEDGEMENTS

I would like to take the opportunity to express my gratitude to my supervisors, Professor Heikki Remes and Professor Lennart Josefson for their ongoing support during the previous months. Without their valuable instructions, discussions and guidance I would not have the capability or the opportunity to dive into to topic. The comments and feedback I received from them helped me not only to finish the thesis but also to learn in depth and acquire a unique skill set towards a state-of-art fatigue assessment.

I would also like to thank Sami Liinalampi, for his eagerness and enthusiasm to help me on a daily bases with the beauty of Python and Matlab coding to run the simulations.

I am incredibly grateful for Jani Romanoff who selected me and gave the opportunity to pursue my studies within this unique, joint double degree program. As a Nordic Master student, I had the chance to study at Aalto University in Helsinki and Chalmers University in Gothenburg, I could not even have asked for better countries to live in. The knowledge and experience I have received from the professors and classmates, during this period of my life were extremely worth every decision I made in the past to come this far. No regrets, indeed one of my best decisions to carry on my studies in the Nordic countries.

I am thankful for Finland for always treating me nicely even during the cold and dark winter times, and the friends, adventures, and opportunities it gave me in during these two years. I would not even want to leave.

Last but not least, I would like to close these lines to thank and show my sincerest and warmest gratitude to my family, who were always there for me and their encouragement and never ending support to keep pushing me beyond my limits.

I can be only grateful for everything.

Thank you!

Gabor Gulyas

Espoo, 08.06.2018

TABLE CONTENTS

LIST OF FIGURES

LIST OF TABLES

NOMENCLATURE

Acronyms

Symbol	**Description**
EEDI	Energy Efficiency Design Index
HSS	High Strength Steel
LSS	Low Strength Steel
LCF	Low Cycle Fatigue
HCF	High Cycle Fatigue
LEFM	Linear Elastic Fracture Mechanism
CGR	Crack Growth Rate
EBSD	Electron Backscatter Diffraction
BM	Base Material
HAZ	Heat Affected Zone
TZ	Transient Zone
WM	Weld Metal
SAW	Submerged Arc Welding
HV	Vickers Hardness
IIW	International Institute of Welding
SWT	Smith Watson Topper
FEM	Finite Element Method

Roman Symbols

Symbol	**Description**
N_t	Total Failure Period
N_i	Initiation Period
N_p	Propagation Period
$l_{s,th}$	Small Crack Threshold Length
$l_{m,th}$	Macro Crack Threshold Length
a_0	Material Characteristic Length
a	Crack Length
a_c	Critical Crack Length
d	Average Grain Size
c	Fatigue Strain Exponent
b	Fatigue Strength Exponent
n	Cyclic Hardening Exponent
K	Cyclic Strength Coefficient
P_{SWT}	Damage Parameter
E	Young’s Modulus
n_0	Initial Discrete Step Number
R	Toe Radius
a	Weld Throat
z	Weld leg Length
S	Nominal Stress

k_t	Stress Concentration Factor
ΔK	Stress Intensity Factor Range
K_{IC}	Critical Fracture Toughness
TH	Stress Triaxiality
R_σ	Load Ratio

Greek Symbols

Symbol	**Description**
$\Delta\varepsilon$	Strain Range
ε_a	Strain Amplitude
$\sigma_f^{'}$	Fatigue Strength Coefficient
$\varepsilon_f^{'}$	Fatigue Strain Coefficient
σ_e	Effective Stress
σ_y	Yield Strength
σ_u	Ultimate Tensile Strength
ε_{el}	Elastic Strain
ε_{pl}	Plastic Strain
α	Flank Angle
σ_{max}	Maximum Stress
σ_{min}	Minimum Stress
σ_m	Mean Stress
σ_r	Residual Stress

1 INTRODUCTION

Nowadays the maritime industry plays a significant role in the economy, due to that over the 90% of the world's trade is done on seaways [1]. Further, this mean of transport provides the most cost-effective way to move freights around the world. Not only the merchant shipping but the luxury cruising industry is significantly increasing with secured orders with the largest shipyards for the upcoming 10 years and also aiming to build larger and larger vessels to be able to accommodate more customers on board [2], [3].

From a ship owner's perspective, the turnover time of the invested financial plays a vital role in the 'equation' when building a vessel. Essentially the more freight can be transferred during one leg, the better. For a vessel with set main dimensions and displacement, this can only be achieved by increasing the deadweight capacity, hence lowering the lightweight of the ship. Furthermore, the energy efficiency of the ship can be improved while maintaining the load carrying capacity, by introducing a lighter structural solution. Subsequently, under the current environmental rules and regulations, this would indirectly result in a lower Energy Efficiency Design Index, (EEDI). Hence a more energy efficient vessel with a lower CO_2 footprint [4].

Weight reduction can be achieved by high strength steel (HSS), thinner plate thickness or both. However, for the application of HSS different other factors also play an important role as well, especially when considering production and fatigue strengths under cyclic loading. The application of different weld techniques would result in varying weld profiles and rather sharp notches in case of low-quality welds. The latter combined with high strength steel (HSS), having higher notch sensitivity could practically eliminate the actual potential of HSS application for better fatigue design. On the other hand, with the determination of the optimum parameters for weld geometry could lead to a beneficial fatigue life of HSS without the application of any post- weld treatments.

2 FATIGUE OF WELDED JOINTS

During the building of hull structure and production stage of a vessel, welding of metallic structural components is applied, this includes welding of steel plates and girders through the entire cross-section of the hull. This production process provides multiple structural design options that could not be simply carried out with other production techniques. However, this production technique is also associated with various problems that are only recognisable for welding, related to different welding techniques used primarily during shipbuilding. Such methods can include plasma arc welding, submerged arc welding, metal active gas welding, laser-hybrid welding or conventional arc welding [5] [6].

These welded structural members or components continuously exposed to cyclic loading will experience degradation of mechanical properties leading to ultimate failure. Fatigue behaviour is a problem that affects the moving structural components of the vessel, for instance, the hull itself being constantly subjected to wave-induced cyclic loads on the high seas, which would define the nominal stress range, during the design stage.

Furthermore, it is estimated that 90% of service failures of the welded hull structural components that undergo a movement of one form or another can be attributed to fatigue [7].

The mechanical and geometrical properties of the weld joint, such as notch radius, flank angle, undercut depth have a substantial effect on the fatigue damage. Therefore the different welding techniques and quality would result in a scatter of the fatigue strength of individual structural members [6]. The actual geometry of the weld of a joint would further increase the local notch stress and strain levels [8].

When it comes to the application of high strengths steel, HSS (with fine-grained structures, case hardened) manufacturing process, as well as high requirements, are particularly important. The name, as in ‘high strength’ only refers to the static strength of a smooth specimen and under alternating or pulsating loading with low-quality welds, having sharp notches, combining with the higher notch sensitivity of the material would eliminate the potential application in shipbuilding for better fatigue resistance [9]. Thus, it seems that with higher quality welds with less notch effect could lead to the beneficial use of HSS without the application of post-weld treatments. However, there is still a lack of knowledge about weld quality effect regarding the crack initiation period of the fatigue assessment.

2.1 Fatigue Assessments

Fatigue of welded components is a very complex process. The material properties are strongly affected during the production by the heating and the followed cooling. Further, the presence of additional material through the fusion process would result in inhomogeneous and different materials. Also, a low-quality weld could contain flaws such as pores, undercuts, inclusions, which would further contribute to high-stress concentrations.

Due to its complexity and the vast area of application, currently, several approaches exist towards fatigue analyses of welded joints [10] [11]. A summary of several approaches can be seen in Figure 1, showing the assessments based on different parameters.

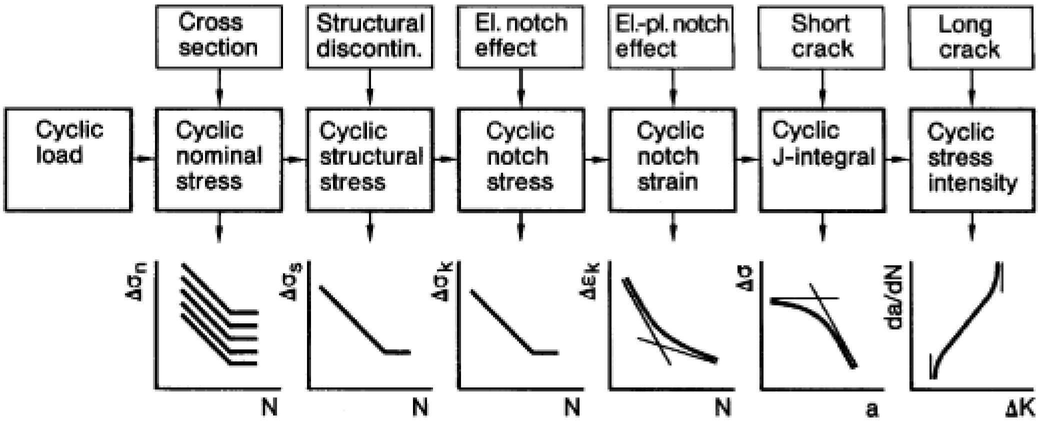

Figure 1. Several approaches to fatigue assessment with different input parameters [12]

These approaches can be categorised as follows:

a) Nominal Stress approach [13] [14]; which requires defining the nominal stress, based on the loading conditions as well as the cross-sectional area of the material. It is then further to be assessed against its permissible value concerning a corresponding classified structural detail, i.e. FAT class; see, e.g. IIW [13]

b) Hot Spot Stress approach [13] [14]; the stress increase effect of the structural discontinuity is taken into account, and extrapolation is being made based on the stress levels at specific reference points away from the weld

In case of a more complex structural detail, a local approach should be applied to consider the weld shape effect. This effect could not be described accurately by a global structural approach since the fatigue process has mainly local characteristics. This challenge can be overcome with local concepts, which may be linked to the following groups [12], [15] :

c) Notch Stress approach [13] [14]; a toe radius, R=1 mm is introduced, and further compared with a FAT class 225

d) Plastic strain energy based model on fatigue life estimation in the LCF regime [16]

e) Notch Strain approach [12] [14]; consideration of local elastic-plastic stress-strain and the supporting effect of the surrounding elastic material, i.e. plane strain condition in the low cycle region ($<10^5$) and traditionally used for the initiation time only [17]

f) Crack Propagation approach [17]; particular parameters of the material are used to describe the increase of the crack length during each cycle but requires an initial crack

However, for the notch stress approach, the crack growth cannot be modelled explicitly and does not consider the material effect on the fatigue crack growth since notch stress S-N curve only presents the total fatigue life and analysis is linear elastic. On the other hand strain energy or strain approach is used to estimate crack initiation. Thus, these local approaches would result in different accuracies of the fatigue assessment [15], so a good understanding of design principles and the purpose, i.e. *damage tolerant design*, *infinite life design*, *safe life design*, *fail-safe design* [7], as well as the fatigue damage process, is imperative.

Furthermore, these assessments can be categorised into Low and High Cycle Fatigue, LCF, HCF. The first three approach listed above from *a)* to *c)* are mainly in connection with the HCF period, whereas a strain based approach could be better utilised for the LCF region.

2.2 Fatigue Damage Process

The fatigue crack formation is divided into different stages [7] [10]. These processes, as seen in Figure 2, includes mainly microstructural phenomena, however, could be further approximately described based on the macroscopic elastic or elastic-plastic stress and strain analyses, which would refer to initiation and propagation of the ‘technical crack’.

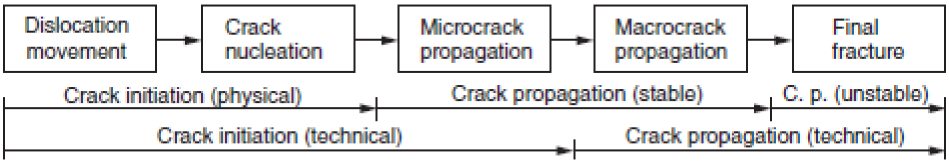

Figure 2. Micro and Macro crack phenomena [12]

The total failure time based on the crack damage process in Stage I - III comprises of the initiation and the propagation period, as seen in equation (1).

$$Nt = N_i + N_p \tag{1}$$

The crack initiation period involves, short crack nucleation, the growth of short cracks up to a threshold length $l_{s,th}$, further the propagation of short cracks on a microstructural level up to a macrocrack threshold length $l_{m,th}$, i.e. ‘technical crack’ length. The initiation phase is then followed by the macrocrack propagation up to a length of a final fracture. The threshold length of the short crack is defined as the smallest crack size that has a stable and measurable crack growth rate and observed to be around three times the grain size of the material [14] [18]. Whereas in the next period the length of the macrocrack threshold, i.e. technical crack is around 0.1 – 0.2 mm [14] [18].

Previously, to describe the initiation period, different theoretical experiment-based models were applied and considered [18] [19]. Furthermore, important issues need to be also considered such as the effect of crack closure, the size of the damage zone, stress state three-dimensionality and notch tip plasticity.

Analysis of the welded joints under the strain-based approach would mean describing the crack initiation by the Coffin-Manson equation [20] and the phase followed by the long crack propagation is typically modelled separately with the Paris-law, governed by fracture mechanics parameters (LEFM) [17].

Preliminary assessment of this initiation phase can be described by the local notch strain approach as mentioned in Section 2.1. This approach was also later further developed, to take into account the short crack initiation as well as the short crack propagation aspects [11] [12]. An evolution of the local approach assessments, including primary and more advanced methods, can be seen as follows:

a) Initiation prediction with notch consideration, considering Neuber’s correction [9], [12], as follows in equation (2):

$$\sigma\varepsilon = \frac{(K_t S)^2}{E} \tag{2}$$

b) Initiation and short crack propagation prediction based on the Coffin-Manson approach, as per the following equation (3) [17], [21]:

$$\varepsilon_a = \frac{\sigma'_f}{E}(2N_f)^b + \varepsilon'_f(2N_f)^c \tag{3}$$

c) Total life, i.e. initiation and propagation prediction of a welded joint with a rounded notch shape, with a finite radius ρ* constant, based on Glinka’s approach [22]
d) Total life prediction with an arbitrary weld notch shape, based on discrete crack growth in a highly stressed volume that takes into account the material parameters on a microstructural level [21]. The approach also utilises the Smith Watson Topper damage parameter due to the mean stress effect [23]. However, it should be noted that, in unnotched specimens with a smooth surface, or in the presence of a properly optimised, high-quality weld joint with a fine geometry, most of the total fatigue life might be consumed mainly in microstructural crack initiation. On the contrary, traditional weld joints with sharp notches could potentially lead to a very short initiation time and crack propagation time would dominate the total fatigue life. Nevertheless, during the initial microcrack growth, the growth rate is rather still low, which could further expand and

cover a significant part of the fatigue life, hence a good understanding of the initiation period and the utilisation of advanced local methods are necessary.

A schematic development of the crack growth rate as a function of the allocated fatigue life can be seen in Figure 3. On the schematic figure, it can be seen the different periods, i.e. micro and macro cracks regarding the crack length, and how the presence of different initial crack lengths would influence the initiation and propagation time of the total fatigue life. However, to this date, the question remains how Figure 3 and its different phases of the fatigue damage process can be related to the weld shape effect and the different material parameters.

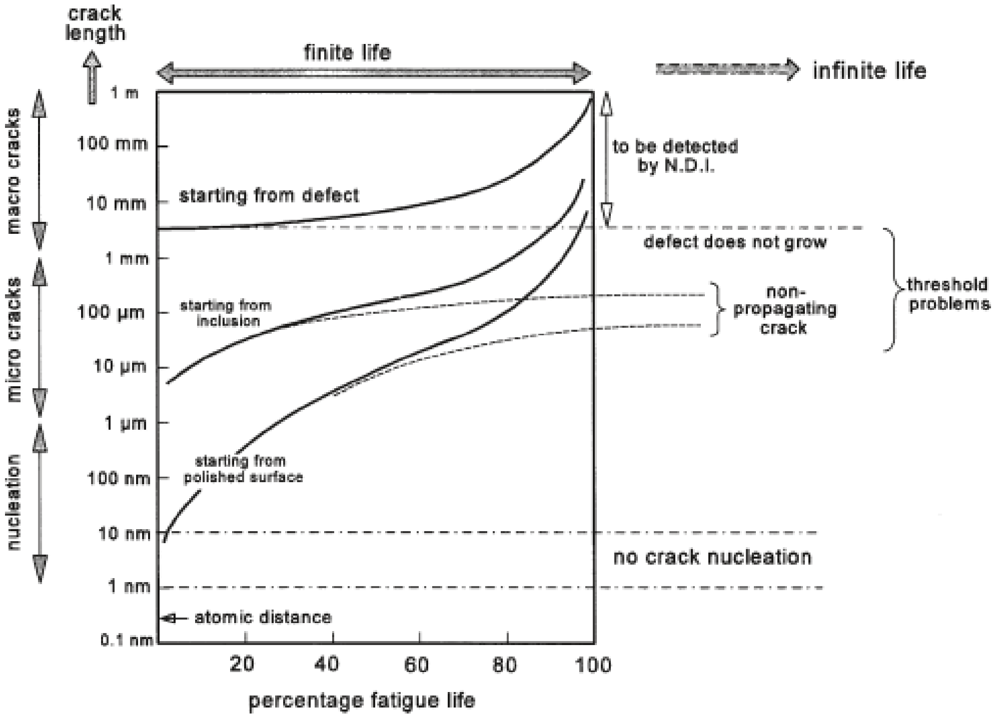

Figure 3. Different crack growth behaviour patterns compared to the fatigue life [7], [24]

2.3 Scope of work

As mentioned in Section 2.2 the crack initiation period plays an important role under different material, loading and surface conditions and it could also cover a significant part of the fatigue life. These surface shape effects due to the influence of welding, i.e. notches are taken into account at a certain level in different assessment approaches.

The application of the continuously developed and improved high-performance welds, with a smooth weld shape could lead to an expanded fatigue life in notch sensitive materials such as HSS. Therefore it would require particular attention to carefully analyse the initiation time of the crack, due to the change of weld shape and the different material parameters.

To analyse the welded specimens and the effect of the material parameters the latest discrete crack growth approach is being utilised based on the findings from H. Remes [18], [21], as mentioned in Section 2.2 *d)*. This approach was previously used on butt welds [18], [21].

However, the current study tends to expand those findings and utilise the approach on different welded structures.

Subsequently, the thesis project primarily focuses on fully penetrated fillet welded specimens with different geometries, as illustrated in Figure 4, and their influences on the fatigue life of HSS and LSS material models, respectively.

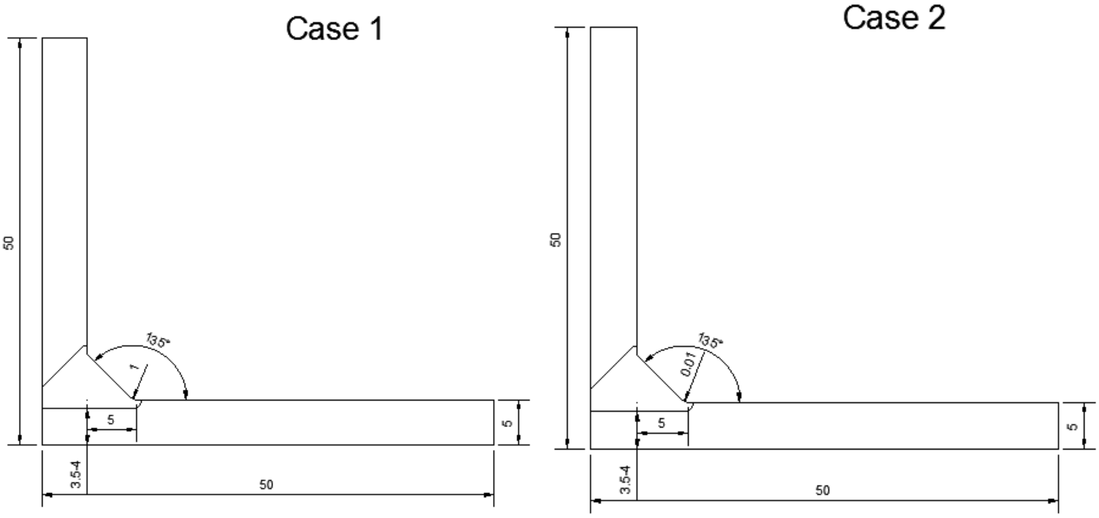

Figure 4. Weld geometries under consideration

Case 1 geometry model offers a smooth transition with a large toe radius of *R= 1 mm*, whereas Case 2 geometry has a smaller, more realistic radius of *R= 0.01 mm* that essentially acts as a notch. These geometries have significant effects on the stress states. Hence they can directly influence the crack initiation and propagation period, which will be considered using FE software, Abaqus.

A simplified FEM model will be created that should also take into account the different material zones and distribution, due to the heat effects from the welding procedures, and their influence on the behaviour of the fatigue damage process.

Based on the current stress and strain state for each material and geometric model the number of cycles will be estimated using Matlab based on the Coffin-Manson formula, considering the different load cases and their allocated mean stresses, as well. The fatigue strengths results including LCF and HCF ranges will be compared to the fatigue behaviour of the two materials for each weld geometries.

3 STRAIN-BASED APPROACH WITH ARBITRARY NOTCH SHAPE

In the case of high-performance welds with smooth geometry and less crack-like defects, hence considering the actual shape of the joint, the initiation time becomes more critical. A significant difference can be realised in fatigue lives when considering this initiation phase into the design compared to other approaches that are only taking into account the crack propagation phase [6], [15], [21], [25].

Recently the consideration of the local elastic-plastic response was further extended by a continuum model. This model also includes the effect of the microstructure of the material for the crack growth response [21], [26], by utilising the fundaments of the Coffin-Manson equation, Neuber's rule [17], Hall-Petch strengthening [27].

3.1 The methodology of the damage process

In this discrete crack growth approach [21], [26] the damage processes are being modelled in a damaged zone, i.e. volume related to the microstructure of the material as a repeated, continuous crack initiation. Within this finite material volume the stresses and strains are averaged, and after dislocation movements forming slip bands [17], short cracks nucleate and propagate to a macrocrack threshold length, $l_{m,th}$, throughout the grains of the material. These grain sizes and shapes vary and statistically distributed. Furthermore, the individual grains and their actual position is not known [28]. Therefore, homogenization is needed on the microstructural level, related to the influence of the individual grains on the behaviour of the material volume. This is done based on the strength of the material, provided the crack damage process follow the weakest link scenario [26].

According to the Hall-Petch relation, in equation (7), low strength is related to large grain size [26]. Therefore the minimum averaging length used to average the stress and strain values is equal to the maximum grain size. This would further result describing the size of the damage zone by the upper limit of grain size distribution. Including the statistical variation of the grain sizes within the material, this damage zone can be described as the material characteristic length a_o as seen in Figure 5. and in equation (4).

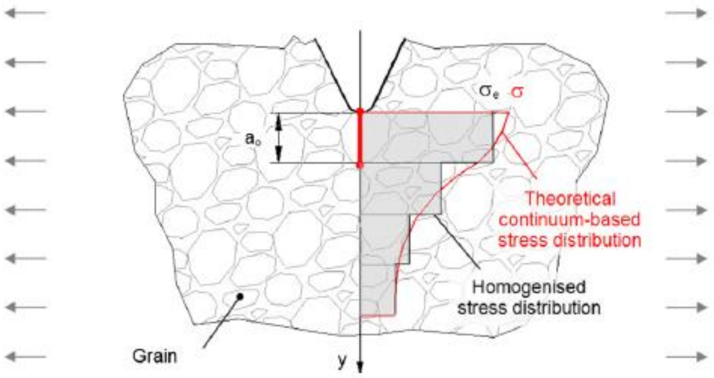

Figure 5. Averaged stress length within the grain-based homogenization unit [26]

$$a_0 = c \cdot d \tag{4}$$

where d defines the averaged grain size and the parameter c is dependent on the statistical variation of the grain sizes. The latter during the study is considered, c=1.

Furthermore, this a_o characteristics length determines the length of the individual steps, n of the discrete short crack growth and the allocated number of load cycles, N_{in}. The number of load cycles for each of the discrete step growth can be calculated based on a further developed Coffin Manson equation that also considers the mean stress effect [17], which equation is described in details in Section 6.2. The fatigue characteristic material parameters in equation (3), such as E, $\sigma_f{}'$, $\varepsilon_f{}'$, b, c has to be known, and will be described in Section (4).

Finally, under these principles, the total life of the final fracture N_t is the sum of the load cycles related to the individual crack growth steps n. Furthermore, based on the characteristic length a_0 an allocated crack growth rate, CGR_n can be defined for each of the discrete steps as seen in equation (5), as well [26].

$$CGR(a) = \frac{a_0}{N_{in}(a)} \tag{5}$$

3.2 Modelling of initiation and short crack growth

Due to its extremely localised phenomena of the stress and strain around the weld notch, the damage processes limited only to the homogenisation unit, i.e. where the area of highest stress applies [26]. According to Section 2.2, the crack initiation involves the coalescing of microcracks, resulting in the short crack, which process takes place within the damage zone. In case this process repeats itself, it would yield the growth of the crack with the increment of each step equals the material characteristic length, $a_{o,}$ as seen in Figure 6 [26].

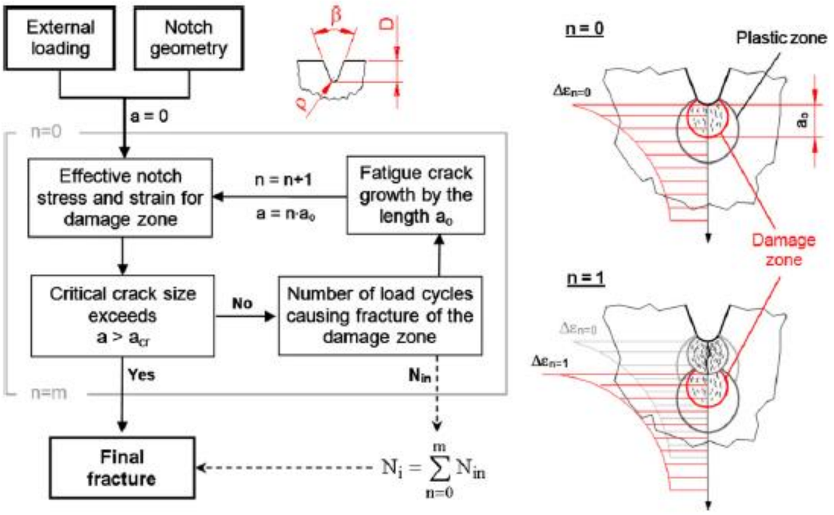

Figure 6. Damage process modelling [26]

The initial stage n_0 of the damage process is modelled with the actual geometry of the weld, including notch size, without any cracks. Cracks usually start initiating at points where peak stresses are present. After the fracture, each of the consecutive steps of the damage analyses is carried out at the new crack tip, and the discrete growths are repeated until the critical crack length is reached that is related to the material parameters, i.e. fracture toughness and the geometry of the material in question [17].

The fatigue crack typically grows in the direction of the maximum principal stress [18], [29], which direction can vary highly according to the weld type, geometry and loading conditions. This direction of the principal stress is an average of all the values within the highly stressed volume of the damaged zone, where the stress higher than 80% of the maximum stress is taken into account [18] [12]. Also, the direction tends to change during each of the discrete crack growth as seen in Figure 7, [18]. Thus the direction would need to be calculated for each of the individual discrete crack growths.

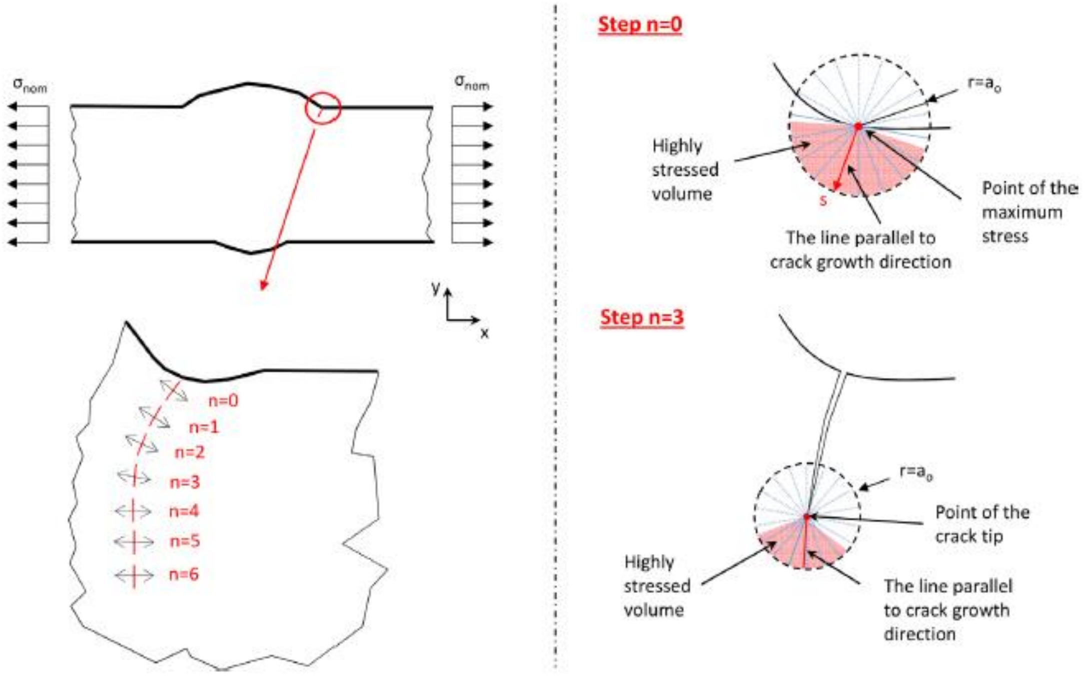

Figure 7. Crack direction change in case of a butt weld [21]

The response of the material is described by the stress such as σ_{eq}, σ_{33}, σ_{22}, σ_{11}, σ_{xx}, σ_{yy}, τ_{xy}, and strain values averaged within the characteristic length, which is obtained by utilising the line method [18]. These averaged stresses, i.e. effective stress is calculated in equation (6).

$$\sigma_e = \frac{1}{a_0}\int_0^{a_0} \sigma ds \tag{6}$$

4 MATERIAL PROPERTIES

A good understanding of the material and its properties under different conditions is necessary for an adequate and comprehensive structural design. As mentioned previously in Section 2.2, the fatigue damage process is split into two periods, i.e. crack initiation and propagation. Therefore it is significant to consider the two periods separately since several material properties and conditions might have different influences on each of the damage process. Also, several surfaces, the environmental condition might influence the initiation period differently, as well compared to the propagation period.

On the other hand, the transition period between initiation and crack growth cannot be quantitatively described. Under basic terms, the propagation starts if the crack growth resistance is controlling the crack growth rate [7]. Due to the transmission depends on microstructural barriers of the material, the size of the microcracks can significantly vary from material to material and be different between low and high strength steels.

This local strain is mainly based on the Coffin-Manson formula as mentioned in Section 2.2 hence the following variables have to be known for fatigue analyses:

- E – Young's modulus
- $\sigma_f{}'$ - fatigue strength coefficient, analogous to the true facture strength and usually somewhat higher than the ultimate tensile strength of ductile materials
- $\varepsilon_f{}'$ - fatigue strain coefficient
- b – fatigue strength exponent
- $c-$ fatigue strain exponent

- n - cyclic hardening exponent,

- K – cyclic strength coefficient,

Some of the parameters can be determined through either monotonic or cyclic tensile tests, which would result in accurate values of the variables. However, in lack of cyclic test opportunities, estimation of the variables can be made based on the material hardness and tensile strength [30], [31].

4.1 Microstructural characteristics, grain size

Fatigue can occur under stress amplitudes below the yield stress that is related to cyclic plastic deformation, i.e. dislocation activities, limited to only a small number of grain size of the material [5]. Since the material on the surface is only constrained with surrounding material on one side, this micro plasticity can already occur in grains on the free surface at lower stress levels, contrary to grains in the subsurface region.

On the microscale level, the stress can differ from grain to grain, based on their size and shape, orientations and the elastic anisotropy of the material. Thus for simplicity and modelling purposes, the isotropic condition is assumed, furthermore as per Section 3 homogenization of the material is needed [5] [21]. It should also be noted that strain hardening can be experienced in the slip band. Hence the hardening parameters of the parent, as well as the weld material need to be adhered to.

Grain size is an essential parameter in regards to an average short crack growth rate *da/dN*. Especially fine or ultrafine-grained steels, prepared by mechanical alloying with consequent consolidation or techniques of severe plastic deformation, could exhibit exceptional mechanical properties on fatigue behaviour [32]. This strength relation is described by the Hall-Petch relationship [32], seen in equation (7).

$$\sigma_y = \sigma_f + k \cdot d^{-1/2} \tag{7}$$

where σ_y represents the yield stress, σ_f the friction stress, k is a constant and d describes the average size of the grains.

The total fatigue life, N_f in the strain-based approach is defined by, the Coffin Manson formula for the low cycle fatigue (LCF), ($\Delta\varepsilon_{el} \leq \Delta\varepsilon_{pl}$) regime, governed mainly by the fatigue ductility, as well as the Basquin equations for the high cycle fatigue (HCF) ($\Delta\varepsilon_{el} \gg \Delta\varepsilon_{pl}$) controlled mainly by the fatigue strength, as seen in equation (3) [17]. Based on the fact that materials with finer grains *(1* $\mu m > d > 100\ nm$*)* shows higher strength in contrast to materials with conventional grains *(*$d \approx 100\ \mu m$ *or larger)*, however the latter material tends to have a larger ductility, which can be seen in Figure 8 in the total strain fatigue life diagram for each of the allocated regimes.

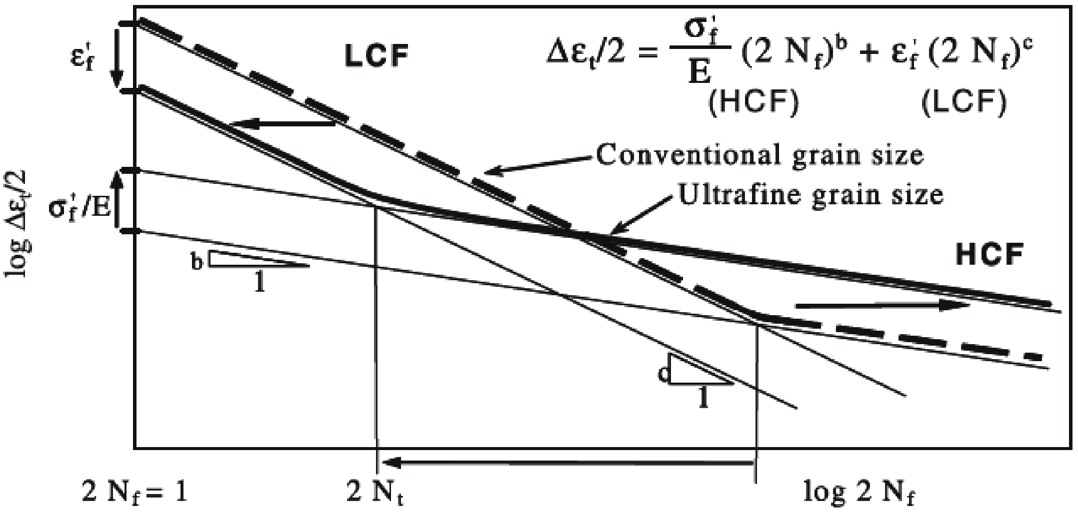

Figure 8. Strain vs the life of fine and conventional grain sized materials [32]

It can be noted from Figure 8 that grain sizes would have different resistance and influence within the crack initiation as well as later in the crack propagation period. It indicates that materials with larger grains that exhibit higher ductility and lower hardness would offer better endurance and resistance for the crack initiation period in the LCF regime. Materials with finer grains could exhibit an overall longer fatigue life, and increased endurance for stress controlled cyclic loading. For the latter, notch sensitivity would also be increased with the finer grain sizes [33]. Thus a high-quality weld geometry would be of importance.

Further, the damage process can also highly depend not only the average size of the grains but on its distribution and the grain boundary structure, i.e. low-angle vs high angle grain boundaries [34]. Thus, strain-based approach with volume-weighted average grain sizes d_v [27] also gives good estimation at least for LSS.

The estimation of d_v of the base material can be done with a Matlab measurement code [35] for the microscopic Electron Backscatter Diffraction (EBSD) image analysis, as seen in Figure 9. The microstructural parameters of the S690 were also compared to lower strength steel such as S355.

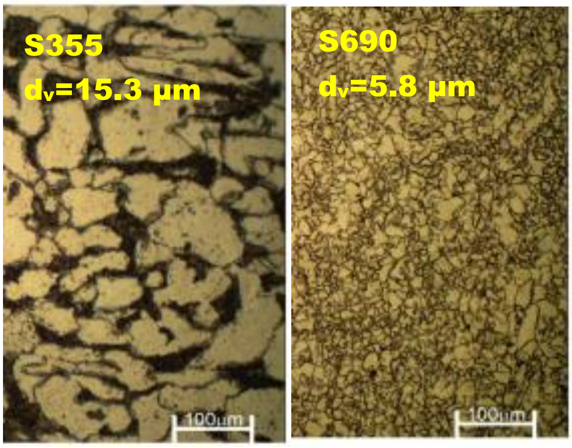

Figure 9. Quality map of the base material HSS and a based material of LSS [36], grain sizes at a probability level of 99%

It can be noted that High Strength Steels (HSS) tend to have finer grain sizes, compared to Low Strength Steel (LSS) materials, this could also indicate better resistance to crack initiation for HSS. This grain size parameters would even increase further for S275 steel.

Nevertheless, studies [34] [37] [38] [7] [33] also show, that increasing the refinement of the grain sizes would further result in lowering the fatigue thresholds for a particular specimen and enhancing the crack growth rate in the propagation region.

4.2 Welding influence

During the localised fatigue assessment the chemical composition of the filler metal, as well as the welding procedure, should also be taken into account for an adequate analysis. Different welding procedures would yield significant variation in the heat affected zones, as well as in the induced hardness around the joint. In case of a fully penetrated fillet welded joint, as seen in Figure 10. a higher quality weld as in a laser or hybrid opposed to an arc welded joint would result in a narrower weld, heat-affected zone (HAZ), as well as transient zone (TZ). The current study does not clarify and compares different welding procedures, neither weld metals used, instead focuses on the actual geometry impact of the welded joint. However, the following generalisation and simplification can be considered for localised fatigue assessment purposes, regarding the influence of the welded joint.

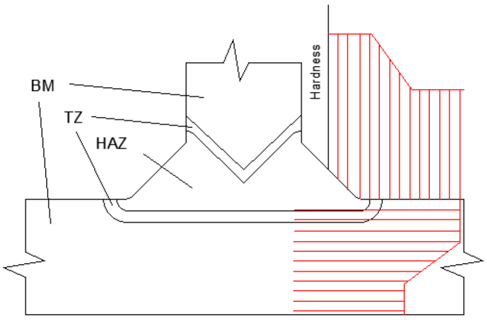

Figure 10.Material zones; base material (BM), heat-affected zone (HAZ), and transient zone (TZ)

In general, when high strength steels are welded, due to the generated heating and cooling in the weld and base metal, it can generate harder heat affected HAZ, cold crack susceptibility and residual stress thus affects the microstructure. The influence of the latter one on the loading condition will be discussed in detail in Section 6.

Depending on the grade type of the BM and the welding technique the HAZ subject to failure, since hydrogen induced cracking is more pronounced across this zone [39]. A higher heat input leading to a slower cooling rate results in coarse grain in the HAZ and the reduction in carbon content would also further increase the resistance to hydrogen induced cracking [40]. In contrary lower heat input, i.e. fast cooling rate coupled with the weld production related mechanical action would result in a finer microstructure. Within these zones based on the heating and cooling rates, phase transformation can also occur that could lead to lower hardness in the different regions [41].

Particular chemical composition of the filler metal could also lead to an increased yield strength of the WM, compared to the BM, since some of the forming elements such as *Nb*, *Ti*, *V* etc. can have limited solubility in ferrite and austenite. This could mean contributing to strength due to precipitation hardening [40].

A high-quality SAW [42] welded joint of *S700MC* is considered and assumed to be free from any macro-level defects. The heat-induced microstructure of the variable region, i.e. BM and HAZ can be seen in Figure 11. The measurement of the grains in HAZ also indicated considerably larger than in BM.

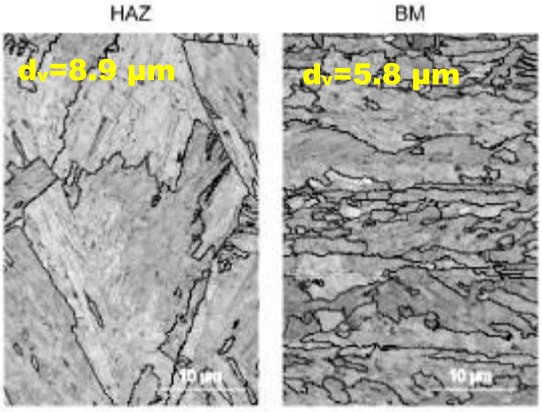

Figure 11. Quality map of the grain sizes in HAZ compared to BM [43]

According to the scaled hardness distribution [21], the individual material properties of the HAZ and TZ can also be estimated, based on the material properties of the weld and base material, respectively. These gradual changes of the material properties from WM to HAZ then can be modelled accordingly. However it should be noted, that the sizes of the actual different material regions affected by the heat, not only depends on the welding technique but also on the geometry of the fillet weld, i.e. flange angle.

Grain measurements and hardness tests were also carried out, on a butt welded S700MC specimen [43]. The measured through-thickness microhardness distribution for the HAZ region of the specimen around the weld can be seen in Figure 12. The average hardness of the HAZ seem to be somewhat lower, 271 $HV_{0.5}$ compared to the BM. Furthermore, the strain-based parameters of the HSS material were determined through cyclic tensile tests [43].

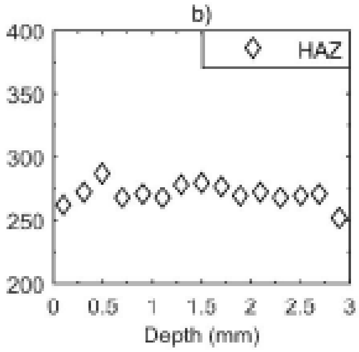

Figure 12. Hardness distribution in the HAZ region [43]

A summary of the HSS compared to LSS material parameters can be seen in Table 1, Figure 13 and Figure 14, respectively. For further comparison, the HSS parameters were estimated also based on the hardness of the material as seen in Table 1 and Figure 15.

Table 1. Material parameters for the HSS and LSS base material and heat affected zone, adapted from [26], [43]

Property	**BM/HSS**	**HAZ/HSS**	**BM/LSS**	**HAZ/LSS**	**Unit**
Young`s modulus E	220		210		
Poisson ratio υ	0.3		0.3		
Yield Strength σ_y	750	798*	287	346	MPa
Tensile Strength σ_u	810	930*	370	410*	
n	0.077	0.131	0.143	0.144	-
K	1353	1456	794	906	MPa
b	-0.064 [-0.0556*]	-0.061 [-0.0792*]	-0.083*	-0.084*	
c	-0.961 [-0.722*]	-0.871 [-0.6042*]	-0.583*	-0.581*	
σ'_f	1174 [1393*]	926 [1373*]	782*	1105*	MPa
ε'_f	9.643 [0.3696*]	3.187 [0.3954*]	0.632*	0.495*	
Hardness ($HV_{0.5}$)	290	271	131	207	
Average grain size, $d = a_0$	5.8	8.9	15.3	18.5	µm

**hardness based estimation*

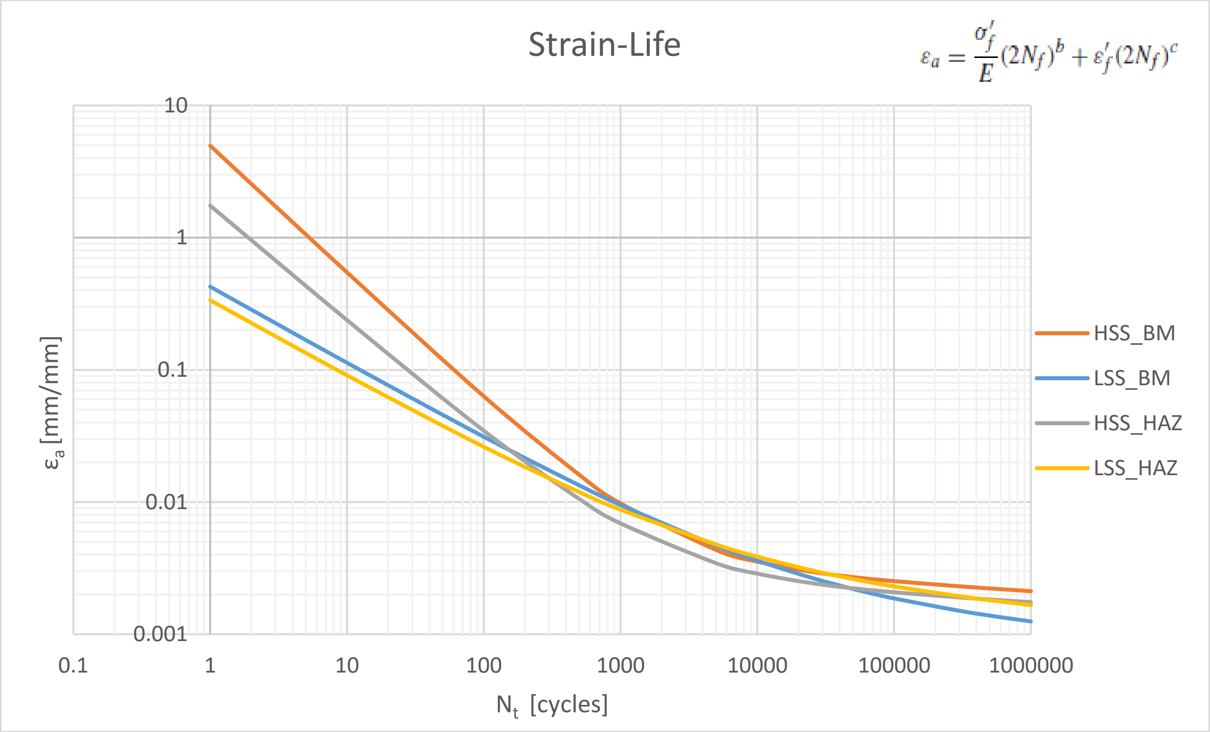

Figure 13. Strain-life (number of cycle to failure) curve of HSS and LSS, using HSS parameters based on full-scale test measurements

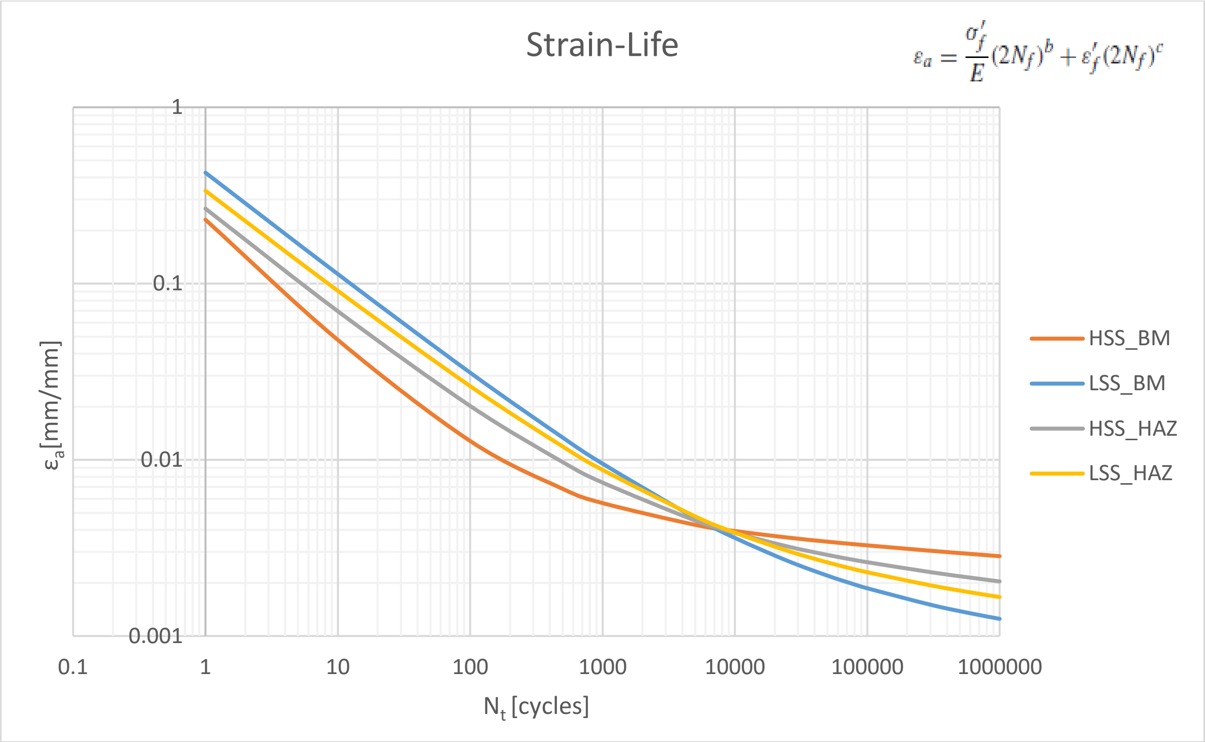

Figure 14. Strain-life (number of cycle to failure) curve of HSS and LSS, using HSS parameters based on Hardness based estimation

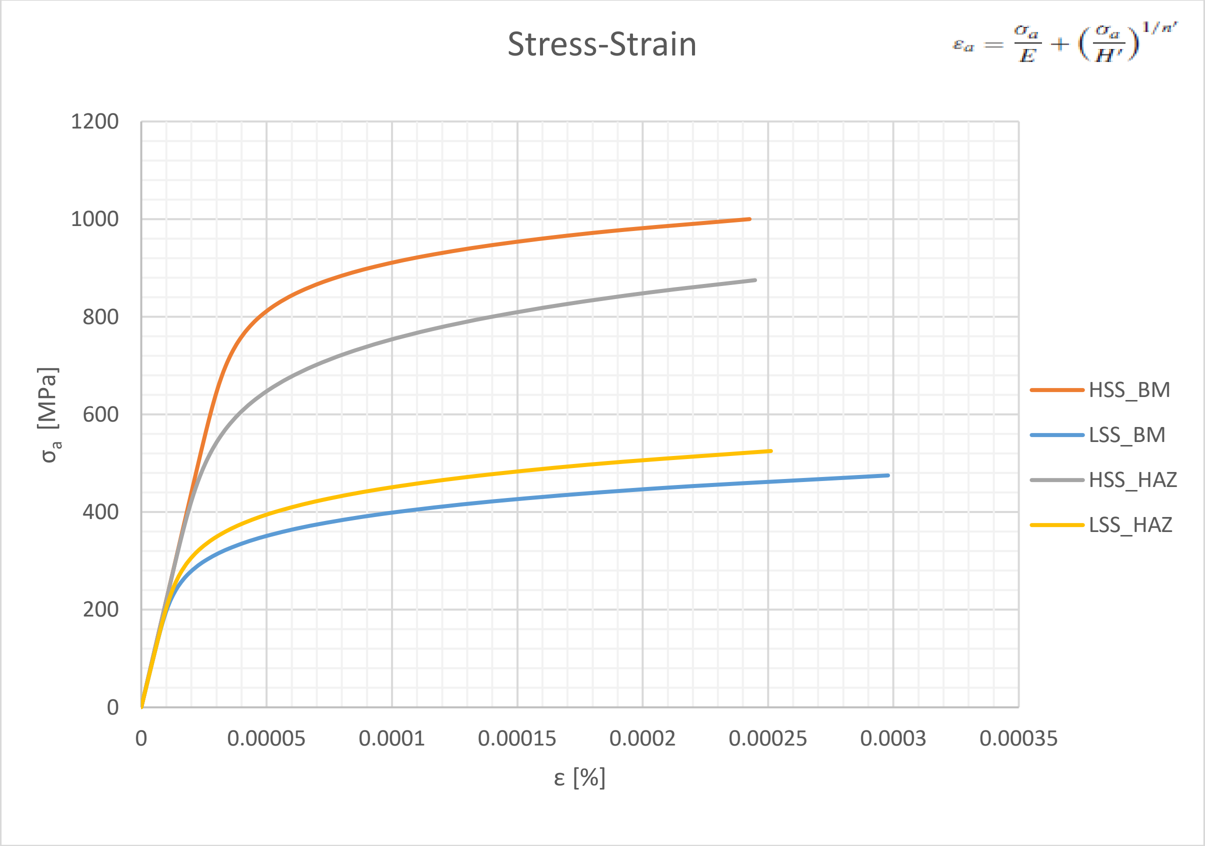

Figure 15. Strain vs Stress curve of HSS and LSS

5 WELD AND JOINT GEOMETRY

Two common practical welding types that can be distinguished for structural as well as different design considerations are the butt and fillet welds.

Applying the latter in structural components would lead inherently to a more complex and sever change in shape and structural discontinuity, which may increase the general stress concentration in addition to the local weld shape effect. Subsequently, it can be expected that fillets welds are more sensitive to loading conditions that could lead to fatigue damage, than butt welds. Fillet welds can be divided into two specific categories such as non-load carrying and load carrying joints, as seen in Figure 16. The scope of the thesis mainly focuses on the fatigue damage process of non-load carrying fillet welds, i.e. attachment welds that are not transmitting any significant part of the loads in the main structural members.

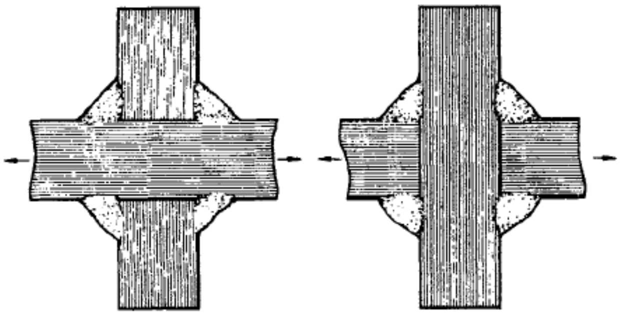

Figure 16. Non-load carrying and load carrying fillet welds [44]

Changing the weld shape and its properties, as seen in Figure 17, would affect the load transfer, throughout the attachment, which may cause an increase or decrease in stress concentration at the weld toe or root. In the current case, i.e. a plate with fully penetrated fillet welds, the highest stress concentrations will occur at the weld toe, and a crack is expected to initiate at one of them.

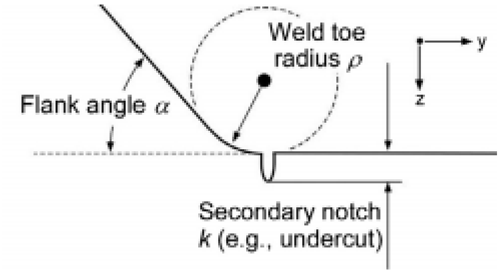

Figure 17. Weld geometry properties [45]

This damage process is influenced by the shape of the fillet weld, the depth of the undercut in the plate at the weld toes and the plate thickness. At the welds, geometry is the primary factor that controls the fatigue damage process of the cruciform joint. Using a high-quality laser welding procedure would result in an improved weld shape, which could further reduce the stress concentration and have a beneficial impact on the crack initiation as well as propagation time, without the need of post-weld treatments [46].

5.1 Fillet weld size

In practice, a weld size should be calculated of the joint structure, based on the material, welding procedure, applied load that is expected to carry, and so on. Therefore, in theory, sizes and shapes for non-load carrying full or partial penetrated joints can be any variations that the designer specifies. However, international standards [47] tend to guide practical limitation for both minimum and maximum throat thickness, as seen in Figure 18 and Table 2, respectively.

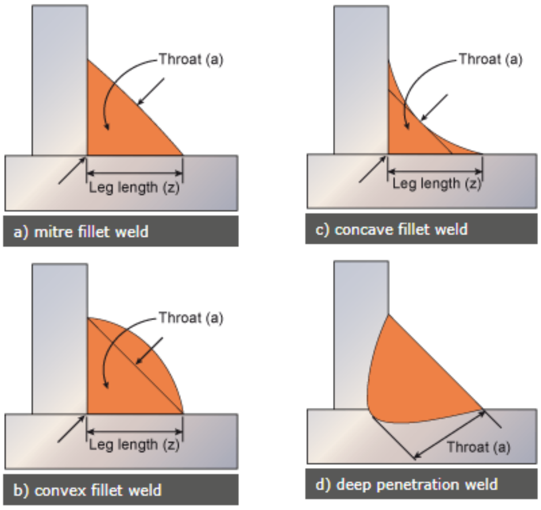

Figure 18. Throat dimensions [47]

Table 2. Minimum practical dimensions [47]

Plate Thickness [mm]	**Minimum size of leg length [mm]**
≤ 6	3
$6 < t \leq 12$	5
$12 < t \leq 20$	6
$20 <$	8

Minimum values are usually governed by the production method to allow adequate fusion into the base metal, whereas the maximum size is that of the thickness of the thinner of the two plates joint together.

5.2 Effect of weld shape on fatigue

In practice, different application of welding procedures, i.e. filler metal, operation speed would lead to significant variation in shapes. Ideal weld geometry would yield a stress concentration close to unity. However, this could require significantly low speed and high amounts of filler metal, which production-wise would be unrealistic [46]. The aim is to find a balance between desirable weld profiles with practice as well, which would lead to a low-stress level at the joint area.

In practice, with the development of technology, it makes it easy to control the formation of weld geometry. Numerous experimental results showed the effect on fatigue life of load-carrying fillet welds [48], [49] [50]. However, few studies were made until now, concerning non-load carrying cruciform joints [46], [51]. For those welded joints, an experimental test was carried out with weld toe radius, and weld flank angle, varying between 0.5-2.1 mm as well as 95° - 152°, respectively [51].

These test result showed that separately increasing either the flank angle or the weld toe radius would gradually increase the overall fatigue life, as seen in Figure 19. It was also concluded that the weld toe thickness has little influence on the fatigue life of the specimen [51].

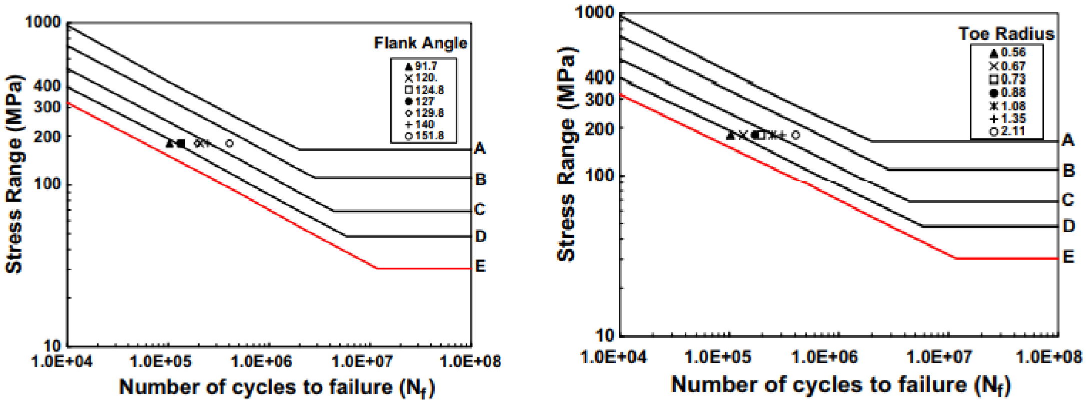

Figure 19. Correlation between weld toe radius, flank angle and fatigue life [51]

In theory, Finite Element modelling can also be carried out to consider any shape variations, as shown in Figure 20 and to investigate their effect on the overall fatigue life of the cruciform joint. This numerical analysis would allow, further variations in weld profiles such as concave-convex shape, horizontal and vertical weld length, throat thickness, radiuses, undercuts, flank angle and so on.

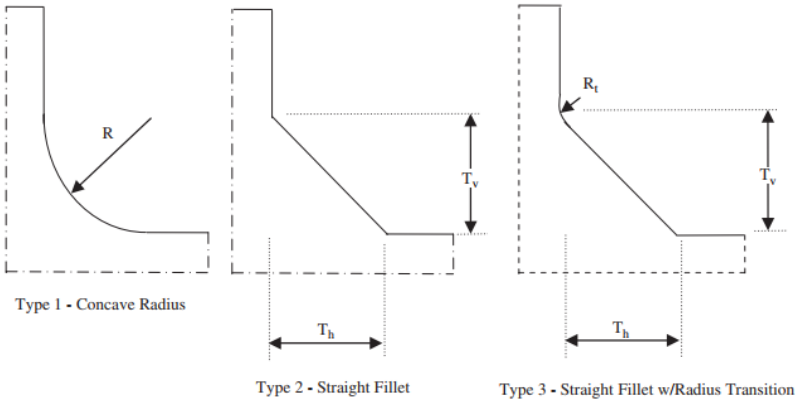

Type 1 - Concave Radius

Type 2 - Straight Fillet

Type 3 - Straight Fillet w/Radius Transition

Figure 20. Different weld shape profiles [46]

To this date, FEM analysis was carried out focusing on mainly the propagation time of the crack, based on the fracture mechanics approach [46], [52], [53], [54], using initial crack in the analysis. This resulted in different stress intensity factors, K_I that is allocated to varying geometries. Further, stress concentration factors, k_t were estimated for weld profiles as in

Figure 20 and can be seen in Table 3. This numerical analysis eventually lead to varying cycles of failure, as the results are seen in Figure 21 regarding the applied nominal stresses.

However, there is still little knowledge about their shape effect on the actual crack initiation and short crack propagation period at the weld toe, which in principle would control the majority time of the fatigue life [45].

Table 3. Weld geometry parameters [46]

Series	Weld geometry type	R (R/t)	T_h=T_v	k_t
A	1 or	0.25	NA	1.46
	3	0.25	9.525	1.52
B	3	0.0625	3.175	2.2
C	3	0.22	6.35	1.77
D	1	0.28	NA	1.45

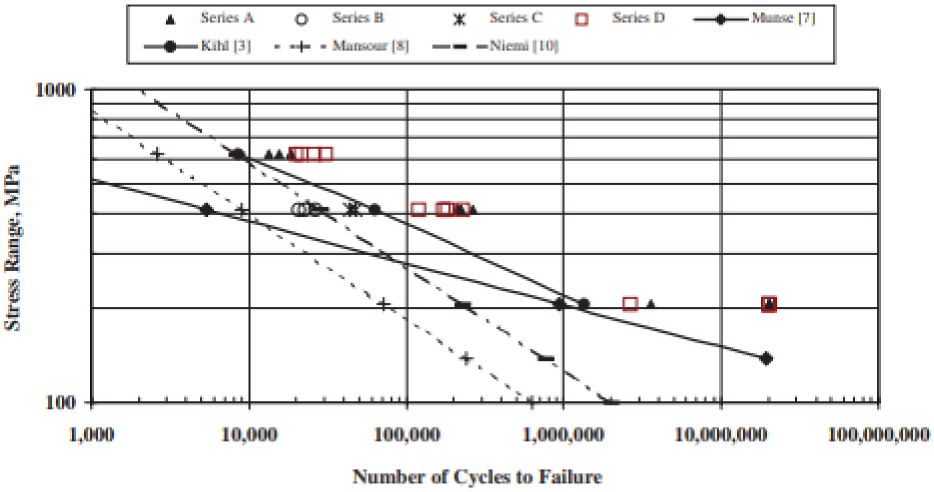

Figure 21. Cycles to failure based on the different weldments [46]

6 LOADING CHARACTERISTICS

Different load cases would have a different impact on the fatigue life assessment of the material. A basic overview of each of the load conditions and their influence on the fatigue life can be seen in *Mechanical Behavior of Materials by Dowling* [17]. During the assessment of LCF, strain-based approach, the following conditions should be considered when doing the analysis.

6.1 Loading History

Fatigue loading in the structure of the hull or other practical applications on board usually involves stress amplitudes that change irregularly on the full scale, i.e. structural components that are subjected to wave loads of variable amplitude and directions. These loads are associated with specific wave characteristics, and a wave scatters [55], [56] regarding the vessel main sailing route. On the global structural scale, the statistical distribution of the wave characteristics is then used for an overall fatigue assessment, which is currently only based on the application of different concepts, mentioned in Section 2.1 [57] to fulfil the requirements of the classification societies [58]

The variable local load history on individual structural components can be illustrated as in Figure 22.

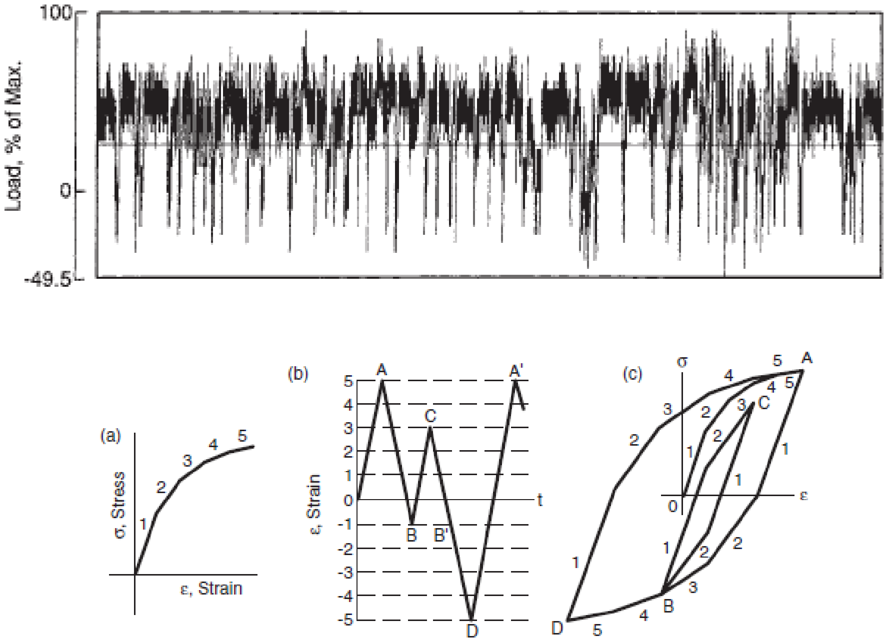

Figure 22. Irregular loads vs time [17]

These stress or strain loading histories then are evaluated by cycle counting such as *rain-flow* counting [17] [7], and the fraction of life is assessed for each cycle and summed up based on *Palmgren-Miner rule* [17] taking into consideration the amplitude variations and the mean level variations of stress or strain.

On the contrary, a simplified load case can be illustrated with a constant amplitude load history, seen in Figure 23. In this case, the amplitudes and mid values for each of the load cases are considered constant values, and its analysis could be done without cycle counting and accumulated damage the assessment of the influence of the variation of mean and peak values in each cycle.

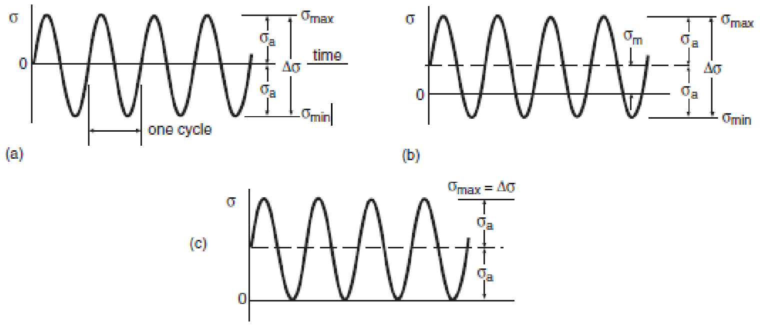

Figure 23. Constant amplitude load case

These various or constant stress amplitudes and peaks in each cycle, can also relate to the strain amplitudes and min-max values, based on the Ramberg-Osgood form [17] and constant material parameters, as seen in equation (8), (9) and in Figure 24 for the elastic as well as plastic part of the curve.

$$\varepsilon_a = \frac{\sigma_a}{E} + \left(\frac{\sigma_a}{K'}\right)^{1/n'} \tag{8}$$

$$\varepsilon = \varepsilon_e + \varepsilon_p \tag{9}$$

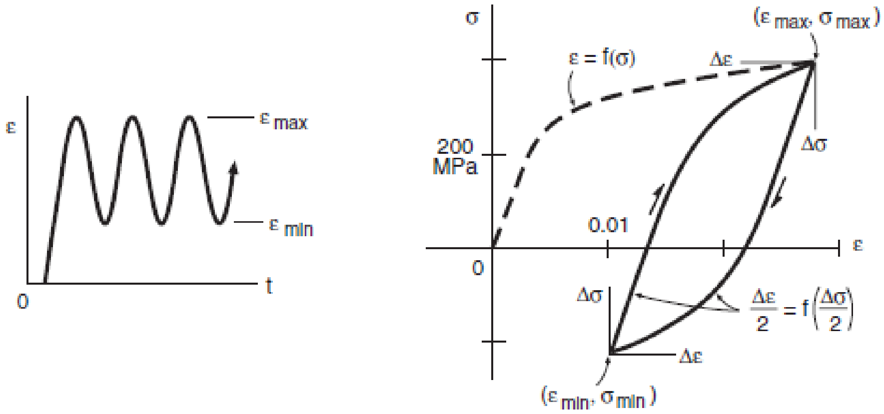

Figure 24. Stress-strain loading characteristic [17]

6.2 Mean Stress effect and Load Ratio

The effect of the mean stress has to be also considered not only in the stress-based approach but the strain-based low cycle fatigue approach as well.

The mean value furthermore is also closely related to the load ratio, $R_\sigma = \frac{\sigma_{min}}{\sigma_{max}}$. In case of a zero mean, when the stress range is alternating between values that are $|\sigma_{max}| = |\sigma_{min}|$ the loading case can be characterized either by giving the amplitude, σ_a, or the maximum stress value σ_{max} as seen in equation (10).

$$\sigma_a = \frac{\Delta\sigma}{2} = \frac{\sigma_{max}}{2}(1-R_\sigma),$$
$$\sigma_m = \frac{\sigma_{max}}{2}(1+R_\sigma) \tag{10}$$

In other cases, if the mean stress is not zero, two independent values are necessary to characterise the loading. These values can be in combination such as σ_a and σ_m, R_σ and σ_{max}, R and $\Delta\sigma$, or σ_{max} and σ_{min}. Two common special cases are R_σ=-1 or σ_m=0 and R_σ =0 or σ_{min}=0, named as completely reversed cycling/alternating and zero-to-tension cycling/pulsating, respectively [59].

Particularly in case of a completely reversed loading, cycling between constant strain limits, the strain-life curve needs to be modified if the mean stress is non-zero. A schematic representation of the changes in mean values of the strain-life curve can be seen in Figure 25.

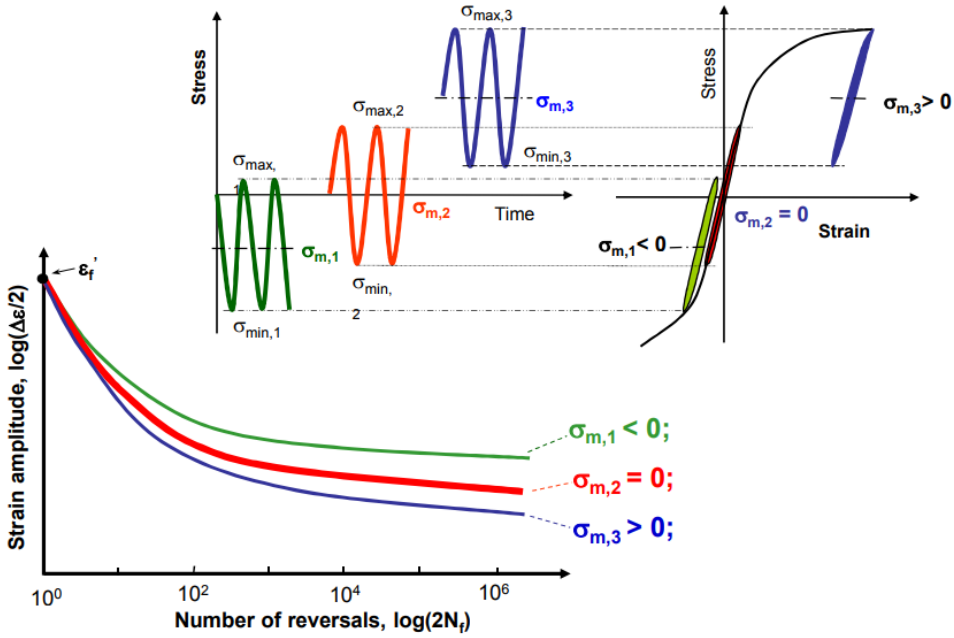

Figure 25. Mean stress effect on strain life curve [17] [19]

Non zero mean values could lead to cycle dependent relaxation [17]. If the component is subjected to a relatively not too large strain amplitude, ε_a, the initially applied mean stress will remain, which will affect the fracture life. However other than the accompanying mean stress, the mean strain itself does not have a significant effect on the fatigue life, unless it is too large that would cover a significant fraction of the tensile ductility [17].

To correct the estimated fatigue life that takes into account not only the amplitude but the mean level, additional equations are needed to calculate the zero-mean stress about the Coffin Manson formula as seen in the fundamental equation of (11).

$$\sigma_{ar} = f(\sigma_a, \sigma_m) = \sigma_a \frac{f(\sigma_a, \sigma_m)}{\sigma_a} = \sigma'_f \left(2N_f\right)^b \tag{11}$$

Different materials would require different equations and methods to consider the mean stress effect, this would also lead to varying accuracy and certain limitations [23]. Most common approaches such as Morrow, Goodman and Gerber, SWT and Walker methods are comprehensively described in the textbook of *Dowling* [17]. The thesis will utilise the SWT solution coupled with the P_{SWT} damage parameter, as seen in equation (12).

$$\sigma_{max}\varepsilon_a = \frac{\left(\sigma'_f\right)^2}{E}(2N_f)^{2b} + \sigma'_f\varepsilon'_f(2N_f)^{b+c} \tag{12}$$

SWT can give a good approximation in the long life regime, however still conservative in the low cycle fatigue region [60]. Furthermore, this approach assumes that no fatigue damage would occur, in case of the maximum stress is compressive, i.e. negative. Nevertheless, it can give acceptable results for a wide range of materials.

The overall observation is increasing the tensile mean stress would result in a decrease of the fatigue strength of the structural component

6.3 Residual stress in welded components

Fabrication and manufacturing operations, i.e. thermal or mechanical processes before welding could result in pre-existing residual stresses within the BM. The evaluation of the possibility of the pre-existing residual stresses comes in the role when the stress determination needs to be done at greater distances from the welded joint. This determination would leave to a function of the superimposition of the weld-induced residual stresses and any pre-existing residual stresses in the parts being joined [61].

However, focusing on a localised area close to the joints, i.e. in HAZ, the stress field will be mainly dominated by the weld-induced higher residual stresses, due to uneven cooling of the material. In case of high tensile residual stress, generated at welds fatigue strength will be reduced [62], by increasing the growth of the fatigue crack, whereas compressive residual stresses [63] would decrease the crack growth rate.

General conclusions and a simple assumption can be drawn based on different fatigue design recommendations [13], [44]. They imply that the magnitude of residual stresses can be equal up to the yield strength of the weld or base material, if the following equation is met, taking into consideration the material parameters [61], in equation (13).

$$\alpha(T_s - T_0) \geq \sigma_y/E \tag{13}$$

Where after cooling the thermal contraction strain gives a higher value than the initial value of the yielding strain. Typically mild LSS material with a lower yield point could reach a higher magnitude of residual stresses in comparison with HSS one. On the other hand, based on the microstructure of the material and the temperature level, phase changes during cooling could also affect the stress state and might result in compressive residual stresses in the HAZ [61], [64]. The residual stress could also vary in different directions relative to the weld, due to restraint of other structural components and geometries. The overall distribution of the residual stress of a butt welded HSS (S690) material can be seen in Figure 26.

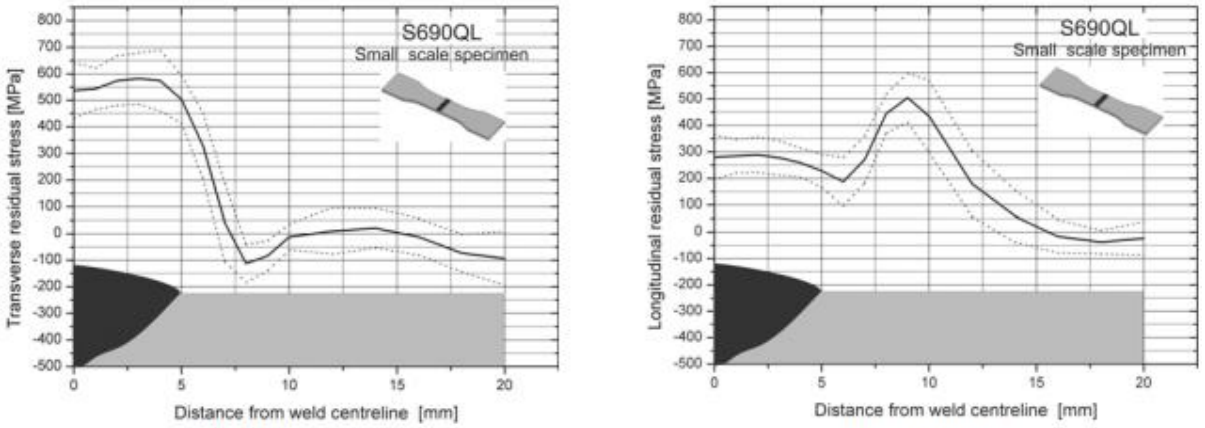

a) Transverse **b) Longitudinal**

Figure 26. Residual stress distribution of butt welded HSS joint [64]

The effect of the residual stress, regardless of the actual magnitude, can be considered during calculation as follows in equation (14) [65], where the effective mean stress σ_m one of the equations from Section 6.2.

$$\sigma_m = \sigma_r + \sigma'_0 \tag{14}$$

Where σ_r the residual stress and σ'_0 the preliminary mean stress, neglecting the presence of the residual stress. Within this consideration, it should be noted that the mean stress itself persist as long as the mean load level remains, however, the residual stress only persist up until a point where the sum of the preliminary residual and current applied stress i.e. load peaks does not exceed the yield strength of the material [66]. This also shows that the residual stresses would further induce a significant mean stress effect, which could lead to an accelerated crack growth rate.

One of the reasons that the crack initiation and propagation time are difficult to predict in the presence of a strong, close to yield level residual stress fields, because of the re-distribution of the residual stress occurring due to plasticity around the crack tip [67], [68], [69].

However recent cases [62] were also examined where, as a result of re-distribution or relaxation happened in the load process, see Section 6.4 for more complex structures as they could result in a lower less harmful stress level. Therefore there are still many uncertainties exist today, and it is necessary to understand the operational conditions, hence the real distribution of residual stresses in welded components for structural optimisation in the hull, since the effect can be either beneficial or detrimental.

6.4 Residual stress relaxation on hull structures

Apart from the initial locked in stresses throughout the hull, i.e. in welded stiffened plates, other stresses may also interact and accompany the life of the vessel that could influence the fatigue damage process. These can be, the weight of the structure, thermal loads, impact loads, fatigue loads due to pressure fluctuation influenced by the waves and roll motions of the ship [70], [62].

Regarding the material mechanical behaviour, multiple studies show that relaxation happens when the equivalent von-Mises stress is higher than the actual yield strength of the material [71], [64], [72].

$$\sigma_{eq} > |\sigma_y| \tag{15}$$

During the operation of a vessel, the highest bending influenced longitudinal compression or tension stress level, depending on the loading conditions, i.e. sagging or hogging can be found on the top as well as bottom plating of the midship section of the hull structure, as seen in Figure 27

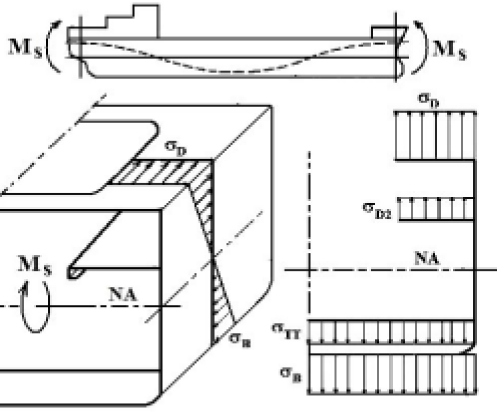

Figure 27. Hull girder stresses over a ship section due to bending [73]

Relaxation would happen under the case of quasistatic tension or compression loading, i.e. longitudinal bending in still water under differed load cases. Experiment [64] shows for butt welded high strength steel S690, which relatively low tension loads may already decrease the residual stress level compared to the values in Figure 26. Whereas for compression loading the weld seam and HAZ less sensitive for relaxation and starts with a delay, as seen in Figure 28 due to overcoming the preliminary tensile residual stresses first.

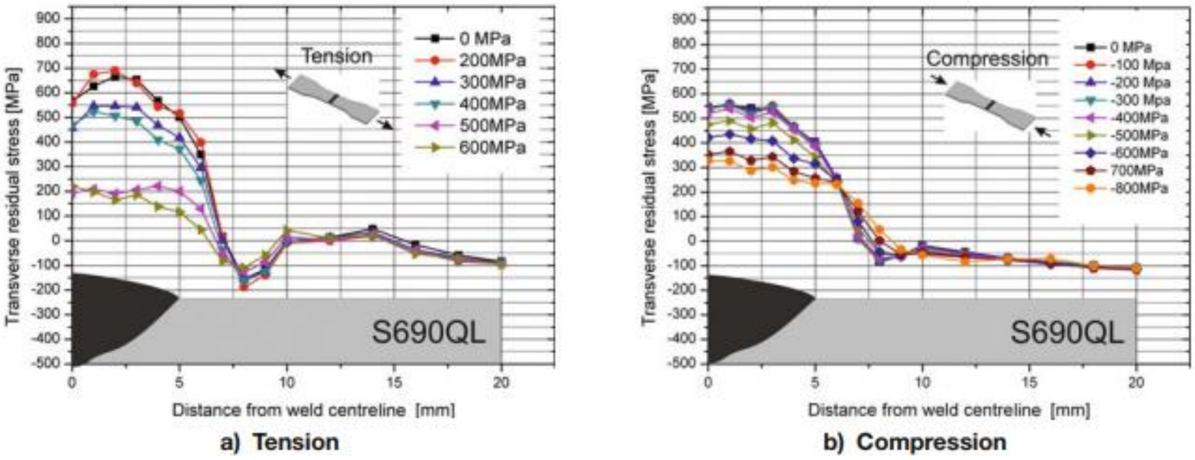

a) Tension **b) Compression**

Figure 28. Residual stress relaxation under increased static tension and compression loads [64]

More realistic loading conditions are the cyclic related loading cases that the vessel encounters, due to varying wave parameters. This would also cause significant relaxation with the redistribution of residual stresses during already the initial first couple of loading cycles. This relaxation can happen according to three different load amplitude regimes such as below endurance limit, above the macroscopic yield strength and between the two [71], [74]. In the low cycle regime, high load amplitudes influencing macroscopic yield are present and experimental data [74] shows, which this could lead to residual stress relaxation toward an initial plate stress value that is the original stress state within the plate due to manufacturing processes, instead of zero, as illustrated in Figure 29.

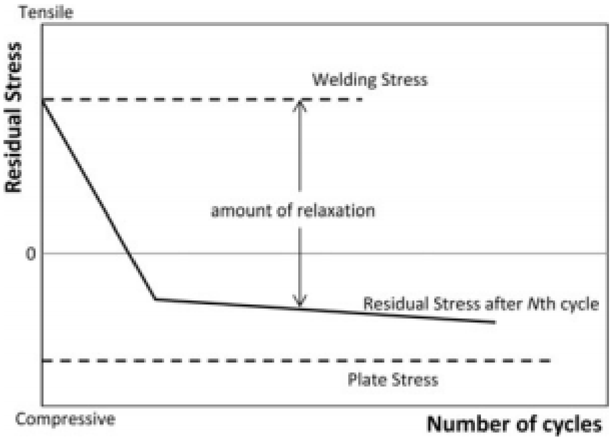

Figure 29. Amount of residual stress relaxation [74]

Cyclic tests on S690 butt welded material under different loading conditions also showed, as seen in Figure 30 and Figure 31, that the larger the load amplitude, the more pronounced the relaxation is compared to the original values in Figure 26.

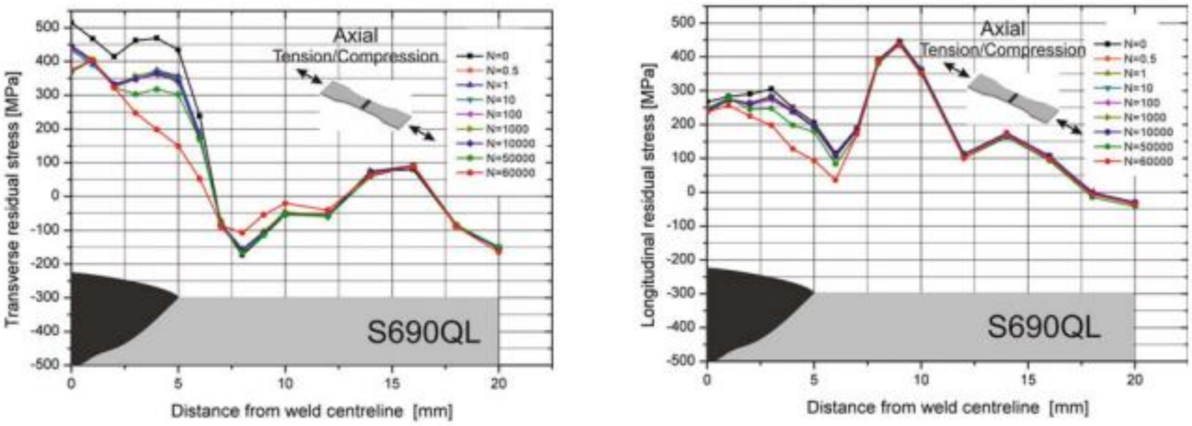

a) Transverse **b) Longitudinal**

Figure 30.Cyclic residual stress relaxation of S690 with $\sigma_a = 300\ MPa$ and R=-1 [64]

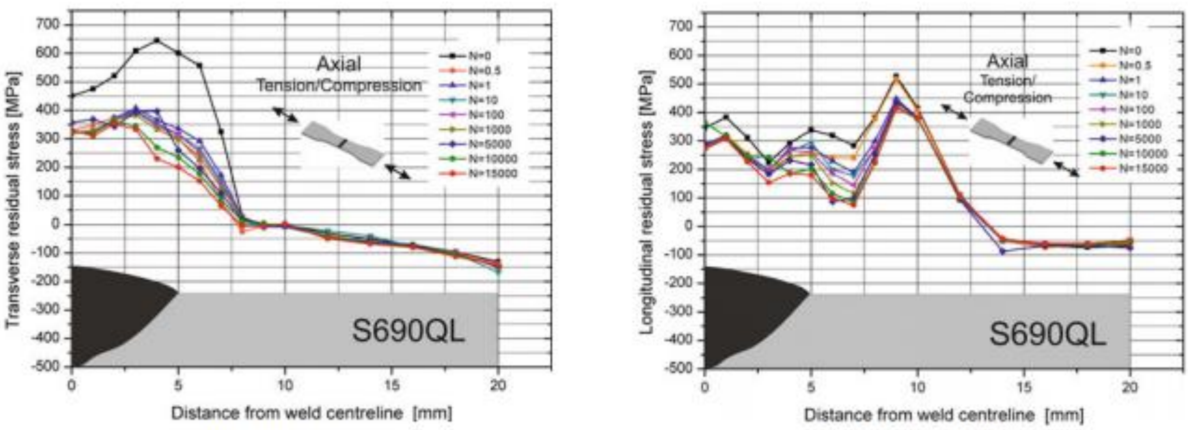

a) Transverse

b) Longitudinal

Figure 31. Cyclic residual stress relaxation of S690 with $\sigma_a = 400\ MPa$ *and R=-1* [64]

Severe loading conditions, under the consideration of impact loads, during slamming or the transversal/horizontal launch of the vessel, could cause extremely high-stress level close to or exceeding the local yield point of the material. This would further lead to plastic deformation and the reduction of the locked in stress level after the welding production.

An illustration of the variations of different loads on the hull girder can be seen in Figure 32 for a specific vessel with the main dimensions and particulars described in [75].

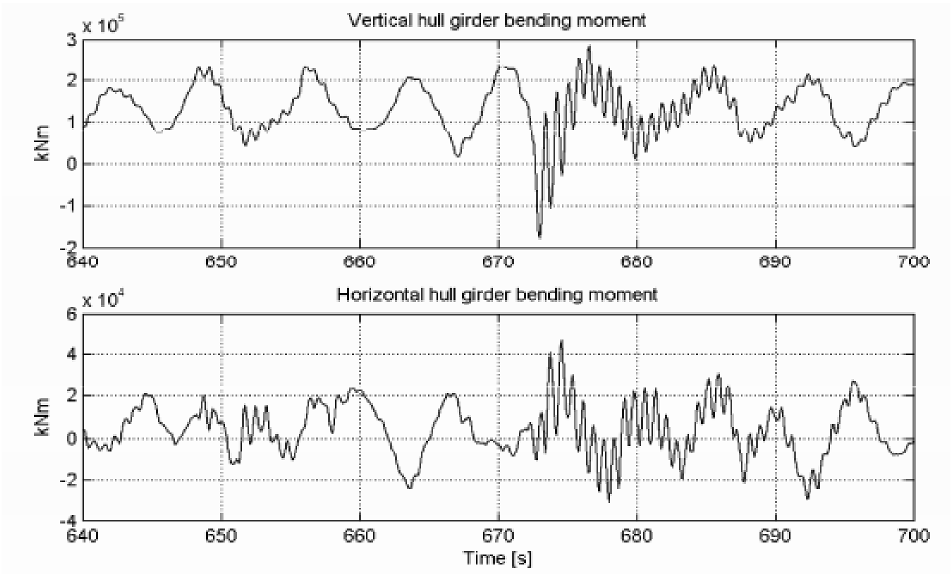

Figure 32. Full-scale wave induced load variation on hull girder [75]

It is yet quite not safe to assume, that during the operation of the vessel relaxation of the residual stresses within the welded structural components will happen at every structural point, without even the application of any post weld treatment [76], [43]. However, in general, the magnitude and the amount of the relaxation would mainly depend on the initial residual stress state, and the maximum applied load. The first one is closely related to the material parameters and the welding procedure, whereas the latter one changed throughout the vertical direction of the hull girder and linked together with a current sea state.

On a local scale higher decrease in residual stresses, even equivalent to the initial plate stress more probable to experience in the bottom or the top structural components, due to the different vertical stress distribution as seen in Figure 27, and the highest stress peaks being experienced on these levels. However on a global scale, when assessing the overall structural integrity of the hull, based on the stiffener placing residual stress values can be significantly high and the relaxation negligible. This further results in strength reduction in the plate and as a consequence a noticeable reduction in the hull girder ultimate strength [77], [71], [78]. A more accurate determination on the overall global scale of the residual stress relaxation is yet to be investigated in the future.

7 MODELLING

After considering the basic principles and the background of the method as in the previous Sections 2-6, they can be applied for the numerical simulation. The analyses were carried out using ABAQUS 6.14 to investigate the different shape effect of the fillet weld as well as to aim to the theoretical optimum parameters that could considerably decrease the crack initiation, thus increase the fatigue life of the specimen.

For the simulation, multiple geometries are considered, and different simplification, as well as input parameters based on the previous Sections, are applied.

7.1 Geometry

Parametric values were given in Matlab to generate 2D geometries in Abaqus for the analysis. The specimen has the main dimensions of plate thickness and width of 10 mm and 50 mm, respectively and as seen in Figure 4. Due to symmetrical boundaries, only one-quarter of the cruciform joint is being modelled.

The size of the HAZ zone was estimated based on macroscopic images of different cruciform joints [46], [79], [80] and set to be some 1 – 1.5 mm in penetration depth. During the numerical analysis for the fully penetrated fillet welds, the leg length is kept constant at 5 mm with a flank angle of 45°. However, two different toe radii were considered; *R* of 1 mm and 0.01 mm.

Furthermore, the variables of the geometric properties can be freely adjusted to consider different cases and their influences within the limitation of the flank angles between 30° and 60°, these values suffice the current state of art welding techniques. At this stage undercuts at weld toe are not implemented.

7.2 Material Properties

Two material properties are being defined and assigned to the generated geometry sections, as seen in Figure 33. The fusion zone consists of only the HAZ properties without a transition zone or any gradual changes of the hardening of the material. To this end, there is a sudden phase change in material parameters between the HAZ as well as the BM geometry sections. With two different mechanical properties, therefore the overall model can be considered as mechanically heterogeneous. The material model in each of the sections, shown in Figure 33 has elastic-plastic, i.e. non-linear behaviour. All the input parameters used are described in Section 4, based on the von Mises criterion as well as the stress-strain curves, shown in Figure 13.

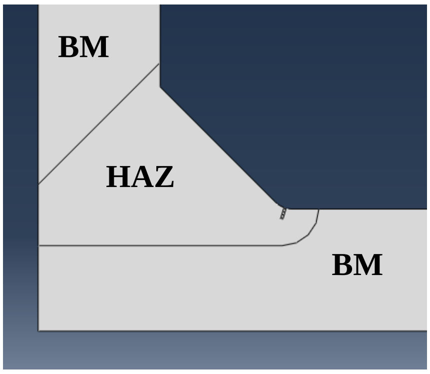

Figure 33. Material property regions

7.3 Load and Boundary Conditions

For simplification, during the simulation, constant amplitude loading is considered. Considering a welded structural specimen in question from either the top or bottom plating of the hull, due to sagging or hogging it would experience the highest stress states. This high-stress state would lead to a considerable amount of cyclic or peak relaxation within the welded structure [70], [71], [74]. To this end, as discussed in Section 6.4 the residual stress effect is considered zero or close to the stress state in the parent material, i.e. welding residual stresses are assumed to be relaxed. The mid stress effect is accounted within a stress ratio, $R_\sigma=0.1$.

The input data for the load characteristics regarding expected fatigue failure is obtained based on the stress ranges used for the fatigue behaviour test of the smooth S690 specimen, as stipulated in [36]. Further, the effect of welding, hence the increased stress state at the toe side, was considered by a stress concentration factor, k_t. This would lead to more adequate and reduced nominal stress that are required for fatigue failure within the low cyclic range, compared to the smooth specimen, as seen in equation (16).

$$k_t S = \sigma \tag{16}$$

Where σ denotes the local stress state at the weld toe and S denotes the nominal stress. In each case, this concentration factor mainly depends on the actual geometrical parameters at the weld toe [17]. However looking at a general optimal case with a toe radius of 1 mm without any applied undercuts, the computed stress concentration factor is close to k_t=4 [81], [82], obviously different cases and geometries would yield varying notch effects and concentration factors as compared in [83], [84]. Furthermore, based on the cross-sectional area of the specimen and the reduced nominal stress, the input load values can be calculated. A summary of the applied load types can be seen in Table 4, whereas Type 3 is optional and could be only applicable for the consideration of HSS material due to the resulting high-stress level, hence high yielding.

Table 4. Load Cases

Load Case	ΔS [MPa]	R	S_{max} [MPa]	S_{min} [MPa]	S_m [MPa]
Type 1	100	0.1	110	10	60
Type 2	150	0.1	167	17	92
Type 3	200	0.1	220	20	120
Type 4	250	0.1	280	28	154
Type 5	300	0.1	330	30	180

The applied load characteristics for Type 3 loading can be seen in Figure 34. It was noted that at the end of the initially applied 10 cycles the hysteresis loops of the material observed at the crack tip, start stabilising after around 5 cycles. To this end for simplification proposes the simulation was reduced to only 5 applied load cycles.

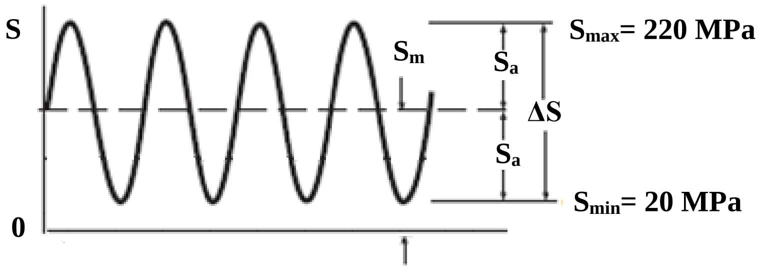

Figure 34. A sample of applied constant amplitude loading with nominal stress range of 200 MPa case

The minimum and maximum load values from Table 4 were applied in each consecutive cycle steps at one end of the model, as seen in Figure 35. Furthermore, due to the symmetry of the cruciform joint, symmetric boundary conditions were applied on one-quarter of the actual geometry along the X and Y axes with zero displacement and rotation. The section is assumed to be in plane deformation (PD).

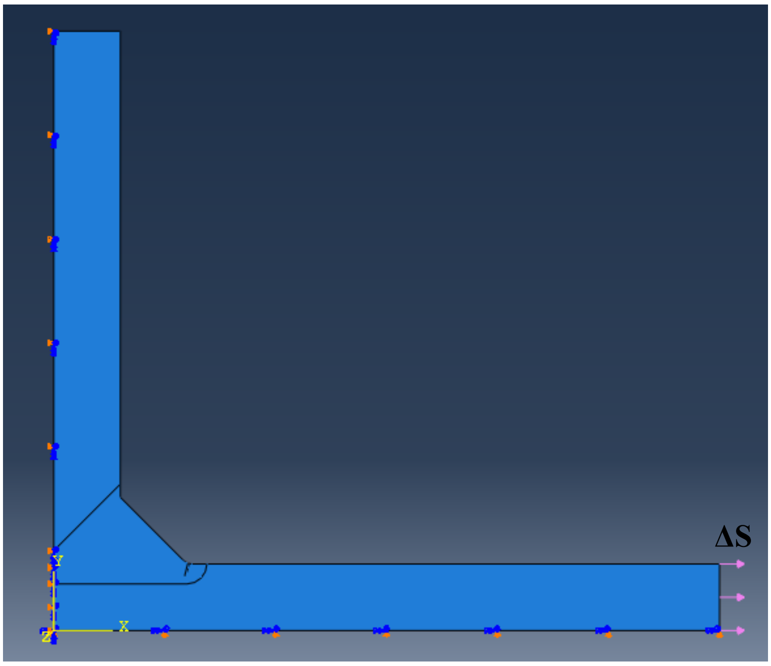

Figure 35. Boundary and Loading conditions of the specimen

7.4 Meshing

The finite 2D element models of the geometry were created using quad-dominated, four-node bilinear plane strain elements (CPE4R) for the overall model.

Two separate meshes were created for the initial geometry as well as the first step of crack propagation, respectively. At both considerations, the aim was to create a smooth transition and gradual change between the element sizes, starting from the area of the toe radius or crack tip in the HAZ to the rest of the model within the BM, as illustrated in Figure 36.

The size of the elements for the initial uncracked model was determined in line with the IIW notch stress analysis guideline where the minimum element sizes are suggested to be ¼ of the toe radius. In the presence of a crack, an additional circular meshing section was created for a finer mesh to account for more accurate stress values, as illustrated in Figure 36. This separate meshing section also covers the highly stressed area. The actual size of this area around the crack tip was estimated to be a radius of 0.01 mm that entails the 80% of the maximum stress [12], [15]. The minimum element size within the crack tip meshing zone was 1/10th of the averaging length of the material, in the order of 1 μm and the maximum element size was 1 mm.

Nevertheless, the mesh sensitivity was also checked for the initial geometry and the one with the presence of the crack. The current mesh sizes seemed to be fine enough to give reasonable results during the FEM simulation and showed to approach a limit value with little change when further decreasing the mesh sizes.

Finally, the overall number of elements for the model was kept in the range 30.000 to 40.000.

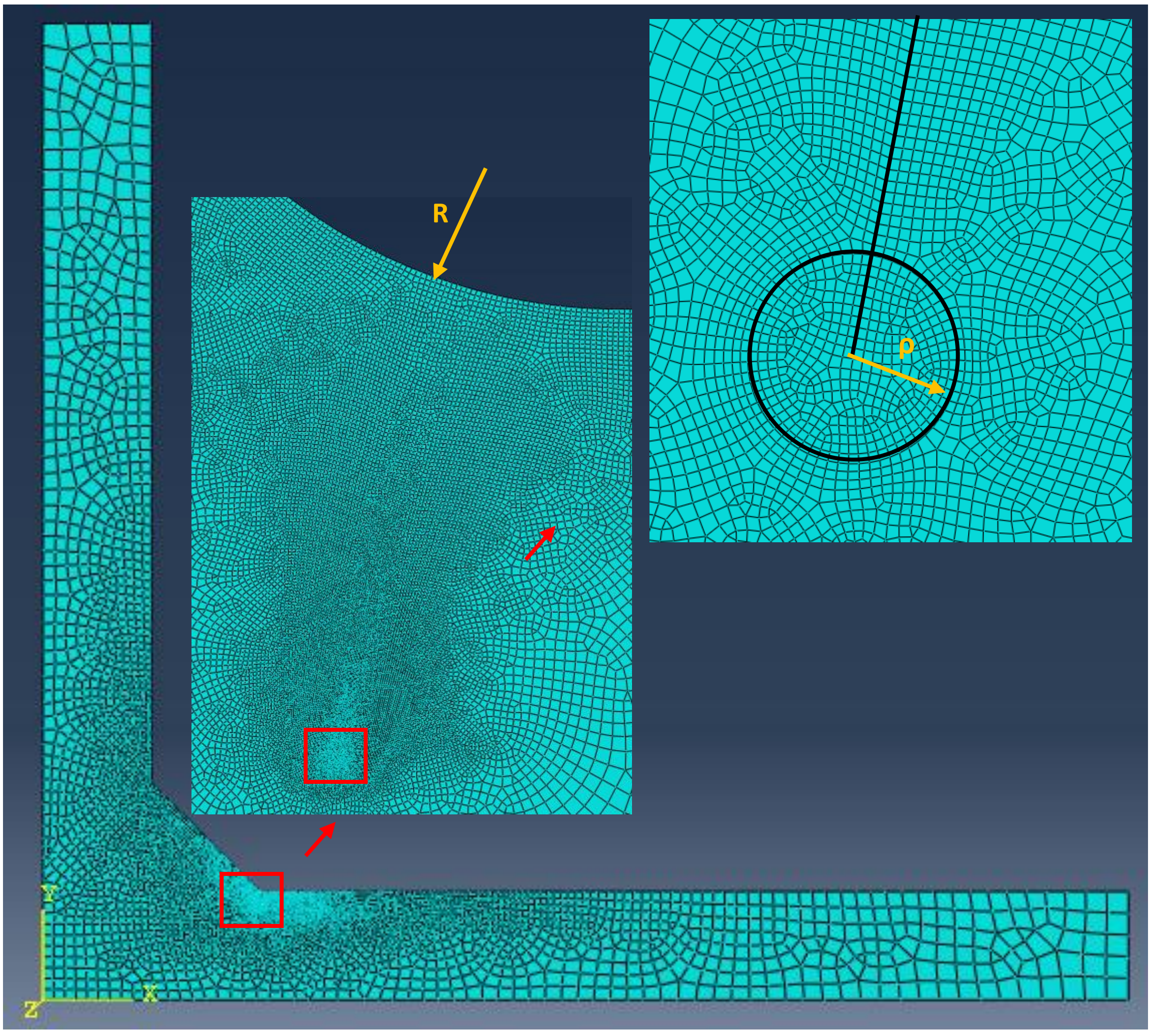

Figure 36. Model meshing for the toe and crack area

7.5 Crack Creation

After creating an analysis in Abaqus and running the model, primarily the following local main variables were output for result discussion and to propagate the discrete crack growths:

- Stress components and invariants
- Plastic strain component
- Equivalent plastic strain
- Logarithmic strain components

These localized parameters were checked, where the crack is assumed to initiate. The starting point coordinates of the crack during the initial intact geometry was determined based on the maximum in-plane principal stress on the toe surface. A sampling line was created for each geometry case, i.e. with the smaller, R=0.01 mm and larger, R=1 mm toe radius along the toe edge. Along with this edge, the allocated element with the highest principal stress value was selected, and the X and Y coordinates of the nodal point of the element were saved.

Multiple sampling paths were created starting from these coordinates, covering a range of 90° in 5° step increments starting from 225° as illustrated in Figure 37. Along each of these paths, the local stress components, such as σ_{eq}, σ_{33}, σ_{22}, σ_{11}, σ_{xx}, σ_{yy}, τ_{xy}, are sampled in uniform spacing with 20 intervals at the top and bottom of the cycles, i.e. max and min loading condition.

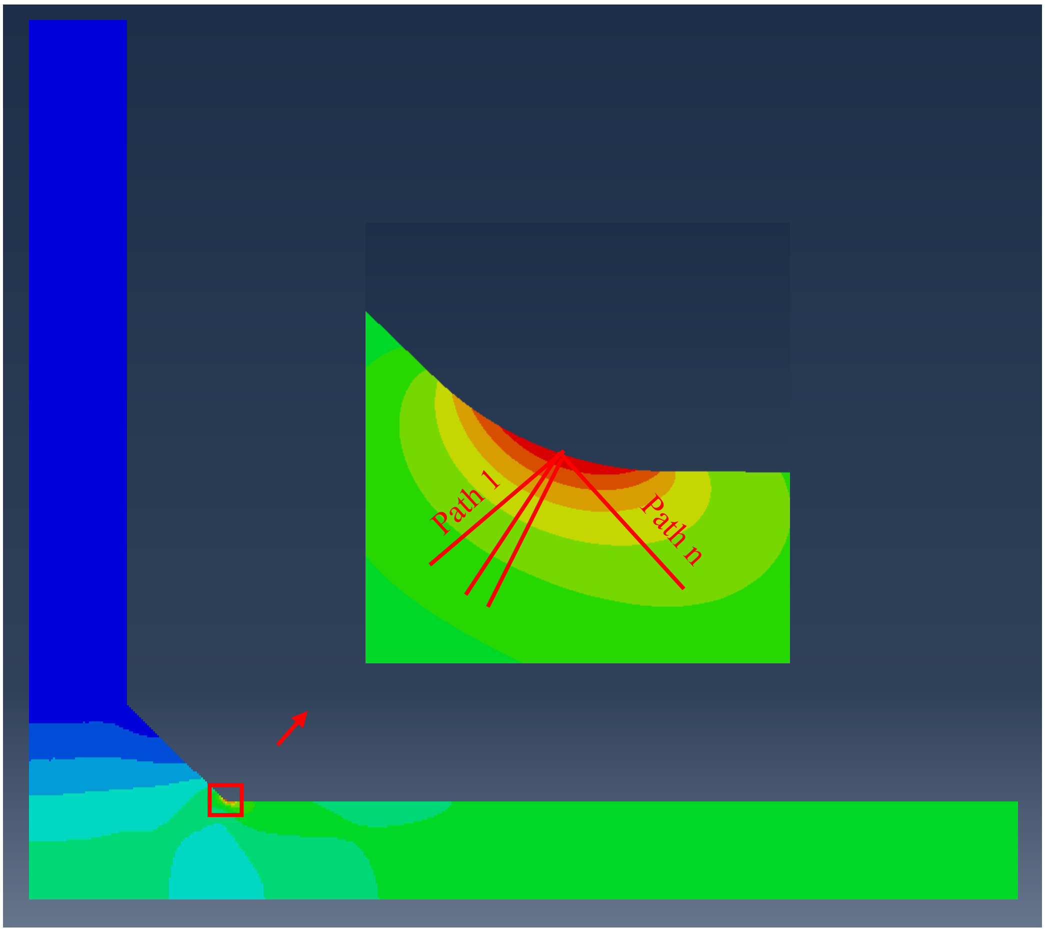

Figure 37. Sampling paths for stress analysis at the weld toe, R= 1 mm, n=1 step

In order to determine the end coordinates of the crack, i.e. crack tip in each of the discrete steps, first, an approximate angle was calculated for the path that is perpendicular to the principal stresses. To this end, this minimum and maximum local stress values were read into Matlab and based on the averaging length of the material an average value was calculated for each of the stress components, as described in equation (6). Furthermore, interpolation was made between two consecutive sampling paths.

Knowing the angle, $\emptyset$ of the crack growth direction and the material characteristic length that also equals, a_0 as stated in Table 1, the X and Y coordinates of the crack tip can be defined as in equation (17).

$$\begin{aligned} crack_{Tip}(X) &= crack_{Start}(X) + a_0 * \cos(\emptyset) \\ crack_{Tip}(Y) &= crack_{Start}(Y) + a_0 * \sin(\emptyset) \end{aligned} \tag{17}$$

After the initial geometry, this procedure is followed during each discrete steps except the necessity to find the coordinates of the highest stressed point. The highest stressed point in case the presence of a crack is at the crack tip. Hence, the coordinates of the crack tip from the previous step equals the coordinates of the starting point for the sampling paths, and crack start at the current step, as seen in Figure 38.

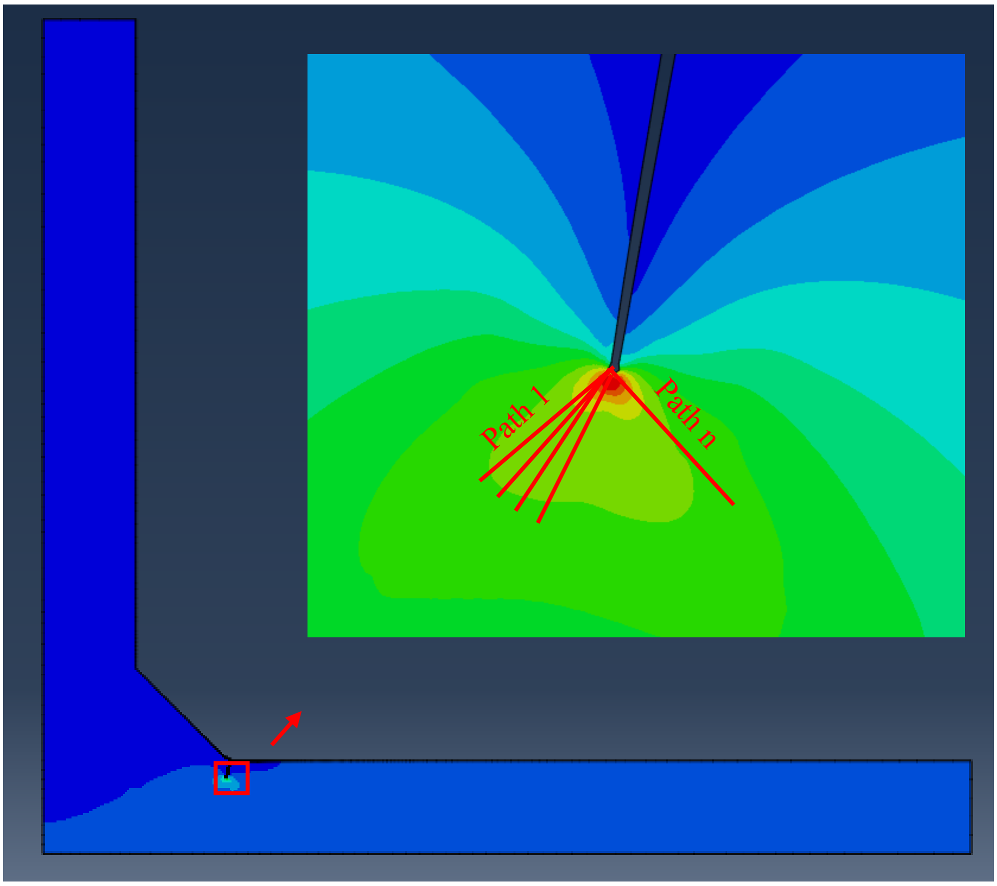

Figure 38. Sampling paths for stress analysis at n=50 steps

Once the coordinates of the start and end points of the crack were determined, the geometry was recreated, and a line was drawn between those points and defined as a standard seam in Abaqus. Hence separate nodes on the elements will be created on each side of the crack line. The meshing was then updated accordingly of the presence of a crack, as described in Section 7.4.

This procedure was repeated in a loop until the crack growth reached 1 mm, as seen in Figure 39.

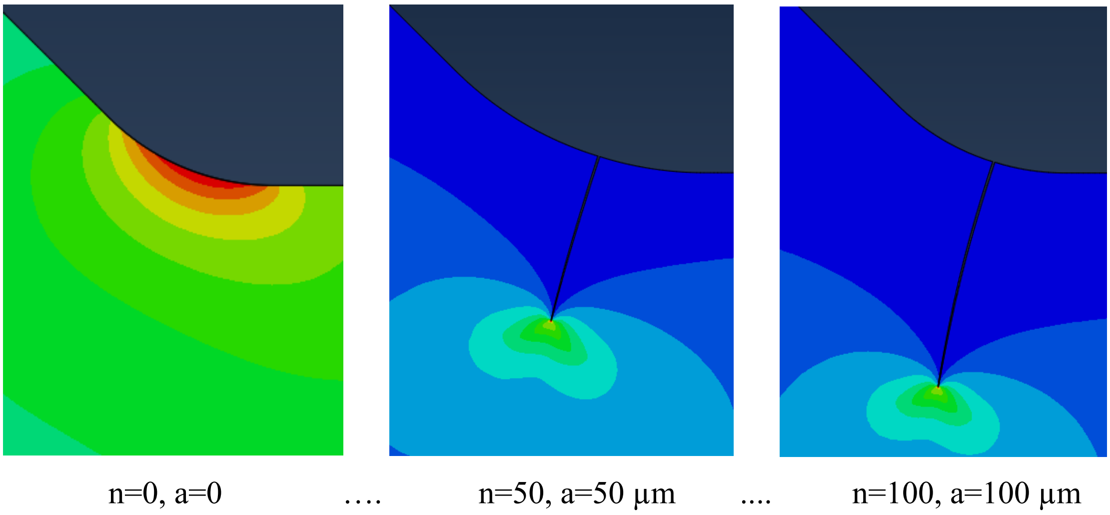

Figure 39. Fatigue crack growth simulation using FE modelling

7.6 Calculation of the cycle number for each step

Also, σ_{xx}, and σ_{yy} values are transformed taking into consideration the allocated angle of the path to avoid at the bottom of the loading out of plane principal stresses as seen in Figure 40. The transformed values are used to calculate the stress range and mid stress.

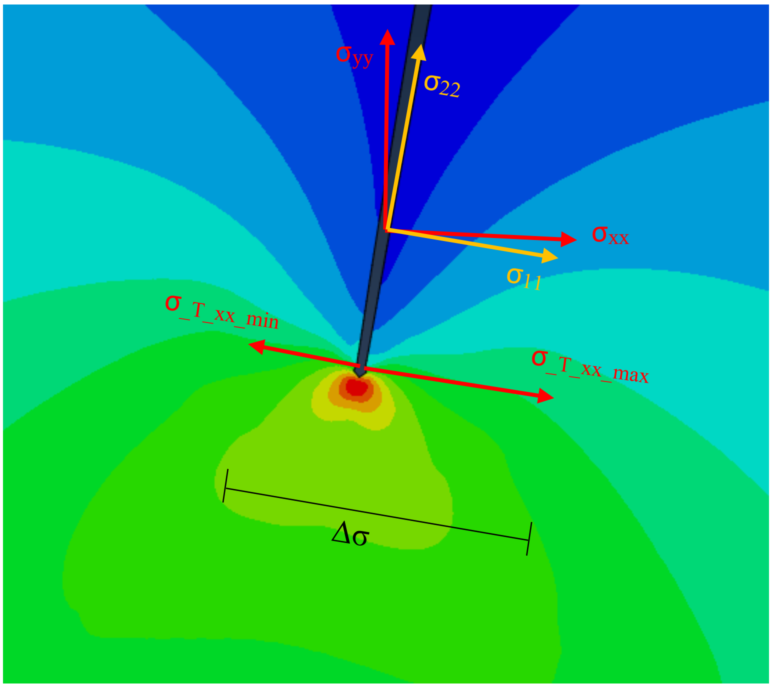

Figure 40. Stress components around the crack

Substituting these calculated stress and strain values, as well as the material parameters from Section 4 into the modified Coffin-Manson formula, i.e. equation (12), the cycle numbers were calculated by performing numerical iterations for each discrete step.

Overall this discrete crack growth FE analysis on the cruciform joints was carried out considering the following cases, as seen in Table 5.

Table 5. Different cases for result analysis

Geometry	**Initial Crack**	**Nominal Stress Range [MPa]**	
		LSS	**HSS**
		100	100
	$a_i = 0$	150	150
R=1 mm	$a_i = 0.1$ mm	200	200
	$a_i = 0.2$ mm	250	250
		300	300
		100	100
	$a_i = 0$	150	150
R=0.01 mm	$a_i = 0.1$ mm	200	200
	$a_i = 0.2$ mm	250	250
		300	300

For the presence of the initial cracks, the results from the cases, *ai=0* were considered, starting from a crack length where it reached 0.1 mm or 0.2 mm. To this end the crack growth path coincides with the original cases, however the overall results such as the fatigue life will be different since the cycle numbers of the individual discrete steps up until the crack length of 0.1 or 0.2 mm are not included, i.e. direction is kept but start at *ai=0.1 or 0.2 mm*.

8 RESULT AND ANALYSES

8.1 Initial Geometry Case

Deformed shapes of the initial models for the different geometry cases and materials without the propagated crack, under tension loading, are presented in Figure 41, Figure 42 as well as in Table 6.

Figure 41. Deformation for LSS Case1 geometry under tension loading with the nominal stress of 300 MPa. Magnification factor is 100.

Figure 42. Deformation for LSS Case2 geometries under tension loading with the nominal stress of 300 MPa. Magnification factor is 100.

The size of the displacements for the two different (LSS and HSS) inhomogeneous material model were reasonable under the applied loading. It can be noted that the deformation of the same materials for both of the geometry cases is similar, and the total displacement of the LSS specimen is roughly 17% higher than the HSS one. Only vertical and horizontal deformations are present without any further angular variation since bending, or secondary bending loading is not applied in the simulation, since the geometry is perfectly symmetric and no angle distortions are present, unlike full scales.

Table 6. Longitudinal relative elongations under tension loading with the nominal stress of 300 MPa

	HSS	**LSS**	**Difference**
Case1	0.064 mm	0.075 mm	17 %
Case2	0.064 mm	0.075 mm	17 %

Figure 43 and Appendix A indicate the maximum von Mises stress levels at the toe for the different geometry cases and materials at the maximum and minimum loading of the cycle, respectively. The overall summary of the increased von Mises tresses due to the changed toe radius that might result yielding under different load cases can be seen in Table 7. The stress states in each case, when yielding happens are highlighted in bold. These values are taken at the end of the load cycles (No.: 5) when cyclic stabilisation seems to occur already. As expected the smaller toe radius acts like a notch and results in higher stresses than the larger radius, whereas the latter one offers a smoother transition. In Case 2 geometry yielding happens in both materials under all applied loading conditions, leading to expected compressive principal stresses and plastic deformation at the toe area. In Case 1 geometry yielding happens in the LSS specimen over 100 MPa applied nominal stress, as seen in Figure 44, whereas HSS specimen is only experiencing deformation within the elastic linear region.

Table 7. Maximum von Mises stresses at the weld toe under different loading conditions

ΔS [MPa]	**von Mises stresses [MPa]**			
	Case 1, R= 1 mm		**Case 2, R= 0.01 mm**	
	HSS	LSS	HSS	LSS
100	234	234	**798**	**436**
150	355	**346**	**807**	**565**
200	468	**359**	**825**	**647**
250	595	**377**	**977**	**708**
300	716	**394**	**1063**	**750**

The 300 MPa nominal stress level corresponds to the loading case where, the loading is higher in the yield stress of the BM of the LSS material model, but still slightly lower than the material properties in HAZ.

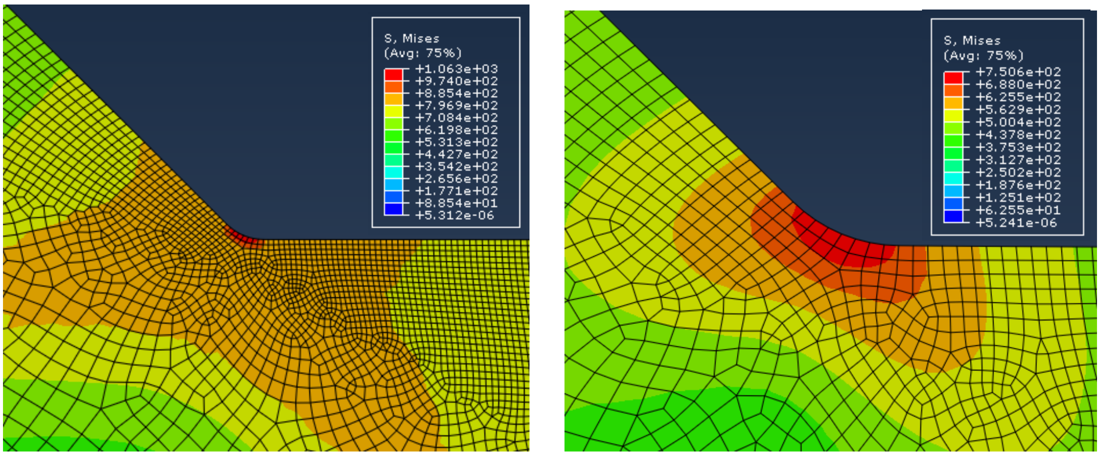

Figure 43. von Mises stress of Case 2, R=0.01mm, HSS (left) and LSS (right) max loading of the cycle, ΔS=300 MPa, cycle No: 5

In cases when yielding happens, plastic conditions will be present, and the plastic strain can be shown. The sizes of the plastic zones are represented in Figure 44 and Appendix A. Under the nominal stress of 300 MPa the Case 1 geometry, with LSS material model, the plastic zone size was 0.6 mm in diameter, whereas in Case 2 for the different material properties the zone was about a diameter of 0.03 mm and 0.08 mm, respectively. In the case of the geometry with a smaller toe radius, higher stress and strain values were observed for the LSS material parameters.

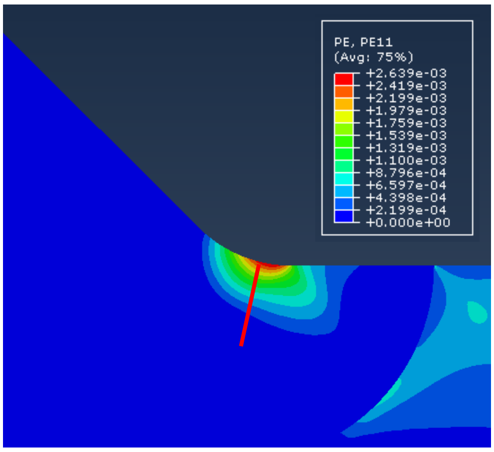

Figure 44. Principal plastic strain (PE11) distribution for Case 1, R=1 mm, LSS under S=300 MPa tension loading

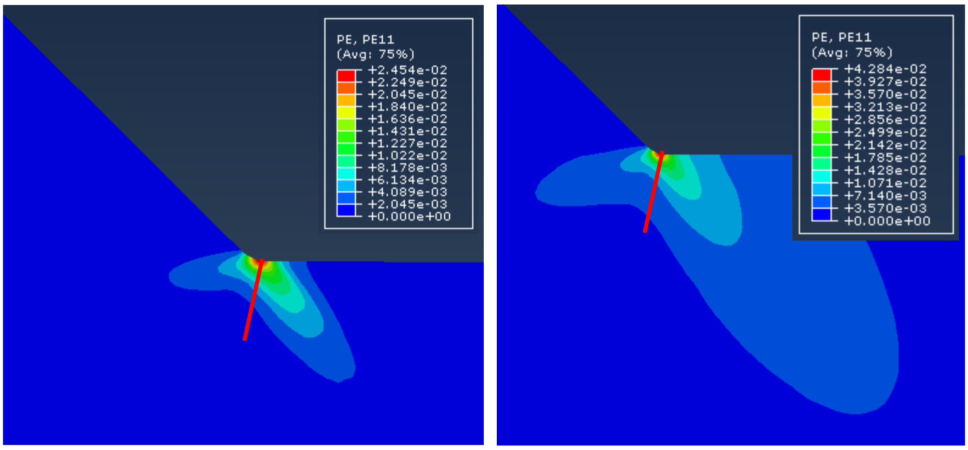

Figure 45. Principal plastic strain (PE11) distribution Case 2, R=0.01 mm, HSS (left) and LSS (right), S=300 MPa

The corresponding normal stress levels and zones can be seen in Figure 46, Figure 47 and in Appendix A. Furthermore, the normal stress and strain distribution versus distance from the uncracked weld toe, along with the Path marked on the individual figures, can be seen in Figure 48, Figure 49 and in Appendix A.

These stress and strain values are presented in logarithmic scale for each of the loading levels that was used for FEM modelling.

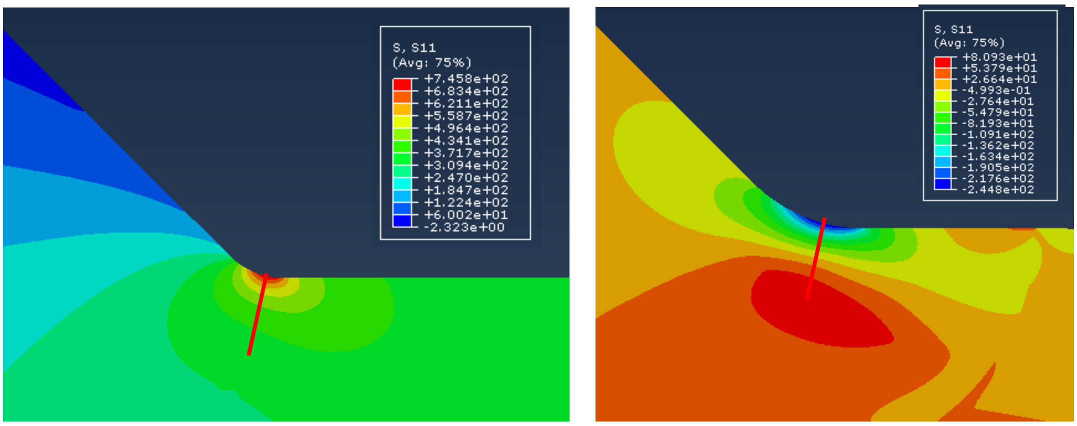

Figure 46. Normal stress distribution of Case 1 LSS at the top (a) and bottom (b) of the cycle no:5, S=300 MPa

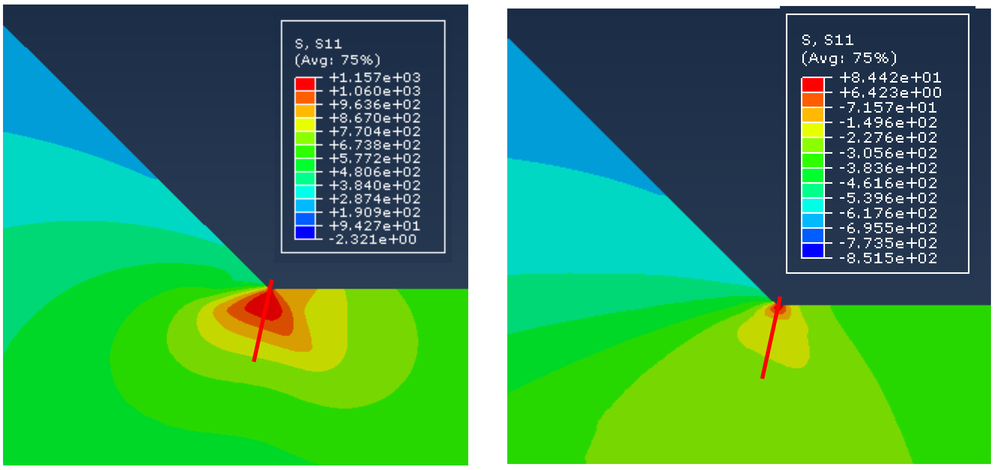

Figure 47. Normal stress distribution of Case 2 HSS (left) and LSS (right) at the top of the cycle no:5, S=300 MPa

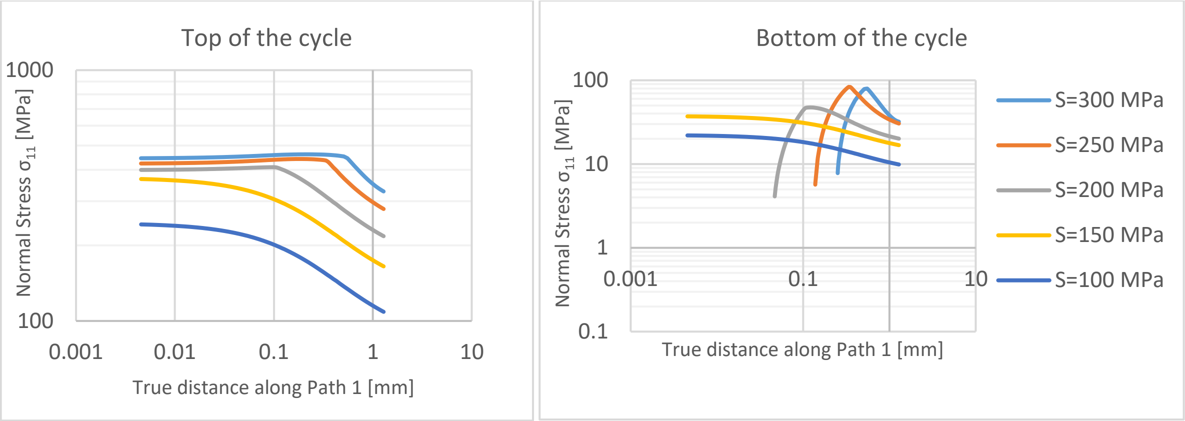

Figure 48. Case 1, LSS, Stress σ_{11} versus distance from the weld toe along Path 1 at the top and bottom of the cycle no:5 for different nominal stress level

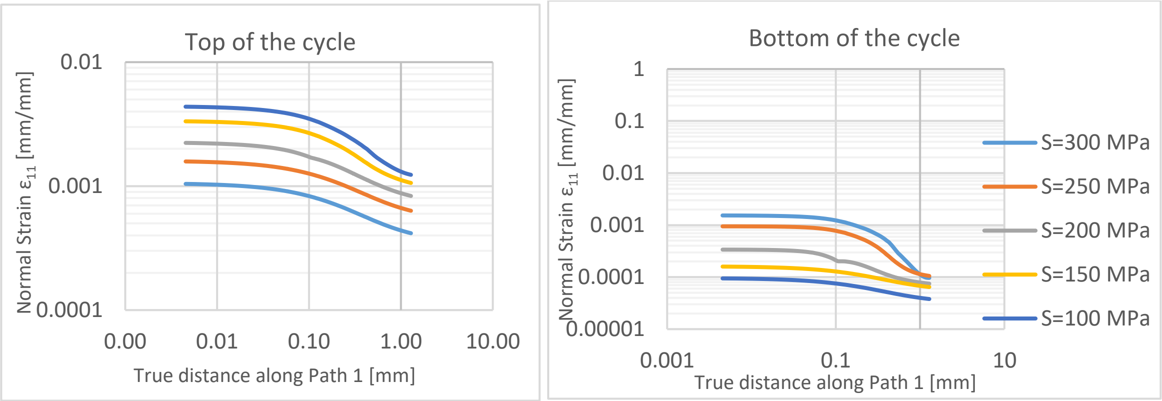

Figure 49. Case 1, LSS, Strain ε_{11} versus distance from the weld toe along Path 1 at the top and bottom of the cycle no:10 for different nominal stress level

In Figure 48 the slope of the stress curves outside of the plastic zone shows independency for each of the nominal stress loadings. At the bottom of the loading cycle, the stress distribution is significantly different when yielding happens, the material experiencing low local normal stress values, which starts increasing rapidly and then decreasing again gradually towards the inner core of the material, i.e. within the HAZ.

In Figure 49 the slopes of the strain curves show strong non-linearity in the plastic zone above the nominal stress of 150 MPa, and unlike the in case of the stress distribution, the strain values are constantly increasing towards the weld toe.

On the contrary, for the HSS material in Case 1 geometry the local stresses are below the yield level. For each load cases, the slopes are not changing and seem to be dependent on the nominal stress load level as seen in Appendix A. Furthermore the strain curves show linearity in the logarithmic scale for each of the loading scenarios.

For Case 2 geometry (with the smaller toe radius), as mentioned for both HSS and LSS materials, the local stresses by far exceeds the yield limit of the HAZ zone for each load cases. Similar behaviour can be experienced for the stress and strain distributions when yielding happens as in Figure 48 and Figure 49, however with significantly higher slopes and nonlinearities in the overall plastic zone for the strain curve as shown in Appendix A.

Since the crack during simulation is only propagated in the HAZ zone without progressing over another material zone, the stress and strain distribution are only inspected in a homogeneous material section. Inhomogeneity occurs when the Path is expended onto the overall geometry, i.e. in the HAZ and BM areas as well. In this case, when crossing the two material sections, a sudden change can be noticed in the distribution curves.

8.2 Crack Propagation

8.2.1 Critical crack length determination

The actual propagated crack length at failure should be estimated, to account for the overall cycle number till failure,

The value of the critical crack length where the final failure of the material occurs can be defined based on the ductile and brittle fracture of the material. In case fully plastic yielding occurs in the cross-sectional area of the material before K_{max} reaches K_c the estimation for ductile failure can be done as in equation (18) [17]. Since the model symmetric, i.e. crack starts propagating parallel at both sides, the consideration of further secondary bending can be avoided.

$$a_c = b\left(1 - \frac{S}{\sigma_y}\right) \tag{18}$$

The results for the estimated final crack sizes based on equation 18, ductile fracture are presented in Table 8.

Table 8. Critical crack length estimation based on ductile fracture

ΔS [MPa]	a_c HSS [mm]	a_c LSS [mm]
100	4.37	3.55
150	4.06	2.83
200	3.74	2.10
250	3.43	1.38
300	3.12	0.66

In case, the fracture toughness, K_c of the material known the critical crack length at brittle failure can be calculated as in equation (19). This fracture toughness, K_{IC} was only roughly estimated based on Table 8.1, 11.2 of *Dowling* [17], and taken as 200 and 150 MPa$\sqrt{m}$ for LSS and HSS respectively. The trend shows that increasing the hardness and the yield strength of the material would result in decreasing the fracture toughness [17].

$$a_c = \frac{1}{\pi}\left(\frac{K_c}{FS_{max}}\right)^2 \tag{19}$$

Where the geometry factor, F was calculated based on Figure 8.12 (b) of the textbook in Dowling [17], as follows in equation (20):

$$F = \left(1 + 0.122cos^4\frac{\pi\alpha}{2}\right)\sqrt{\frac{2}{\pi\alpha}tan\frac{\pi\alpha}{2}}\frac{1}{\pi} \tag{20}$$

For the critical crack length and fatigue life estimate the smaller values should be chosen from the two correspondent fracture case. Furthermore, it seems that in all cases in brittle fracture gave higher critical crack lengths of around 4.5 mm than in ductile fracture.

8.2.2 Stress and strain distribution

The discrete crack steps within the initiation period, resulted in significant rise in the local stress and strain values around the crack tip, within the volume of the damaged zone. Consequently localised yielding happens during each of the discrete steps in both material models regardless of the geometry under all applied loading conditions. In case of the 10th propagated crack step (n=10), under the lowest loading case of 100 MPa nominal stress, the stress and strain distributions and zones for the HSS material model can be seen in Figure 50 - Figure 52 and for LSS in Appendix B, respectively.

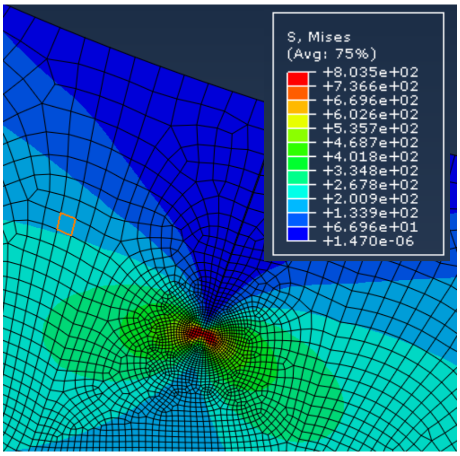

Figure 50. von Mises stress of Case 1, HSS top of the cycle under S=100 MPa nominal load a=0.1 mm, n=10

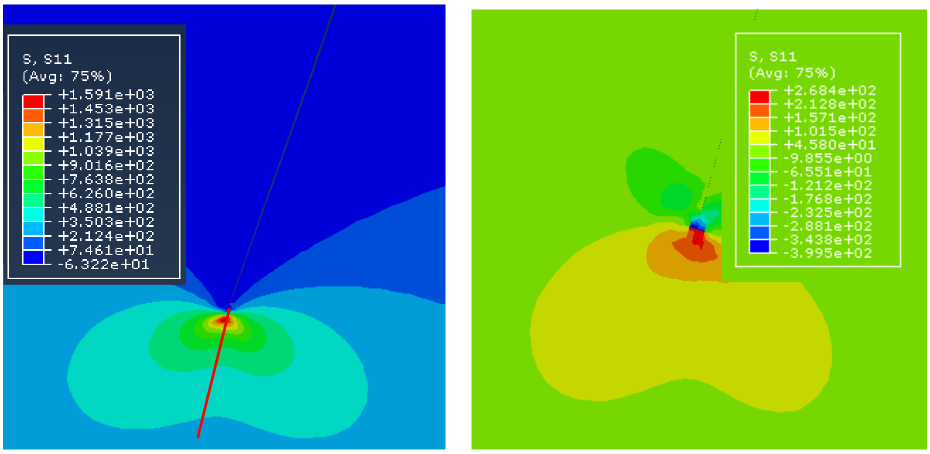

Figure 51. Normal stress distribution of Case1 HSS at the top (left) and bottom (right) of the cycle under S=100 MPa nominal load a=0.1 mm, n=10

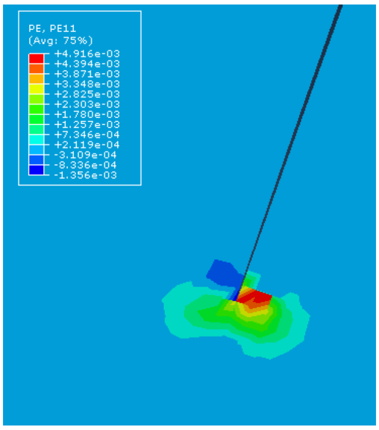

Figure 52. Plastic strain zone of Case HSS 1 at the top of the cycle under S=100 MPa nominal load a=0.1 mm, n=10

The plastic zone is significantly smaller around 0.003 mm for HSS and roughly 3 times larger around 0.009 mm for LSS, at both cases, the zone is more concentrated around the crack tip in contrary to the intact geometry case. The size of this zone, as well as the strain values, are gradually increasing for each of the load cases.

The stress distribution from the crack tip down, showed similarities and significantly close relations for the similar material models, regardless of the initial geometry. This is primarily due to the presence of the crack, hence the influence of the actual size of the toe radius can be waived. For the different nominal load cases, only the magnitudes and the slope of the curve changed. The same behaviour can be noticed as well for the strain distribution for the similar material models.

8.2.3 Crack growth path

The initial geometry and the toe radius as shown in Figure 4, has local stress increasing and decreasing effect and further can also influence the crack propagation paths and its angles for each of the steps, due to the differences in the stress flow as seen in Figure 53. The stress flow is steeper in Case 2, R=0.01 mm with the smaller toe radius whereas the Case 1, R= 1 mm offers a more gradual transition between the vertical and horizontal structures.

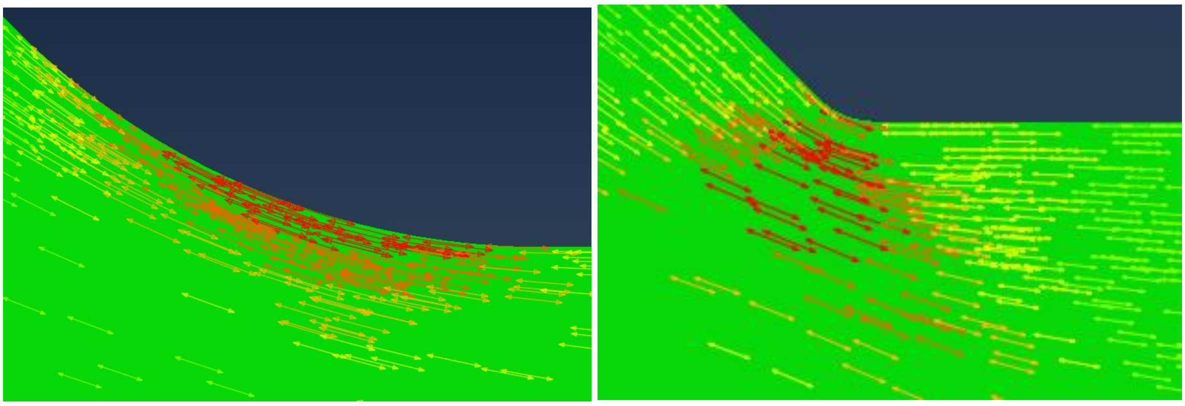

Figure 53. Initial stress flow of the intact geometry for Case1 HSS (left) and Case 2 HSS (right) under the nominal stress level S=250 MPa

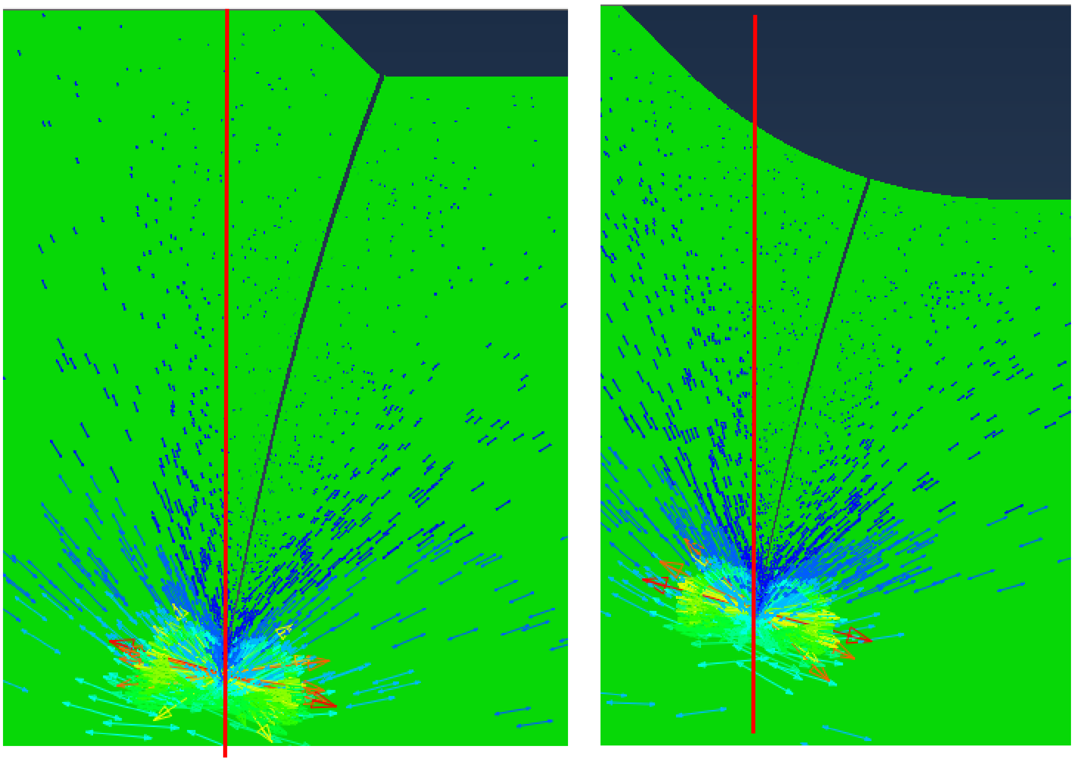

Figure 54. The vertical direction of the crack propagation for Case 2 HSS (left) and Case 1 HSS (right) under the nominal stress of S=250 MPa, a=1mm

The direction of the crack growth during the initiation period profoundly differs from the vertical y-axis based on the actual weld geometry. Later on, it tends to move forward to be perpendicular to the applied load, i.e. parallel with the y-axis during the long crack propagation period, as seen in Figure 54. These crack path changes can be realised in each step as a function of the crack length as shown in Figure 55.

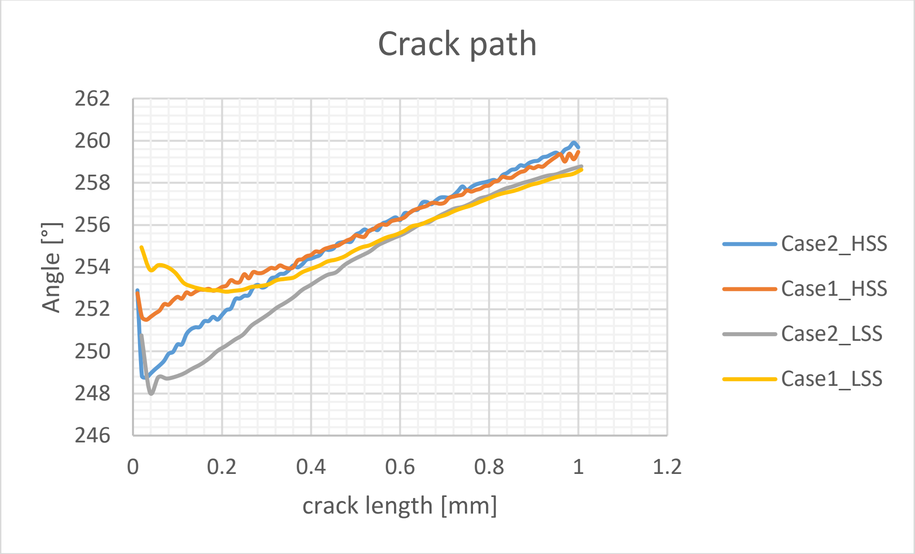

Figure 55. Crack path angles for each discrete steps for different materials and geometries under S=250 MPa,

A sudden drop, i.e. 1-2 degrees and change can be noticed in the other direction after the first step, however afterwards it linearly increases with the same slope for each of the material and geometry models under the same applied load.

8.2.4 Damage Parameter P_{SWT} and Triaxiality

Based on the modified Coffin – Manson formula that also takes into account the mean stress level, as in equation (12) the damage parameter, P_{SWT} [17], [21] can be calculated for each discrete steps, as follows in the equation (21)

$$P_{SWT} = \sqrt{\frac{\Delta\varepsilon}{2}\sigma_{max}} \tag{21}$$

The change of the damage parameter as a function of the effective crack length (a_0 + a) considering each discrete steps is shown in Figure 56, and Appendix C.

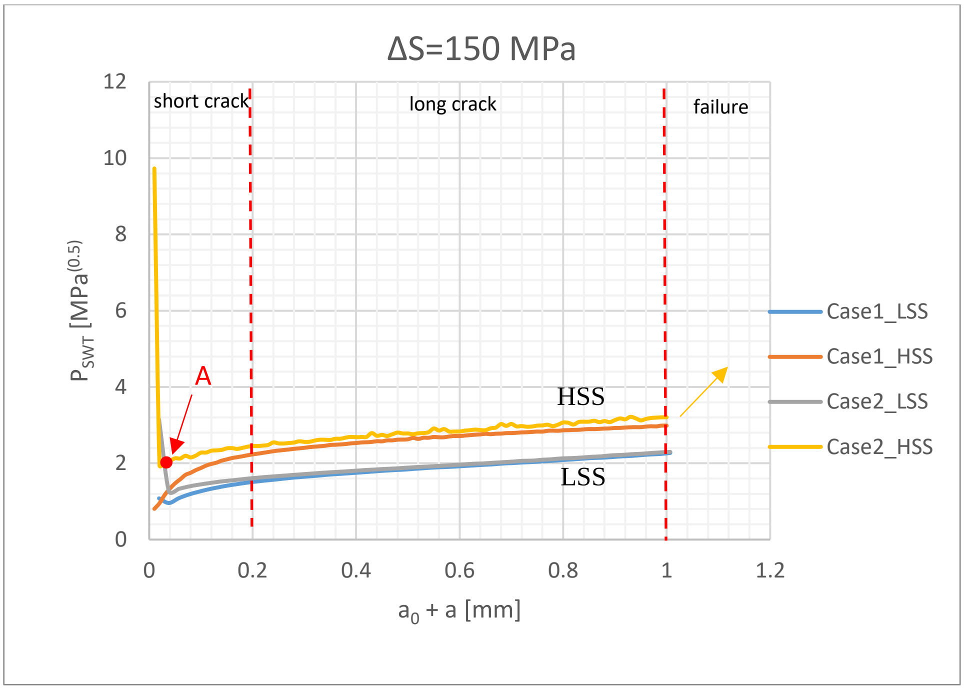

Figure 56. Damage parameters for different material and geometry models under the loading of S=150 MPa

It can be seen that the values coincide for the same material properties and at the beginning similar since plasticity is small, but HSS seemed to have 30-50% higher values. The difference between the results of the LSS and HSS is due to the macroscopic properties of the material, i.e. the actual grain size distribution since it gives the averaging length of the P_{SWT} calculation. The grain sizes of the LSS material are considerably bigger than the HSS. Hence the averaging length is around two times larger. In addition, σ_{max} and $\Delta\varepsilon$ are different as seen in Appendix A.

For the geometry Case 2 with the smaller toe radius, regardless of the material model for most of the applied nominal loads, the values as a function of the crack length first are experiencing a sudden drop before the linear increase. However the magnitude of this linear part and the slope of the curve seem to be independent for each of the loading cases, as seen in Figure 56 and Appendix C. However for Case 2 HSS the values, especially for the first step and above 150 MPa nominal stress load are unrealistically too high. For the Case 1 HSS model the averaging length is smaller than the toe radius, but about the same size in the case of the geometry model Case 2. However, in general, the influence of the high stressed local area at the toe on the surface could lead to higher P_{SWT} values, with smaller or same averaging length than the size of radius itself.

The stress triaxiality under the same nominal loading (S=150 MPa) can be seen in Figure 57 and for the other load levels in Appendix D, respectively. For the weld toe on the surface, the triaxiality that is based on the Hydrostatic and von Mises stresses as follows in equation (22).

$$TH = \frac{\sigma_{Hydrostatic}}{\sigma_{von\ Mises}} \quad (22)$$

TH is roughly 0.5 for each loading cases, while during the short crack propagation this value starts to increase significantly. The magnitude of the increase and the behaviour of the curve seems not to be consistent for each of the nominal load cases. However, the same material model resulted in the same behaviour and values of stress triaxiality regardless of the initial geometry of the model. Above the nominal load level of 200 MPa, the increased stress triaxiality of the HSS material seems to be higher than the LSS at the crack length of 1 mm.

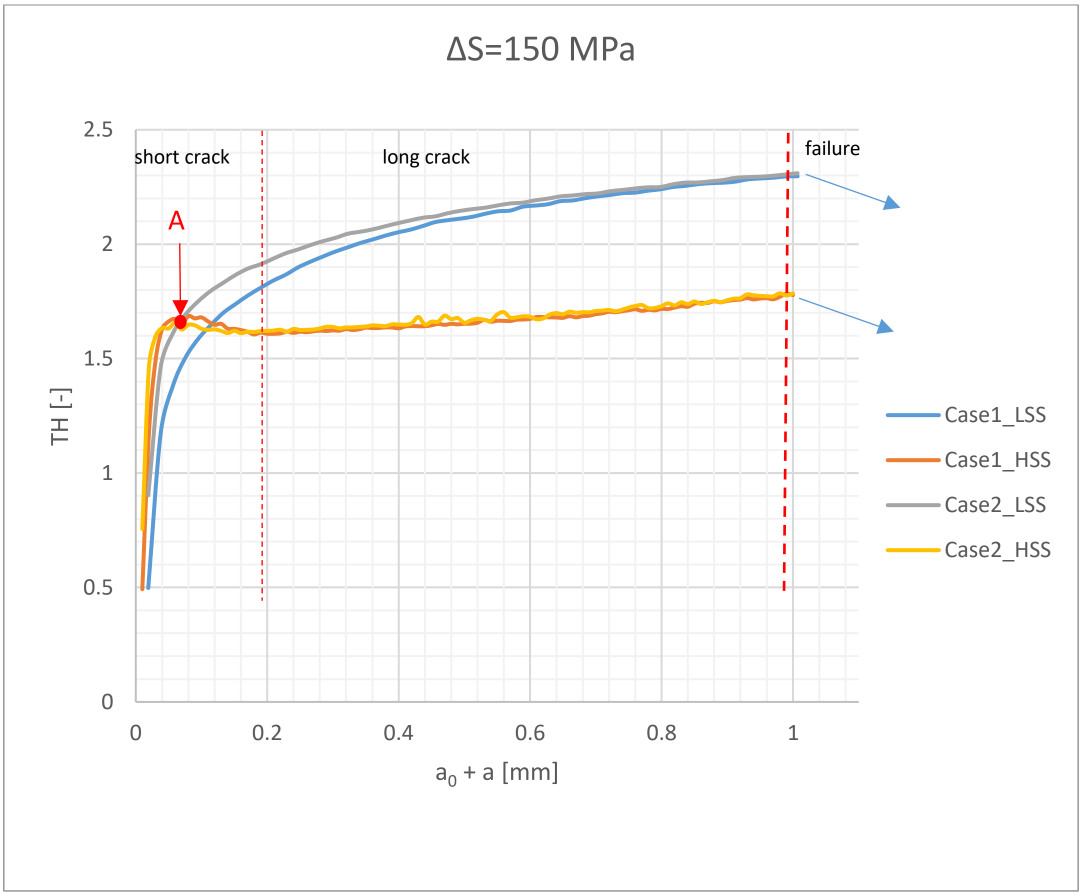

Figure 57. Stress triaxiality for different material and geometry models under the loading of S=150 MPa

8.2.5 Crack growth rate

The crack growth rate, CGR is calculated following the equation (5) and the results are plotted for the different geometries and material models against the effective crack length, as well as the stress intensity factor range ΔK (a_0 + a). The latter was calculated based on the varying geometry factor, *F* as in equation (20) and the effective crack length for each discrete step, as summarized in Appendix E. In Figure 58, when the CGR is shown as a function of the effective crack length the difference in the CGR between each nominal loads is visible and varies greatly based on the material model and the toe radius. When the CGR is plotted against the ΔK (a_0 + a) value, this difference vanishes between each of the curves and can be fitted with one curve in load cases where initial yielding does not happen such as Case 1 HSS under the different load levels. Only the starting point varies for each load levels, these points compared to the K_{th} threshold stress intensity factor $(63\ MPa\sqrt{mm})$ and CGR curve plot during the long crack propagation period estimated based on the Paris – Law with values from Table 3.15 of the IIW recommendation [13], are also shown in Figure 58.

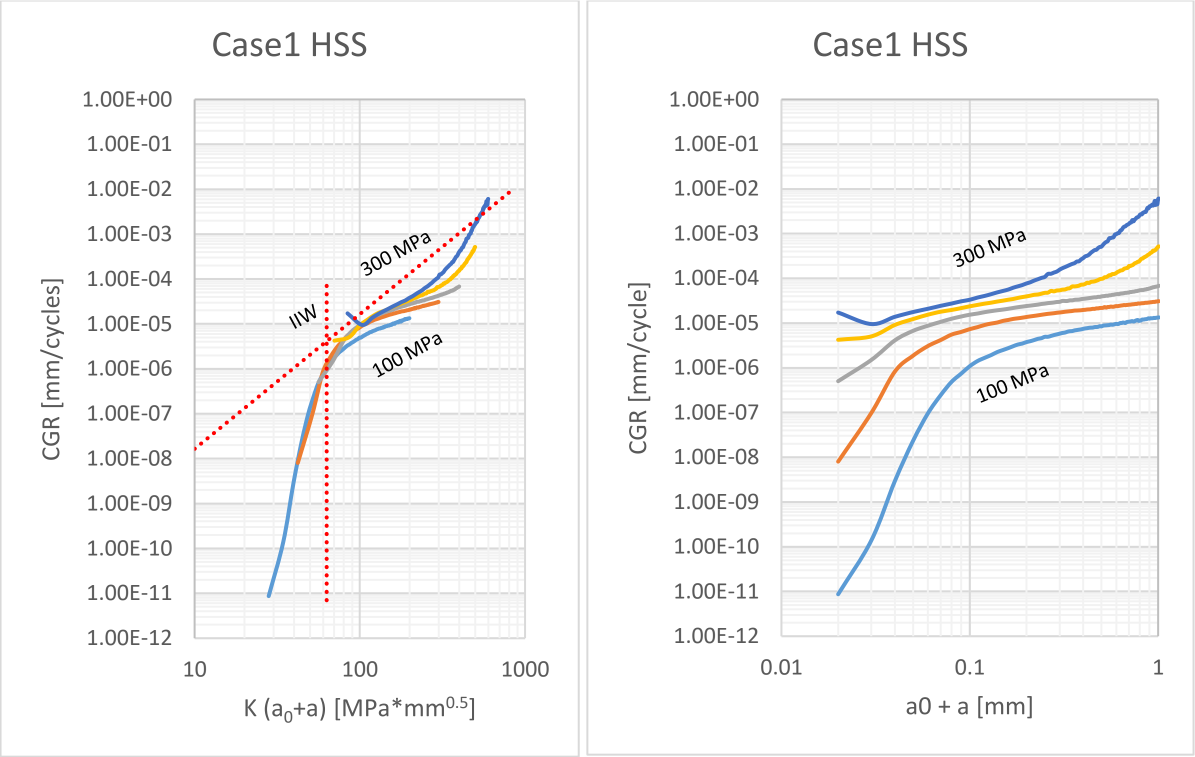

Figure 58. CGR plotted as a function of stress intensity factor (left) and effective crack length (right)

When initial yielding happens at the weld toe, the CGR curves are varying significantly for each load level not only at the linear elastic part but also at the beginning of the curve that represents the initiation of the crack a significant sudden drop can be experienced. This phenomenon can be seen in Appendix E and Figure 59. This sudden change and short crack growth period are more significant and steeper for the HSS material compared to the LSS. This shows a high dependency on the microstructural of the material mainly for the initiation period.

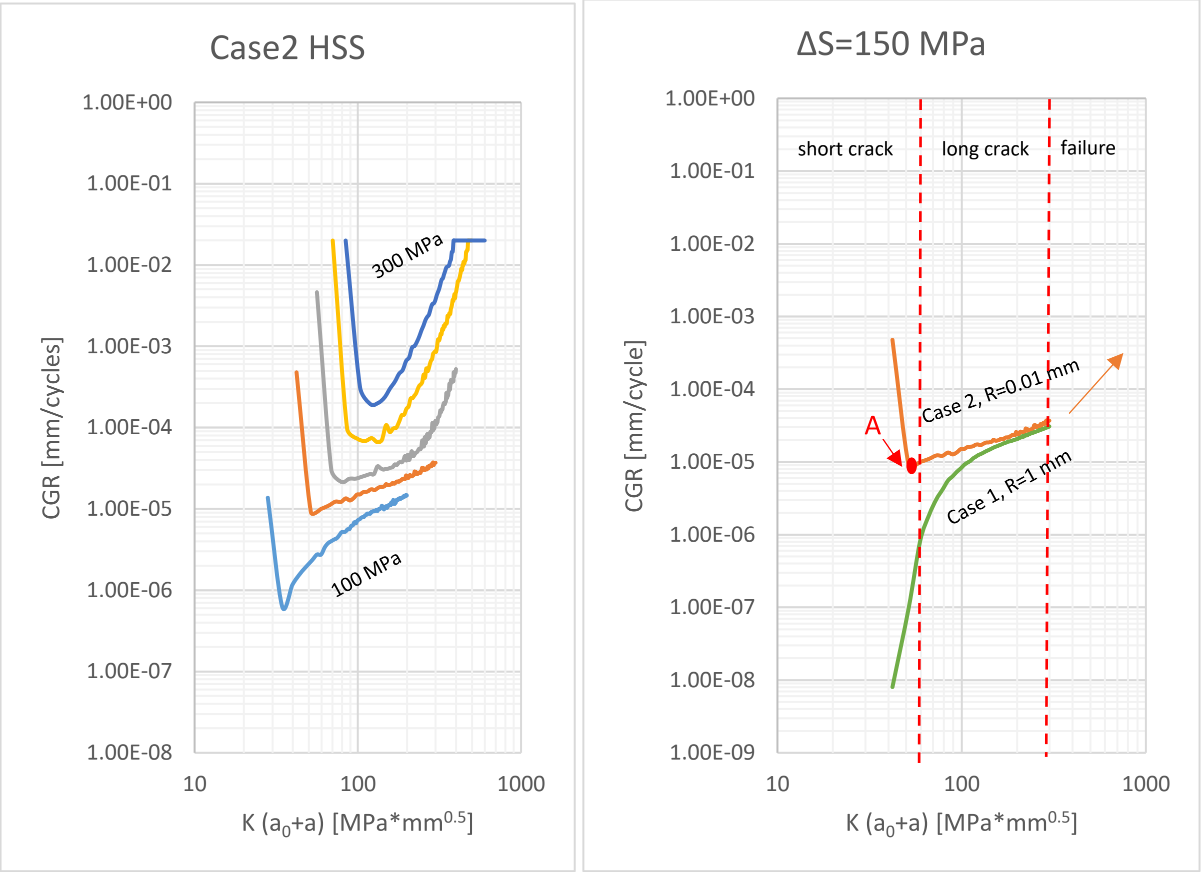

Figure 59. The sudden drop in CGR due to initial yielding at the toe area (left) and the influence of geometry on CGR (right) for HSS material

Clear differences can also be seen in the CGR in each of the crack propagation periods that can be divided into the short crack, long crack as well as a tearing-related final failure that results in very quick crack propagation as illustrated in Figure 58, Figure 59 and in Appendix E, respectively. The intermediate and the latter period shows an increasing trend in the slops as well as coinciding for both HSS and LSS materials, respectively for higher load levels. During the short crack initiation and propagation period, the plastic zone size is significantly high at the weld toe in the geometry case of R=0.01 mm. This plastic zone size decreases and during the presence of the crack start increasing again exponentially. This size at the crack tip is smaller than the averaging length and the damaged zone of the material.

After the drop during the initiation period, the CGR non-linearly starts increasing until point A, seen in Figure 59 for the curve under the load case of S=150 MPa, when the plastic zone size reaches the size of the damage zone and the linear long crack growth period starts with a constant slope. These changes can also be seen in the allocated stress triaxiality graph in Figure 57 that consequently effecting also the P_{SWT} values in Figure 56 for each of the damage process period defined based on the CGR curve. During the long crack, intermediate period the triaxiality increases almost linearly as seen in Figure 57. When extensive plasticity occurs the size of the yield zone becomes considerably large [85] resulting the crack tip to become larger with a larger radius as seen in Figure 60, that also reduces the local stress level at the crack tip, this reduction can also be noticed as a decrease in the triaxiality curves. Thus during this final failure period, a high increase can be noticed in the CGR curves as well.

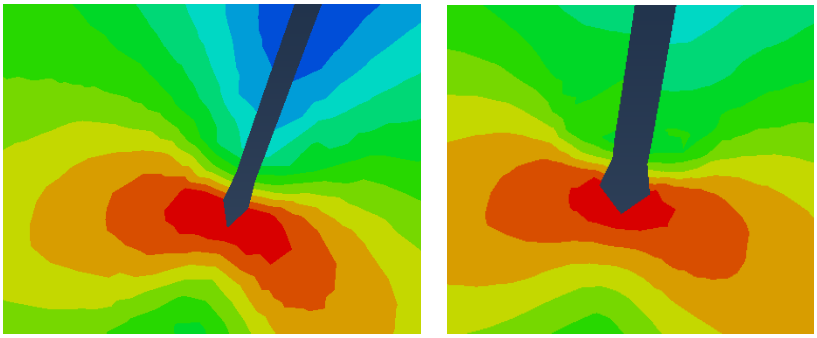

Figure 60. Crack tips a=0.1, n=10 (left) and a=1 mm, n=100 (right) of Case 2 HSS under 300 MPa nominal loading

Nevertheless, for comparison purposes, the inverse of the CGR, i.e. dN/da was plotted as the function of the crack length to calculate the areas under the curves to account for the overall cycle number, as seen in Figure 61. For interpolation, Simpson's rule was applied under also different *da* sample frequencies to check the sensitivity of the calculation as well that resulted in no major difference or sensitivity by changing the sample lengths, *da* for the point on the curve. The plotted FEM graph as well as the plot made based on the IIW recommendation [13], taking into consideration an M_k stress intensity factor suggested by IIW [13] due to the presence of the weld. The areas under the curves differ. However, it can be noticed that the curve tend to coincide after around a crack length of 0.2 mm, i.e. during the start of the long crack propagation period as seen in Figure 61. This is well in line with the theory since the IIW recommendation only takes into account the long crack propagation. Hence it results in considerably lower cycle numbers and different type of curve.

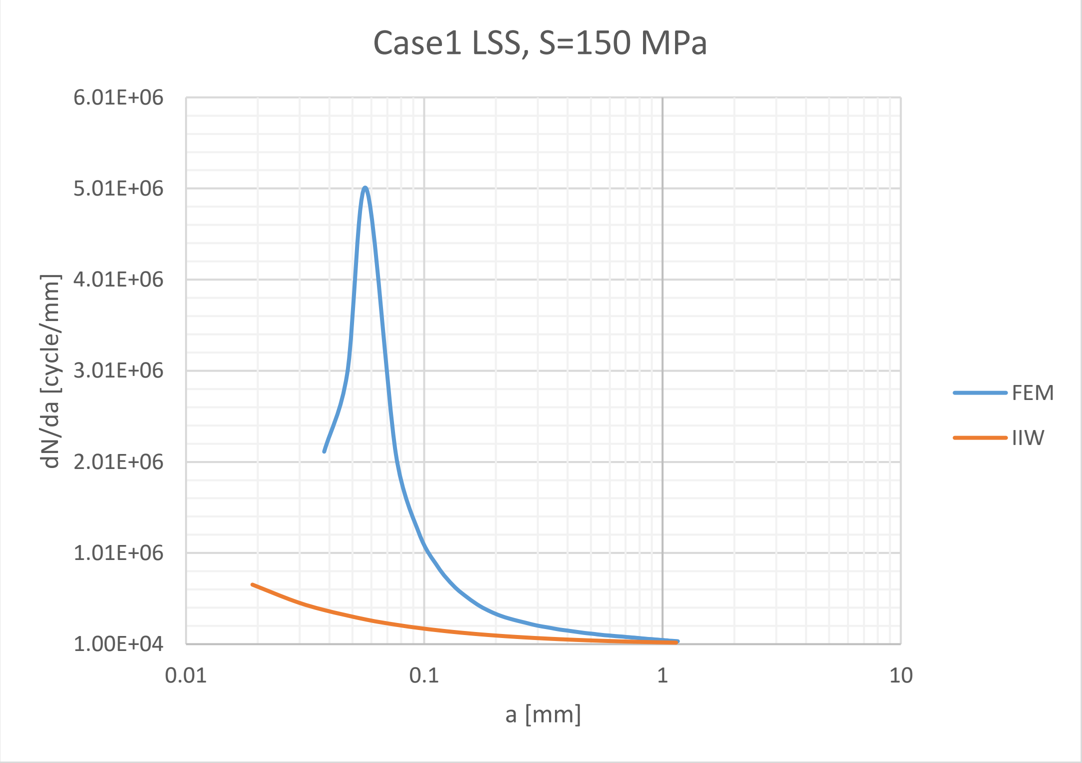

Figure 61. dN/da as a function of the crack length and the difference between FEM and IIW results

8.2.6 Fatigue Life

For each case, the discrete cycle steps until the propagated FEM simulation of 1 mm crack length were summed up to account for the fatigue life based on the FEM simulation. The life comparison of the two geometries and material models, including the short crack initiation, propagation and long crack propagation periods are shown in Figure 62, and Figure 63 and values are also presented in Table 9. However, it should be emphasised that the simulation is focusing mainly on the N_i since the final crack sizes, as discussed in Section 8.2.1 differ in most of the cases from 1 mm length.

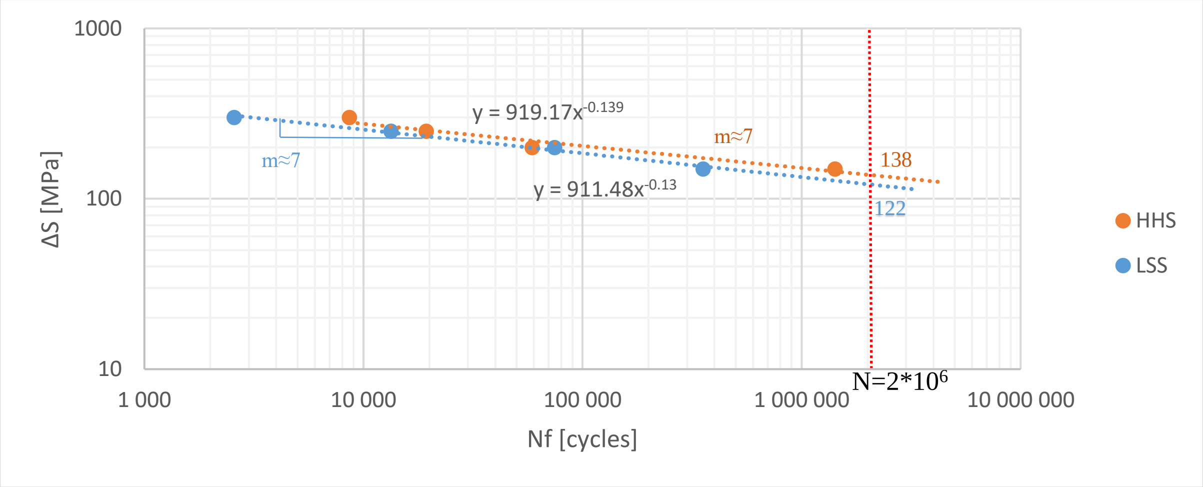

Figure 62.Case 1 estimated S-N curve

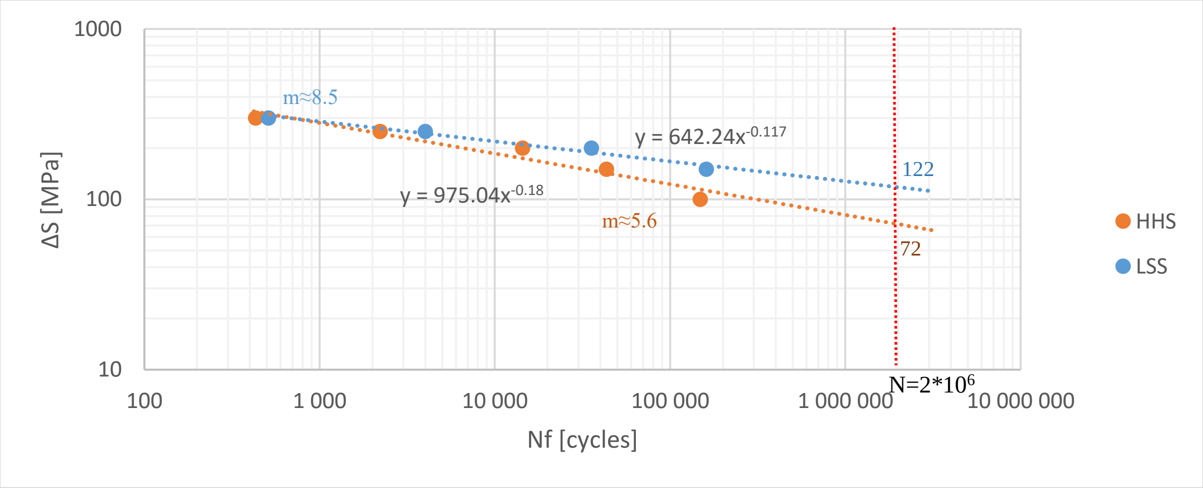

Figure 63. Case 2 estimated S-N curve

Table 9. Cycle numbers based on the FEM analysis

ΔS [MPa]	**Case 1 R=1 mm**		**Case 2 R=0.01 mm**	
	LSS	HSS	LSS	HSS
100	26 717 000	1 229 014 403	944 771	148 485
150	355 572	1 421 654	160 829	43 290
200	74 541	59 000	35 604	14 420
250	13 361	19 352	4 004	2 215
300	2 573	8 624	510	431

Along the data points, a trend line was fitted based on the power law approximation to represent failure at 50% probability level. Furthermore, this line was extended over $2*10^6$ cycles. The slope of the trend line gave the *m* value of the S-N curve and based on its equation for comparisons the stress levels were calculated at a cycle number of $2*10^6$ and presented in Table 10.

Table 10. Stress levels at 2 million cycles

	R = 1 mm	R = 0.01 mm
HSS	138 MPa	72 MPa
LSS	122 MPa	122 MPa
IIW*	104 MPa	80 MPa

**R= 1 mm estimated in full scale with grinding,*
R = 0.01 mm estimated as welded specimen in full scale

In the Case 1 (R = 1 mm) geometry model the curves show high similarity regarding the slope accounting for around m=7.2. However, for the overall fatigue life, the HSS material shows higher endurance, at 2 million cycles, compared to the LSS material.

In the Case 2 (R = 0.01 mm) geometry model, the curves show significant differences in the high cycle regime, whereas in the low cycle period the values show similarities. The LSS material model seems to have a higher m value of 8.5 compared to m=5.6 of the HSS model, resulting in a higher endurance at 2 million cycles and overall better fatigue life.

Furthermore, for comparison in the HCF regime, IIW recommended FAT class (stress levels at $2*10^6$ cycles) were included in Table 10. The recommended values for the Case 1 geometry was chosen based on the nominal stress and as in Case No. 511 [13], whereas for Case 2 geometry, grinding was assumed with a magnification factor of 1.3 [13]. These recommended stress levels at 2 million cycles is lower than both materials in Case 1 geometry, however higher than the HSS material in Case 2 geometry.

9 DISCUSSION

The topic discusses the effects of the weld toe radius in the fatigue damage process, including crack initiation and propagation up to a crack size of 1 mm, for fully penetrated cruciform joints. These effects and the damage process behaviour were investigated for two different materials, LSS and HSS.

The assessment was carried out using a strain-based local approach that governs more of the crack growth than the long crack propagation methods and was based on the findings of H. Remes [21], [26]. The theoretical overview of the principles are explained in Sections 2-6 and was implemented using softwares, Abaqus and Matlab. This fatigue process is modelled by a discrete step by step crack growth and initiation within a damaged volume. These individual crack lengths in each step were defined by the material characteristic length that considers the actual microstructure of the material and the implementation of the grain size statistics. Due to the differences between the microstructure of the two materials, LSS and HSS, the characteristic length hence the individual crack growth length is different as well. These values were two times higher in the case of LSS, $a_0 = 18.5\ \mu m$ material than the HSS one, $a_0 = 8.9\ \mu m$. The current approach also enables to consider the stress-strain state during the changes from the smooth and notched weld toe to the occurrence of a crack, as well as the changes in the damage parameter, P_{SWT}, stress triaxiality and plasticity. All the P_{SWT}, are presented in Appendix C, in general the curves expected to coincide and have similar values towards the increased crack length. This expected behaviour is well represented in Figure 56 under 150 MPa nominal load, but seem to significantly differ under the other loading conditions, behaviour was unexpected. As seen in Appendix D, this stress triaxialities for the same material coincide during the different load levels and tend to have the same behaviour. However for most load cases the LSS material has higher values than the HSS one, which trend seemed to change at the nominal load case of 300 MPa, which was unexpected. This is important since the stress triaxiality has a significant influence on the CGR.

The stress and strain results are highly dependent on the input material parameters used for the FEM simulation, as seen in Section 4. The HSS material parameters, presented in Table 1 and Figure 13 are based on the full-scale measurements, whereas the LSS material parameters were a hardness based estimate. These values were used during the FEM simulation. However, comparing the HSS and LSS strain-life curves showed different behaviour, than expected see Figure 8, and discussed in the literature [32]. In this case, strain values during the low cycle range for the HSS material were higher than the LSS. On the contrary, when the HSS parameters were estimated based on the material hardness and compared to the LSS material, as shown in Figure 14, it showed the same behaviour as in Figure 8 in line with the expectations.

This significantly different strain behaviour of the material defined based on the full-scale measurements has also an impact on the overall results that might lead to a different shape of the S-N curves, than using the material parameters defined based on the hardness estimate. Furthermore, the stress-strain curves of the different material zones in Figure 15, showed that the welding has an influence on the hardness, hence stress amplitudes. In the case of HSS material the HAZ zone has lower hardness and stress-strain values than the BM, whereas, for the LSS material the opposite was experienced, the HAZ had higher values than the BM. This further lead to visible yielding in certain cases, around the area of the two material sections (HAZ and BM) of the LSS.

For each of the individual material, and geometric model the calculated CGR seems to be in line with the IIW recommended values as seen in Figure 61 for the long crack period. However, the IIW recommended CGR is only valid for the long crack propagation period and does not give any other considerations for the initiation period, i.e. short crack growth period. Hence, the cumulative cycle numbers are significantly smaller than compared to the one from the FEM model, in terms of the fatigue life of until 1 mm. The main difference in the curves is up until a crack length of around 0.1 – 0.2 mm that is considered as the threshold length, the boundary between the initiation and long crack propagation period. In general, based on the modelling, the short crack initiation and propagation period account for around the 70-80% of the total fatigue life. In the CGR curves changes and main differences can be noticed when the local stress level raises around and over the yield stress of the considered material section. This significant difference can be realised between the two geometric cases, where the smaller toe radius, *R=0.01mm* act like a notch and results in stress levels over the yield point of the HSS and LSS material models, respectively.

Subsequently, during the intermediate long crack propagation period as well as in the period of the unstable rapid growth, the CGR behaves similarly for the similar material models. Furthermore, in the Case 2 (*R=0.01 mm*) geometry model with the HSS material showed significantly higher damage parameters than the LSS models, during the initiation period when a sudden drop and a gradual increase can also be noticed. The stress triaxialities behaved similarly for the similar material parameters regardless of the initial uncracked geometry. After a sudden increase in the values during the period of the short crack initiation, gradual changes were dominant throughout the intermediate and failure period. First, a gradual increase than a decrease was noticed. This also resulted in a noticeable sudden drop in the CGR curves, in the beginning, following with a non-linear increase before reaching the threshold crack length of the long crack propagation period.

The predicted S-N curves, shown in Figure 62 and Figure 63 were calculated based on the 1 mm simulated crack length. In the life consideration, a significant difference can be seen between the behaviours of the material in the two different geometry cases. The presence of a toe radius of 1 mm can offer a smooth transition in the stress state and smaller local stress levels. Hence, depending on the material properties, the stress state can still be under the yield point of the material zone. This can further result in higher fatigue life and endurance of the overall damage process within the period of the low and high cycle fatigue, respectively for the HSS material. The stress levels at 2 million cycles in the case of the HSS was around 138 MPa and for LSS 122 MPa, respectively. However, the damaging process seemed to have the same magnitude with the same slope, m=7.2. Significant differences can be noticed again during the low and high cycle range.

The compared IIW values are mainly based on numerous data obtained during full-scale testing at constant amplitudes. To this end, it would only give reasonable comparison at 2 million cycles for only the geometry case with R = 0.01 mm, since this toe radius is considerably close to the full scale welded joints. On the other hand, the geometry with the larger toe radius, R= 1 mm could be approximated with an ideal case when the joint is ground. In full scale, grinding could result in better fatigue life and is also considered in the recommendation. For that, IIW recommends a magnification factor of 1.3 [13]. This would further increase the endurance stress level at 2 million cycles up to max 104 MPa, which is reasonably close to the ones obtained based on the FEM simulation, as seen in Table 10. The comparison with these FAT class values is strictly valid for the HCF range.

Although the recommendation is not at all designed and does not set limit values for the LCF range, neither for the initiation period. Hence accurate comparison within this period is not possible. Thus the influence of the size of the actual toe radius is not considered either in the total life. Nevertheless, the different behaviour for both the low and high cycle periods could suggest the application of two different m values for these ranges, for a better approximation for the fatigue strength of the joint.

Different behaviour was noticed in the presence of a small *R=0.01 mm* radius that technically acts as a notch. The S-N curve of the initial uncracked geometry and its behaviour can be coupled with the other geometries regardless of the toe radius but in the presence of an assumed 0.1 mm and 0.2 mm initial cracks as shown in Figure 64 to Figure 67. These initial cracks were defined based on the overall FEM simulation and the results considering stress, strains and cycle numbers were only taken from an already existing propagated crack of 0.1 mm and 0.2 mm, respectively. Hence the crack growth path is the same than one with the uncracked geometry, but the fatigue life up until the 1 mm crack length is different since the discrete cycle numbers till the assumed initial cracks are not included in the calculation.

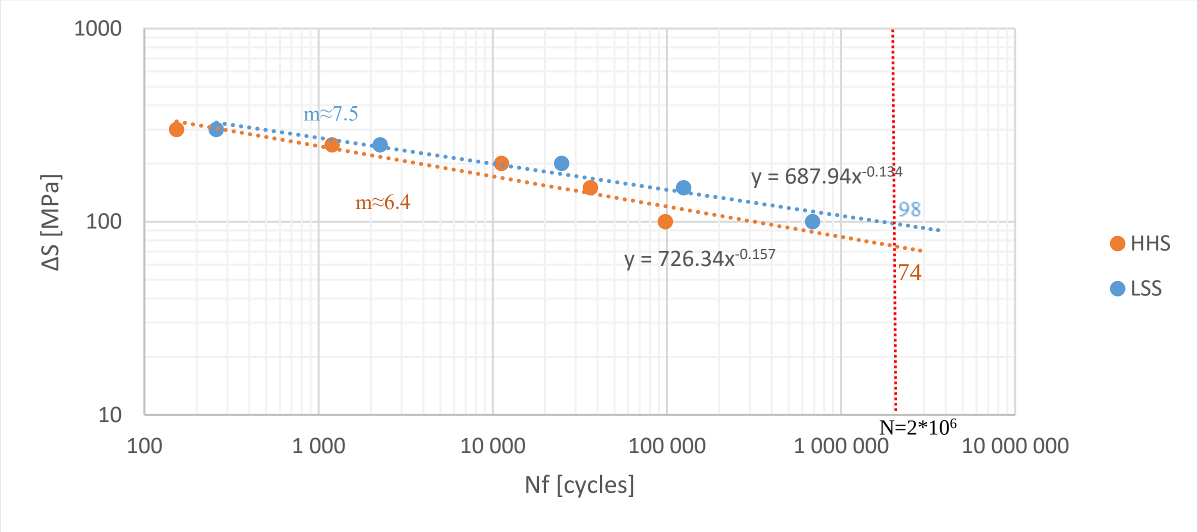

Figure 64. The estimated S-N curve for Case 2 geometry, starting from an initial crack length of 0.1 mm

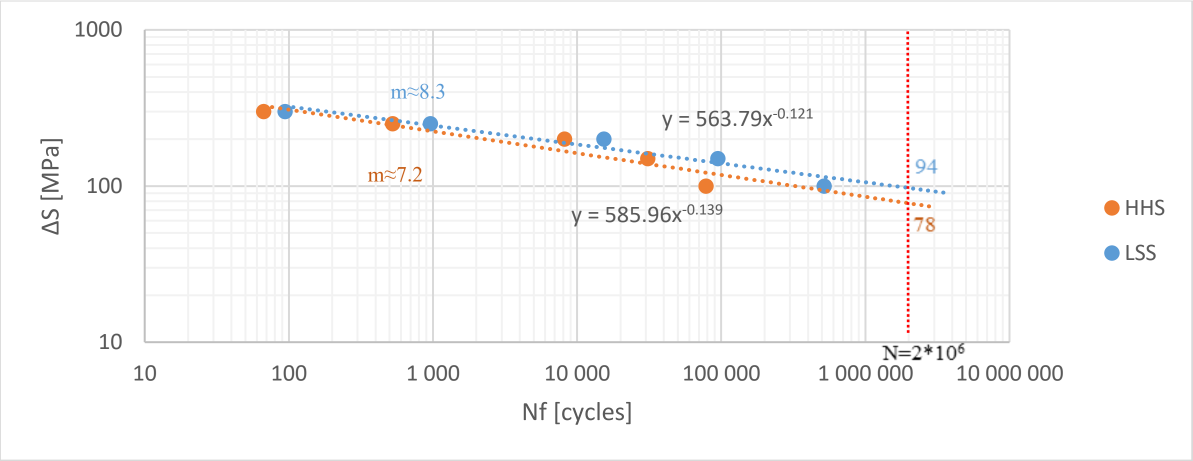

Figure 65. The estimated S-N curve for Case 2 geometry, starting from an initial crack length of 0.2 mm

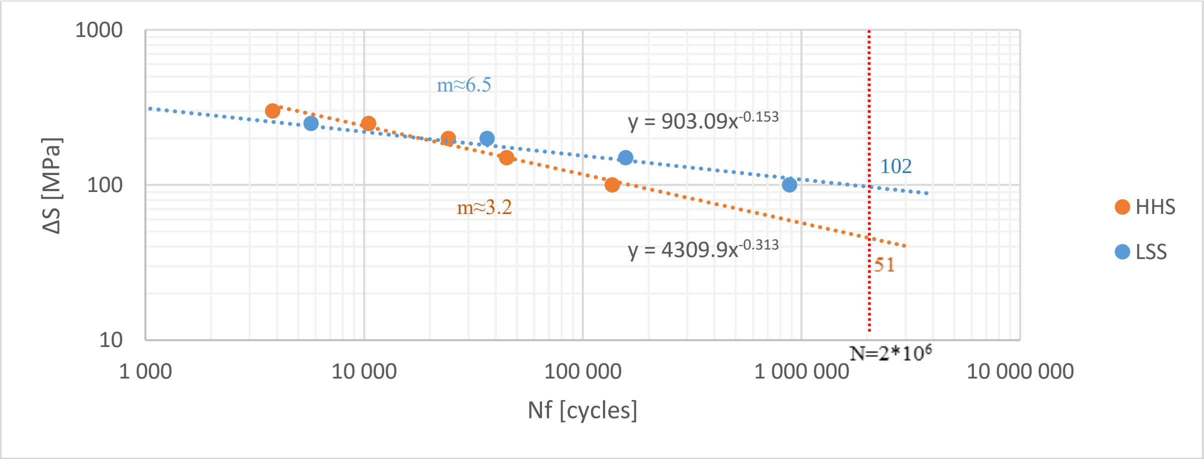

Figure 66. The estimated S-N curve for Case 1 geometry, starting from an initial crack length of 0.1 mm

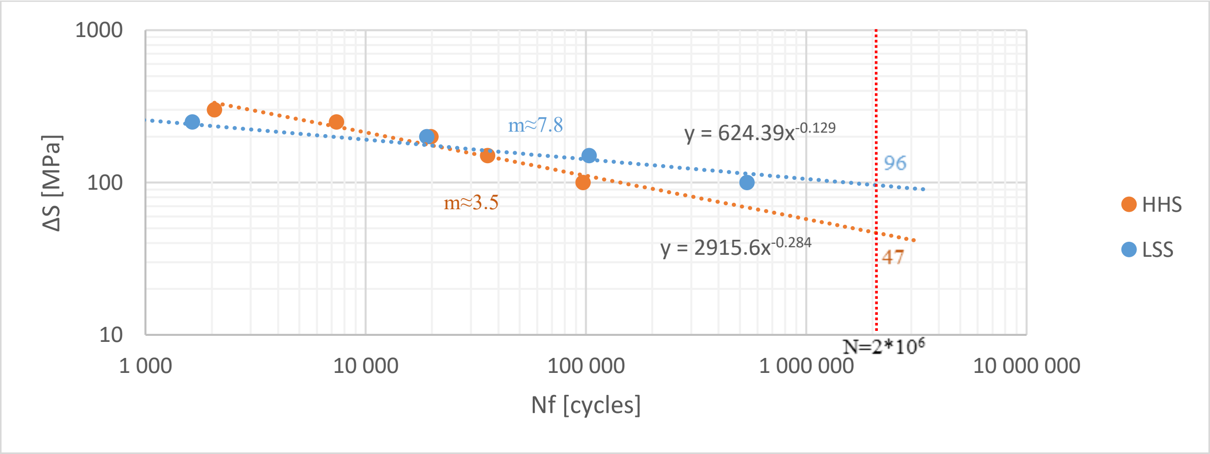

Figure 67. The estimated S-N curve for Case 1 geometry, starting from an initial crack length of 0.2 mm

In general in the presence of an initial crack, i.e. that covers the length of the actual short crack initiation and propagation period the LSS material could offer better overall fatigue resistance with higher stress levels at 2 million cycles, than the HSS. However during the low cycle period, the HSS material can offer higher cycle numbers on the same stress level, but this is rapidly decreasing in the high cycle range due to the considerably smaller *m* value. More significant differences can be seen close to the endurance limit between the two materials.

This data showed that the fatigue life of the HSS material is highly dependent on the actual geometries, due to its high sensitivity to notches and flaws on the surface and within the material. The smoother the surface or the transition is with a larger toe radius, the better fatigue resistance can be achieved with the application of the HSS material. This is due to the actual initiation period that takes up most of the total fatigue life is significantly higher than the propagation period. The latter period is in the same magnitude and similar to the LSS material model.

10 CONCLUSION

This strain based approach can be well applied to the damage process taking into consideration the actual microstructural material parameters as well as including the crack initiation and propagation periods.

The simplified, 2D plane deformation analysis under constant amplitude loading and zero residual stresses showed that with a better geometry the HSS material could be better utilised and better fatigue resistance could be achieved in the design stages. This indicates that the short crack growth period dominates, which can result in important influence on the overall fatigue life. A material having smaller grain sizes (HSS) can have an earlier start for the short crack initiation and propagation period but this period would take longer time than that of the LSS material with almost twice the size of the grain sizes.

However, due to the higher notch sensitivity of the HSS material, the fatigue life decreases considerably, in the presence of a notch or surface flaws compared to the LSS material. On the other hand, during the low cycle fatigue period, better resistance might be achieved for each geometry cases for HSS material. To this end, a good understanding of the actual load cases and estimated cycle numbers are imperative, as well as of the design scenarios where *damage tolerant, safe life, or fail-safe design* considerations might be necessary.

Unfortunately, actual material data is somewhat limited, and several material parameters were only estimated. To this end, the FEM model and results could significantly vary. Nevertheless, the estimated fatigue life, CGR, as well as the crack growth path, are in good line with the fatigue IIW recommendations for the high cycle range up to the simulated crack length of 1 mm.

The different behaviour of P_{SWT} and stress triaxialities have a strong effect on the CGR, and their effects can also be realised in the allocated separate crack growth periods. These values should be re-evaluated as it seems to have no constant behaviour and show a significant changing trend under each nominal load level. The trends of values in the TH, P_{SWT} and CGR curves showed distinctive separate behaviours for each of the damage process periods, including short crack initiation and propagation, long crack propagation and tearing-related unstable rapid growth until final failure. However to understand the material behaviour and account for more accurate results more FEM simulation with different scenarios should be carried out. The current model and the crack propagation is symmetric, hence secondary bending moments are not present, applying unsymmetrical model would result in further consideration of different stress states, as well.

For further consideration, a more accurate FEM analysis in the future can include starting from the changes in the actual weld geometries and material types till different loading conditions. The latter can include varying amplitudes and the influential effect of residual stress. These should also be incorporated into the modelling to get more comprehensive knowledge of the actual fatigue behaviour of HSS under different conditions. The simulation can also be run until the calculated critical crack length. Also to calculate an adequate brittle fracture, full-scale tests can be made to obtain the fracture toughness of the material. Furthermore, an extended 3D simulation can also be carried out to account for the 3D effect of the joint shape or present notch shapes and also further validation can be done through experiments and tests on welded specimens.

REFERENCES

[1] IMO, “IMO profile,” [Online]. Available: https://business.un.org/en/entities/13. [Accessed February 2018].

[2] ECORYS, “Study on Competitiveness of the European Shipbuilding Industry,” ECORYS, Rotterdam, 2009.

[3] BRS, “Shipping and Shipbuilding Markets,” BRS Group, 2017.

[4] IMO, “2014 Guidelines on the Method of Calculation of the Attained Energy Efficiency Design Index (EEDI) for New Ships, as amended (Resolution MEPC.245(66), as amended by resolutions MEPC.263(68) and MEPC.281(70)),” in *IMO*, London, 2017.

[5] J. Schijve, Fatigue of Structures and Materials, New York: Springer, 2009, pp. 535-559.

[6] I. Lillemäe, H. Remes, S. Liinalampi and A. Itävuo, “Influence of weld quality on the fatigue strength of thin normal and high strength steel butt joints,” *Welding in the World*, vol. 60, pp. 731-740, 2016.

[7] M. A. Meyers and K. Chawla, Mechanical Behavior of Materials, New York: Cambridge University Press, 2009, pp. 713-765.

[8] A. Hobbacher, B. Jonsson, G. Dobmann, M. Kassner and G. Marquis, IIW Guidelines on Weld Quality in Relationship to Fatigue Strength, International Institute of Welding, Springer, 2016.

[9] D. Radaj, Design and Analysis of Fatigue Resistant Welded Structures, Cambridge: Woodhead Publishing Limited, 1990.

[10] W. Cui, “A state-of-the-art review on fatigue life prediction methods for metal structures,” *Maritime Science and Technology*, vol. 7, pp. 43-56, 2002.

[11] W. Fricke, “Fatigue analysis of welded joints:state of development,” *Marine Structures*, vol. 16, pp. 185-200, 2002.

[12] D. Radaj, C. Sonsino and W. Fricke, Fatigue Assessment of Welded Joints by Local Approaches, Cambridge: Woodhead Publishing, 2006.

[13] A. F. Hobbacher, Recommendations for Fatigue Design of Welded Joints and Components, London: Springer, IIW, 2016.

[14] D. Radaj, C. Sonsino and W. Fricke, “Recent developments in local concepts of fatigue assessment of welded joints,” *International Journal of Fatigue*, vol. 31, pp. 2-11, 2009.

[15] H. Remes, J. Jelovica, J. Romanoff, P. Lehto and S. Liinalampi, “Fatigue strength modelling of high-performance welds using local approaches,” in *Practical Design of Ships and Other Floating Structures* , Copenhagen, 2016.

[16] T. Lagoda, “Energy models for fatigue life estimation under uniaxial random loading I.-II.,” *International Journal of Fatigue,* vol. 23, pp. 467-480, 2001.

[17] N. E. Dowling, Mechanical Behavior of Materials (4th Edition), Essex: Pearson, 2013.

[18] H. Remes, Doctoral Dissertation: Strain-based approach to fatigue strength assessment of laser-welded joints, Espoo: Helsinki University of Technology, 2008.

[19] “eFatigue,” [Online]. Available: https://www.efatigue.com/training/Strain_Life_Method.pdf. [Accessed February 2018].

[20] F. V. Lawrence, R. J. Mattos, Y. Higashide and J. D. Burk, “Estimating the fatigue crack initiation life of welds,” in *ASTM STP648, Fatigue testing of weldments,* Philadelphia, ASTM, 1978, pp. 134-158.

[21] H. Remes, “Strain -based approach to fatigue crack initiation and propagation in welded steel joints with arbitrary notch shape,” *International Journal of Fatigue,* vol. 52, pp. 114-123, 2013.

[22] S. Mikheevskiy, G. Glinka and T. Cordes, “Total life approach for fatigue life estimation of welded structures,” *Procedia Engineering,* vol. 101, pp. 177-184, 2015.

[23] N. E. Dowling, “Mean Stress Effects in Stress-Life and Strain-Life Fatigue,” *Society of Automotive Engineers,* 2004.

[24] K. Miller, “A historical perspective of the important parameters of metal fatigue; and problems for the next century,” in *International fatigue conference; Fatigue'99,* Beijing, 1999.

[25] S. Liinalampi, H. Remes, P. Lehto, I. Lillemäe, J. Romanoff and D. Porter, “Fatigue strength analysis of laser-hybrid welds in thin plate considering weld geometry in microscale,” *International Journal of Fatigue,* vol. 87, pp. 143-152, 2016.

[26] H. Remes, P. Varsta and J. Romanoff, “Continuum approach to fatigue crack initiation and propagation in welded steel joints,” *International Journal of Fatigue,* vol. 40, pp. 16-26, 2012.

[27] P. Lehto, H. Remes, T. Saukkonen, H. Hänninen and J. Romanoff, “Influence of grain size distribution on the Hall–Petch relationship of welded structural steel,” *Material Science and Engineering,* vol. 592, pp. 28-39, 2014.

[28] P. Lehto, J. Romanoff, H. Remes and T. Saikka, “Characterisation of local grain size variation of welded structural steel,” *Welding in the World,* vol. 60, pp. 673-688, 2016.

[29] A. Ekberg, “Multiaxial Fatigue,” Chalmers University of Technology, Gothenburg, 2016.

[30] M. Roessle and A. Fatemi, “Strain-controlled fatigue properties of steels and some simple approximations,” *International Journal of Fatigue,* vol. 22, pp. 495-511, 2000.

[31] B. Goo and S. Yang, “Fatigue Life Evaluation of Welded Joints by a Strain-life Approach Using Hardness and Tensile Strength,” *Mechanical Science and Technology,* vol. 20, no. 1, pp. 42-50, 2006.

[32] H. Mughrabi and H. W. Höppel, “Cyclic deformation and fatigue properties of very fine-grained metals and alloys,” *International Journal of Fatigue,* vol. 32, pp. 1413-1427, 2010.

[33] H. Kim, M. Choi, C. Chung and D. H. Shin, “Fatigue properties of ultrafine grained low carbon steel produced by equal channel angular pressing,” *Material Science and Engineering,* vol. 340, pp. 243-250, 2003.

[34] P. Cavaliere, “Fatigue properties and crack behavior of ultra-fine and nanocrystalline pure metals,” *International Journal of Fatigue,* vol. 31, pp. 1476-1489, 2009.

[35] P. Lehto, “Grain size measurement using Matlab,” [Online]. Available: https://wiki.aalto.fi/display/GSMUM/Grain+size+measurement+using+Matlab. [Accessed 23 January 2018].

[36] A. M. P. d. Jesus, R. Matos, B. F. C. Fontoura, C. Rebelo, L. S. d. Silva and M. Veljkovic, “A comparison of the fatigue behavior between S355 and S690 steel grades,” *Journal of Constructional Steel Research,* vol. 79, pp. 140-150, 2012.

[37] B. Bialobrzeska, L. Konat and R. Jasinski, *The Influence of Austenite Grain Size on the Mechanical Properties of Low-Alloy Steel with Boron,* Wroclaw: Wroclaw University of Technology, 2017.

[38] B. Jung, H. Lee and H. Park, “Effect of grain size on the indentation hardness for polycrystalline materials by the modified strain gradient theory,” *International Journal of Solids and Structures,* vol. 50, pp. 2719-2724, 2013.

[39] G. Magudeeswaran, V. Balasubramanian, G. M. Robby and T. S. Balasubramanian, “Effect of Welding Processes and Consumables on Tensile and Impact Properties of High Strength Quenched and Tempered Steel Joints,” *Journal of Iron and Steel Research,* vol. 15, no. 6, pp. 87-94, 2008.

[40] S. R. Nathan, V. Balasubramanian, S. Malarvizhi and A. Rao, “Effect of welding processes on mechanical and microstructural characteristics of high strength low alloy naval grade steel joints,” *Defence Technology,* vol. 11, pp. 308-317, 2015.

[41] C. Chen, M. Zhao, T. Fung, S. P. Chiew and C. Lee, “Influence of welding on mechanical properties of high strength steel butt joints,” *Proceedings of Eurosteel 2017,* vol. 1, no. 2-3, pp. 3567-3576, 2017.

[42] ARC, “Arc Specialties,” 2017. [Online]. Available: http://arcspecialties.com/wp-content/uploads/2017/06/Essential-Variables-for-SAW-CRO-Welding.pdf. [Accessed February 2018].

[43] E. Mikkola, “Doctoral Dissertation: A study on effectiveness limitations of high-frequency mechanical impact,” Aalto University, Espoo, 2016.

[44] S. J. Maddox, Fatigue strength of welded structures, Cambridge: Abington, 1991.

[45] B. Schork, P. Kucharczyk, M. Madia, U. Zerbst, J. Hensel, J. Bernhard, D. Tchuiundjang, M. Kaffenberger and M. Oechsner, “The effect of the local and global weld geometry as well as material defects on crack initiation and fatigue strength,” Engineering Fracture Mechanics, 2017.

[46] V. Caccese, P. A. Blomquist, K. A. Berube, S. R. Webber and N. J. Orozco, “Effect of weld geometric profile on fatigue life of cruciform welds made by laser/GMAW processes,” *Marine Structures,* vol. 19, pp. 1-22, 2006.

[47] TWI, “Fillet weld size determination,” TWI, [Online]. Available: https://www.twi-global.com/technical-knowledge/faqs/faq-how-do-you-determine-the-minimum-size-of-a-fillet-weld/. [Accessed February 2018].

[48] V. Balasubramanian and B. Guha, “Influence of weld size on fatigue crack growth characteristics of flux cored arc welded cruciform joints,” *Materials Science and Engineering,* vol. 265, no. 1-2, pp. 7-17, 1999.

[49] P. J. Singh, D. R. G. Archar, B. Guha and H. Nordberg, “Fatigue life prediction of gas tungsten arc welded AISI 304L cruciform joints with different LOP sizes,” *International Journal of Fatigue,* vol. 25, no. 1, pp. 1-7, 2003.

[50] S. Kainuma and I. T. Kim, “Fatigue strength evaluation of load-carrying cruciform fillet-welded joints made with mild steel plates of different thickness,” *International Journal of Fatigue,* vol. 27, no. 7, pp. 810-816, 2005.

[51] C. H. Lee, K. H. Chang, G. C. Jang and C. Y. Lee, “Effect of weld geometry on the fatigue life of non-load-carrying fillet welded cruciform joints,” *Engineering Failure Analysis,* vol. 16, pp. 849-855, 2009.

[52] T. Nykänen, G. Marquis and T. Björk, “Fatigue analysis of non-load-carrying fillet welded cruciform joints,” *Engineering Fracture Mechanics,* vol. 74, pp. 399-415, 2007.

[53] L. Zong, G. Shi, Y. Q. Wang, Z. X. Li and Y. Ding, “Experimental and numerical investigation on fatigue performance of non-load-carrying fillet welded joints,” *Journal of Constructional Steel Research,* vol. 130, pp. 193-201, 2017.

[54] H. Remes and P. Varsta, “Statistics of Weld Geometry for Laser-Hybrid Welded Joints and its Application within Notch Stress Approach,” *Welding in the World,* vol. 54, no. 7-8, pp. 189-207, 2010.

[55] B. F. Mechanics, “Global Wave Statistics,” 2011. [Online]. Available: http://www.globalwavestatisticsonline.com/Help/wave_scatter.htm. [Accessed January 2018].

[56] Aalto University, *Kul-24.4120 Ship Structural Design (P), Lecture 4 - Statistical Treatment of Ship Response due to Global and Local Loads,* Espoo: Aalto University, 2016.

[57] J. Kozak and Z. Gorski, “Fatigue strength determination of ship structural joints,” *Polish Maritime research,* vol. 18, no. 69, pp. 28-36, 2011.

[58] DNV-GL, “Fatigue Assessment of Ship Structures”. Patent No. 30.7, April 2014.

[59] D. P. Kihl and S. Sarkani, “Mean stress effects in fatigue of welded steel joints,” *Probabilistic Engineering Mechanics,* vol. 14, pp. 97-104, 1999.

[60] A. Ince and G. Glinka, “A modification of Morrow and Smith-Watson-Topper mean stress correction models,” *Fatigue and Fracture of Engineering Materials and Structures,* vol. 34, pp. 854-867, 2011.

[61] R. H. Leggatt, “Residual stresses in welded structures,” *International Journal of Pressure Vessels and Piping,* vol. 85, pp. 144-151, 2008.

[62] W. Fricke, “Effect of residual stresses on the fatigue behaviour of welded steel structures,” *Werkstifftech,* vol. 36, no. 11, pp. 642-649, 2005.

[63] Y. Morikage, S. Igi, K. Oi, Y. Jo, K. Murakami and K. Gotoh, “Effect of Compressive Residual Stress on Fatigue Crack Propagation,” *Procedia Engineering,* vol. 130, pp. 1057-1065, 2015.

[64] M. Farajian, T. N. Pagel and K. Dilger, “Mechanisms of Residual Stress Relaxation and Redistribution in Welded High-Strength Steel Specimens under Mechanical Loading,” *Welding in the World,* vol. 54, no. 11-12, pp. 366-374, 2010.

[65] T. Teng and P. Chang, “Effect of residual stresses on fatigue crack initiation life for butt-welded joints,” *Journal of Materials Processing Technology,* vol. 145, pp. 325-335, 2004.

[66] A. Fatemi, *Residual Stresses and Their Effects on Fatigue Resistance,* University of Toledo, Ohio, USA.

[67] C. Liljedahl, O. Zanellato, M. Fitzpatrick, J. Lin and L. Edwards, “The effect of weld residual stresses and their re-distribution with crack growth during fatigue under constant amplitude loading,” *International Journal of Fatigue,* vol. 32, pp. 735-743, 2010.

[68] L. Edwards, “Influence of residual stress redistribution on fatigue crack growth and damage tolerant design,” *Materials Science Forum,* Vols. 524-525, 363-372 September 2006.

[69] M. Fitzpatrick and L. Edwards, “Fatigue Crack/Residual Stress Field Interactions and Their Implications for Damage-Tolerant Design,” *Journal of Materials Engineering and Performance,* vol. 7, no. 2, pp. 190-198, 1998.

[70] S. Y. Kenno, S. Das, J. B. Kennedy, R. B. Rogge and M. Gharghouri, “Residual stress distributions on ship hull specimens,” *Marine Structures,* vol. 23, pp. 263-273, 2010.

[71] Q. Wang, X. Liu, Z. Yan, Z. Dong and D. Yan, “On the mechanism of residual stresses relaxation in welded joints under cyclic loading,” *International Journal of Fatigue,* vol. 105, pp. 43-59, 2017.

[72] M. Farajian, T. Pagel and K. Dilger, “Residual Stress Relaxation of Quasi-Statically and Cyclically-Loaded Steel Welds,” *Welding in the World,* vol. 54, no. 1-2, pp. 49-60, 2010.

[73] M. Shama, Buckling of Ship Structures, Berlin: Springer, 2013.

[74] Z. Qian, S. Chumbley, T.Karakulak and E. Johnson, “The residual stress relaxation behavior of weldments during cyclic loading,” *Metallurgical and Materials Transaction,* vol. 44, pp. 3147-3156, 2013.

[75] P. J. Aalbertsa and M. W. Nieuwenhuijs, “Full Scale Wave and Whipping Induced Hull Girder Loads,” in *Hydroelasticity in Marine Technology,* Wuxi, 2006.

[76] W. Z. Zhuang and G. R. Halford, “Investigation of residual stress relaxation under cyclic load,” *International Journal of Fatigue,* vol. 23, pp. 31-37, 2001.

[77] L. Gannon, Y. Liu, N. Pegg and M. J. Smith, “Effect of welding-induced residual stress and distortion on ship hull girder ultimate strength,” *Marine Structures,* vol. 28, pp. 25-49, 2012.

[78] M. Leitner, M. Khurshid and Z. Barsoum, “Stability of high frequency mechanical impact (HFMI) post-treatment, induced residual stress states under cyclic loading of welded steel joints,” *Engineering Structures,* vol. 143, pp. 589-602, 2017.

[79] U. Kuhlmann, H.-P. Gunther and C. Rasche, “High-strength steel fillet welded connections,” *Steel Construction 1* , 2008.

[80] M. Khurshid, Z. Barsoum and N. Mumtaz, “Ultimate strength and failure modes for fillet welds in high strength steels,” *Materials and Design,* vol. 40, pp. 36-42, 2012.

[81] W. Fricke, “IIW Guideline for the Assessment of Weld Root Fatigue,” *Welding in the World,* vol. 57, pp. 753-791, 2013.

[82] C. M. Sonsino, W. Fricke, F. d. Bruyne, A. Hoppe, A. Ahmadi and G. Zhang, “Notch stress concepts for the fatigue assessment of welded joints - Background and applications,” *International Journal of Fatigue,* vol. 34, pp. 2-16, 2012.

[83] A. Al-Mukhtar, H. Biermann, S. Henkel and P. Hubner, “Comparison of the Stress Intensity Factor of Load-Carrying Cruciform Welded Joints with Different Geometries,” *Journal of Materials Engineering and Performance,* vol. 19, no. 6, pp. 802-809, 2010.

[84] A. M. Al-Mukhtar, S. Henkel, H. Biermann and P. Hubner, “A Finite Element Calculation of Stress Intensity Factors of Cruciform and Butt Welded Joints for Some Geometrical Parameters,” *Jordan Journal of Mechanical and Industrial Engineering,* vol. 3, pp. 236-245, 2009.

[85] P. Ljustell, “Large Scale Yielding Fatigue Crack Growth, A Literature Survey,” KTH School of Engineering Sciences, Stockholm, 2007.

APPENDIX A –INTACT GEOMETRY

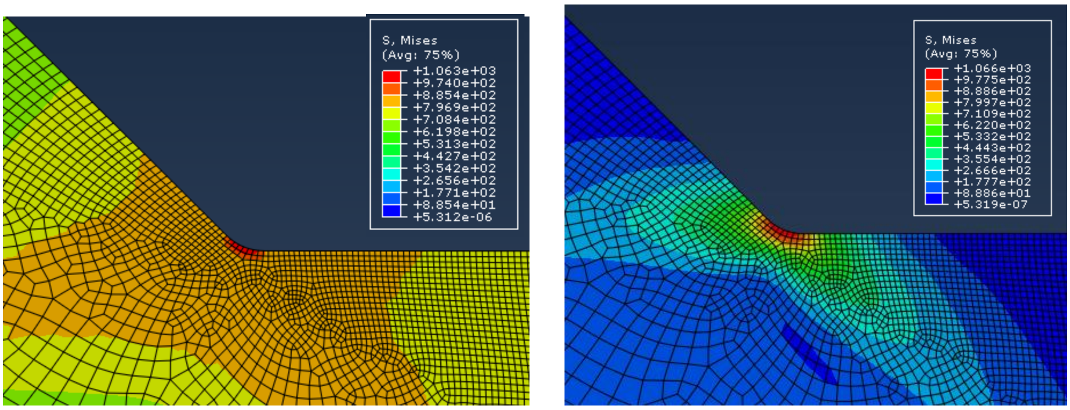

Case 2 HSS top (left) and bottom (right) of the cycle, ΔS=300 MPa, cycle No: 5

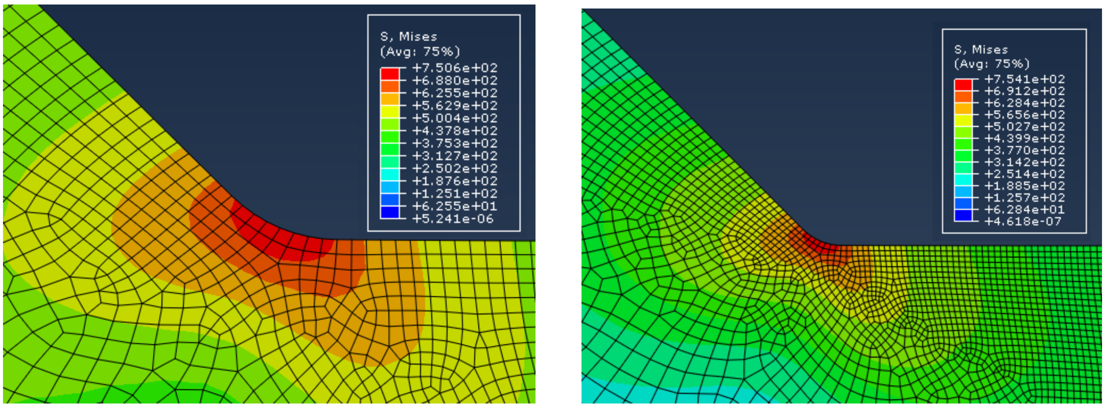

Case 2 LSS top (left) and bottom (right) of the cycle, ΔS=300 MPa cycle No: 5

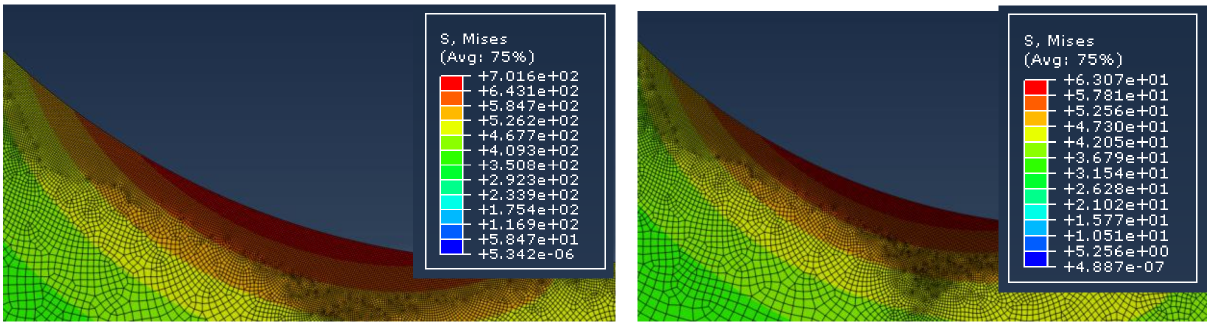

Case1 HSS top (left) and bottom (right) of the cycle, ΔS=300 MPa, cycle No: 5

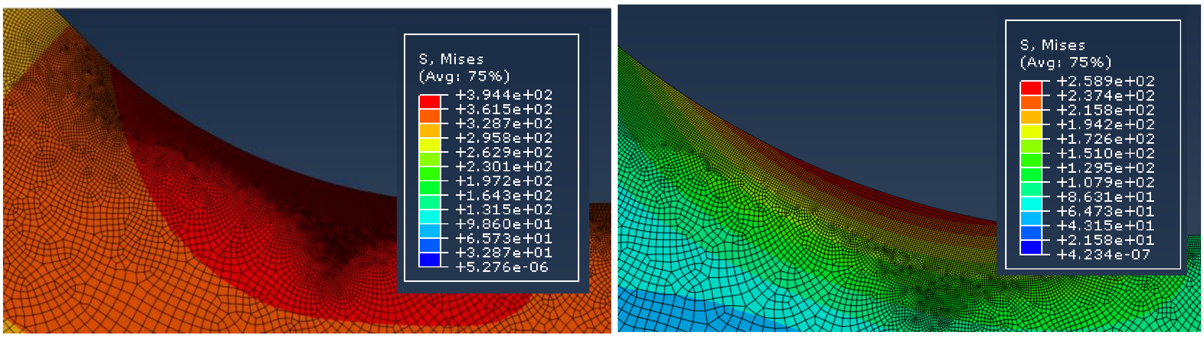

Case1 LSS top (left) and bottom (right) of the cycle, ΔS=300 MPa, cycle No: 5

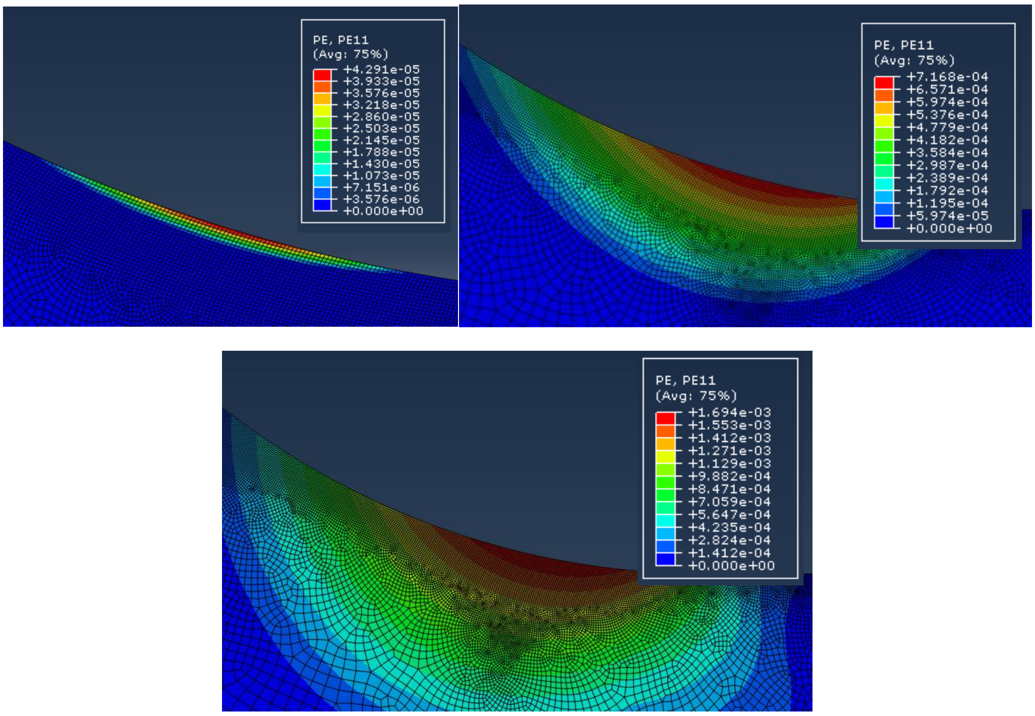

Case 1, LSS plastic strain distribution under nominal load level, 150, 200, 250 MPa, cycle No: 5

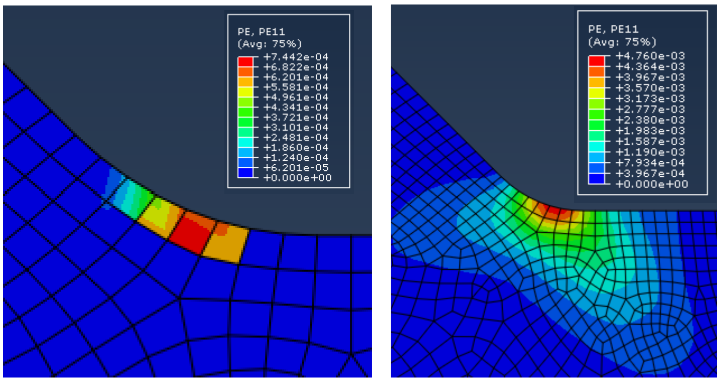

Case 2, HSS (left) and LSS (right) plastic strain distribution under nominal load level, 100 MPa, cycle No: 5

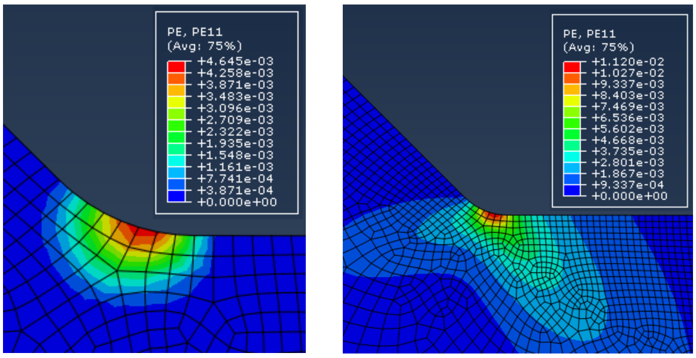

Case 2, HSS (left) and LSS (right) plastic strain distribution under nominal load level, 150 MPa, cycle No: 5

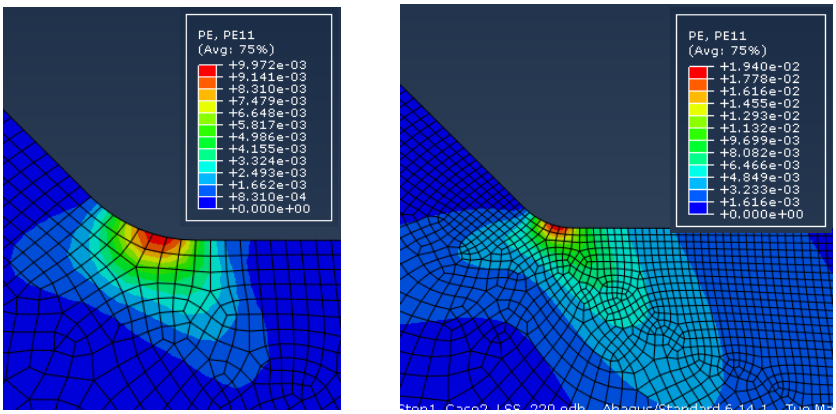

Case 2, HSS (left) and LSS (right) plastic strain distribution under nominal load level, 200 MPa, cycle No: 5

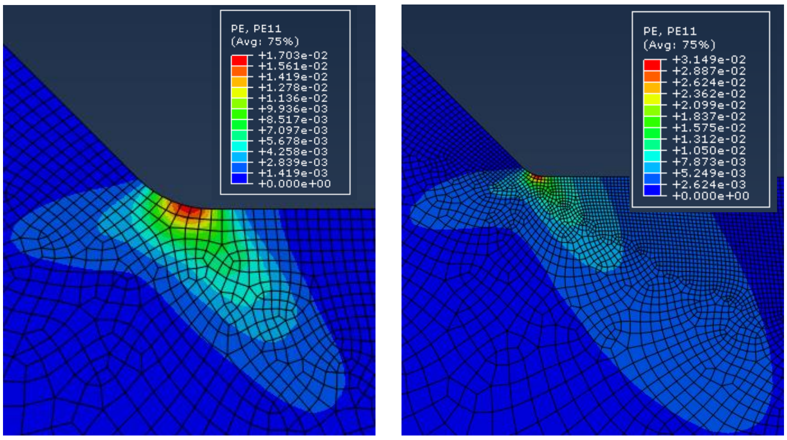

Case 2, HSS (left) and LSS (right) plastic strain distribution under nominal load level, 250 MPa, cycle No: 5

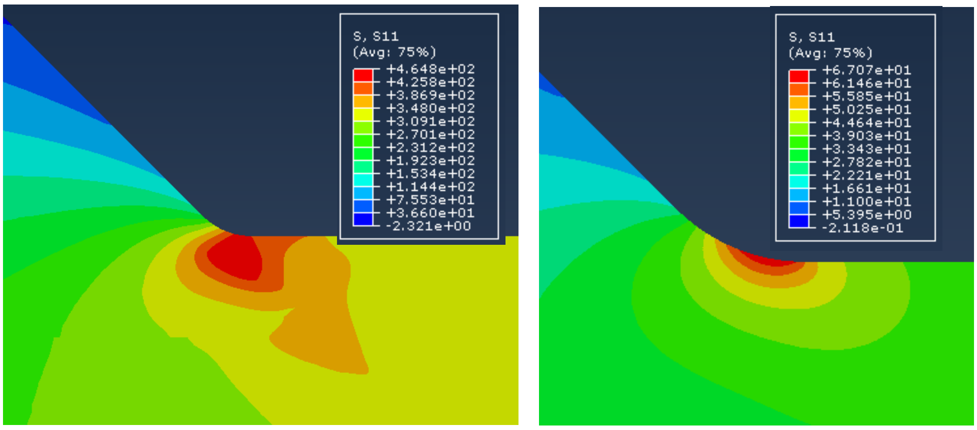

Normal distribution of Case 1 HSS at top (a) and bottom (b) of the cycle no:5, S=300 MPa

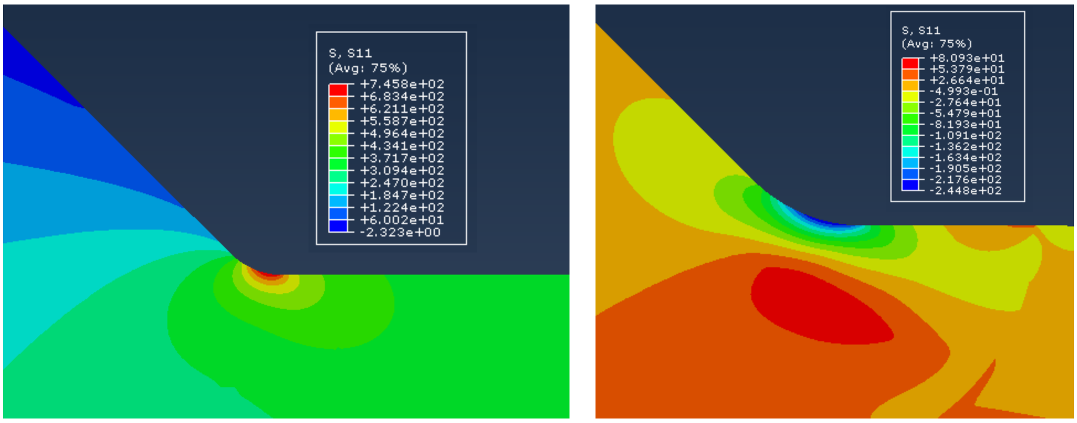

Normal stress distribution of Case 1 LSS at top (left) and bottom (right) of the cycle no:5, S=300 MPa

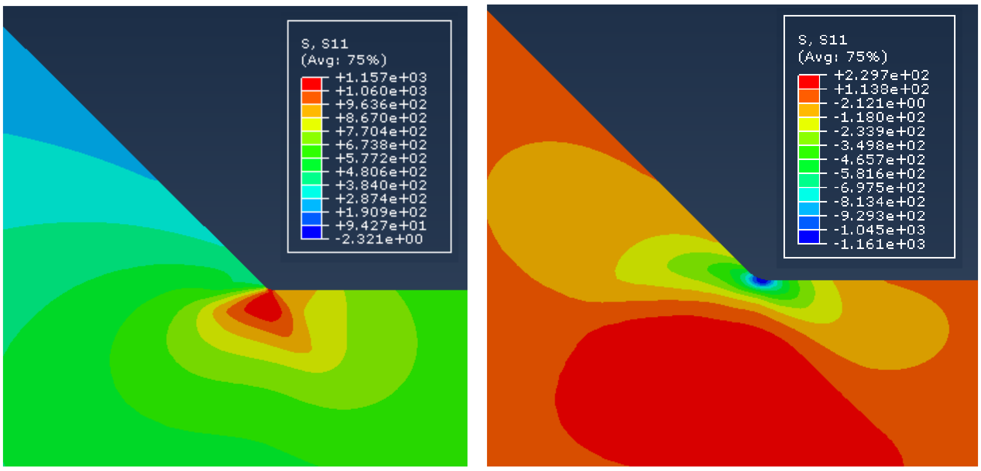

Normal stress distribution of Case 2 HSS at top (a) and bottom (b) of the cycle no:5, S=300 MPa

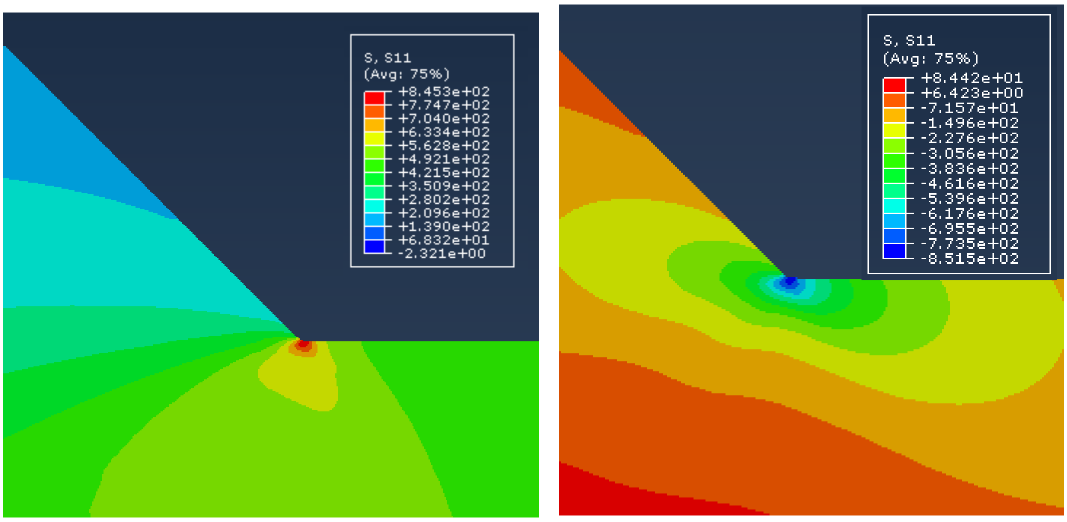

Normal stress distribution of Case 2 LSS at top (a) and bottom (b) of the cycle no:5, S=300 MPa

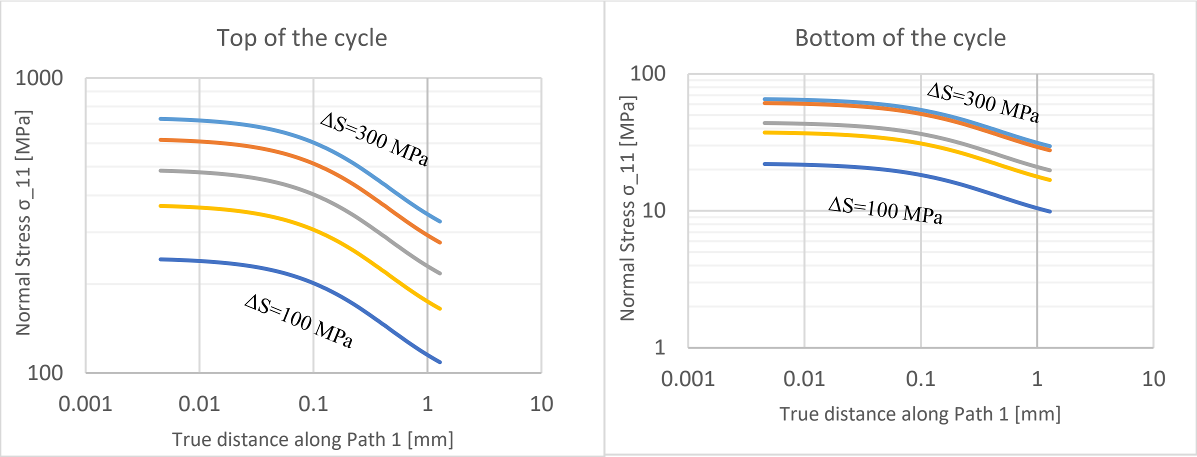

Case 1, HSS, Stress σ_{11} versus distance from the weld toe along Path at the top and bottom of the cycle no:5 for different nominal stress level

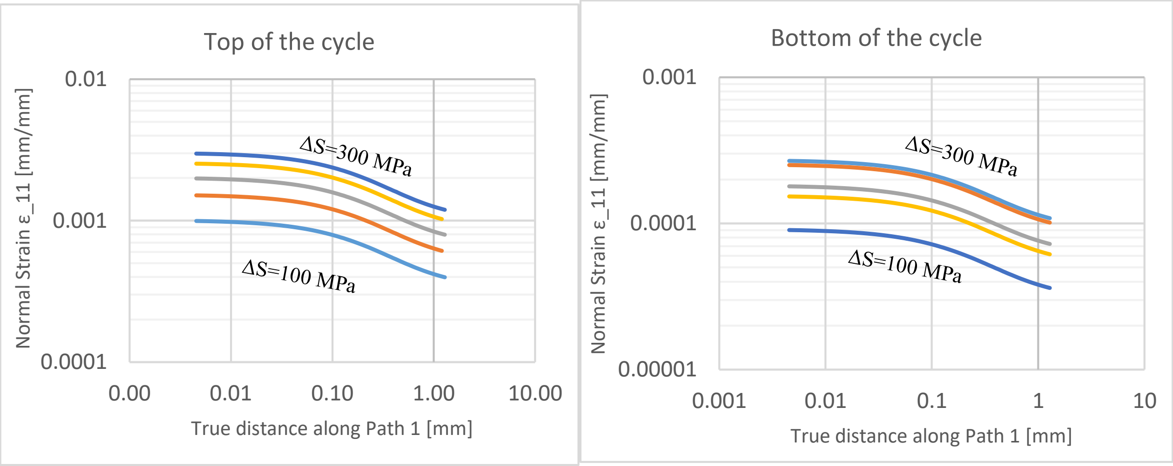

Case 1, HSS, Strain ε_{11} versus distance from the weld toe along Path at the top and bottom of the cycle no:5 for different nominal stress level

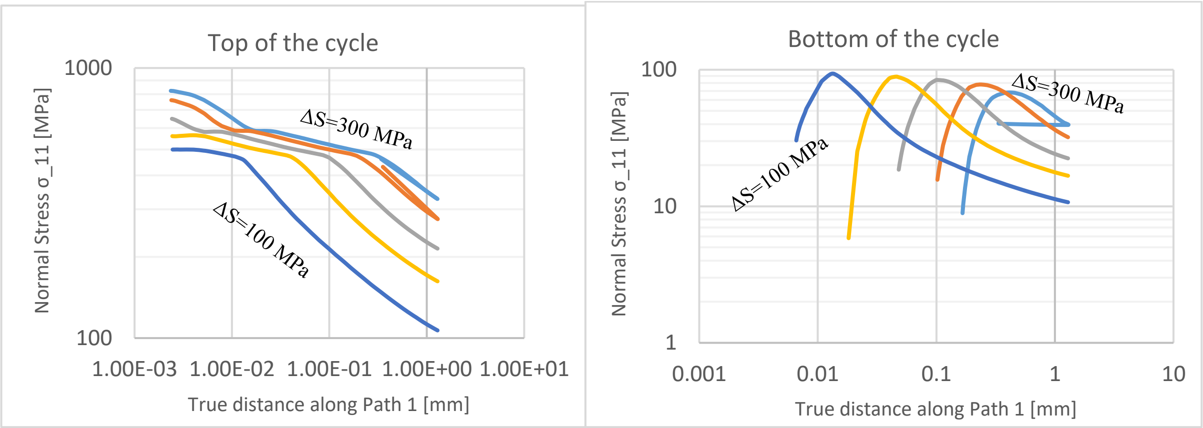

Case 2, LSS, Stress σ_{11} versus distance from the weld toe along Path at the top and bottom of the cycle no:5 for different nominal stress level

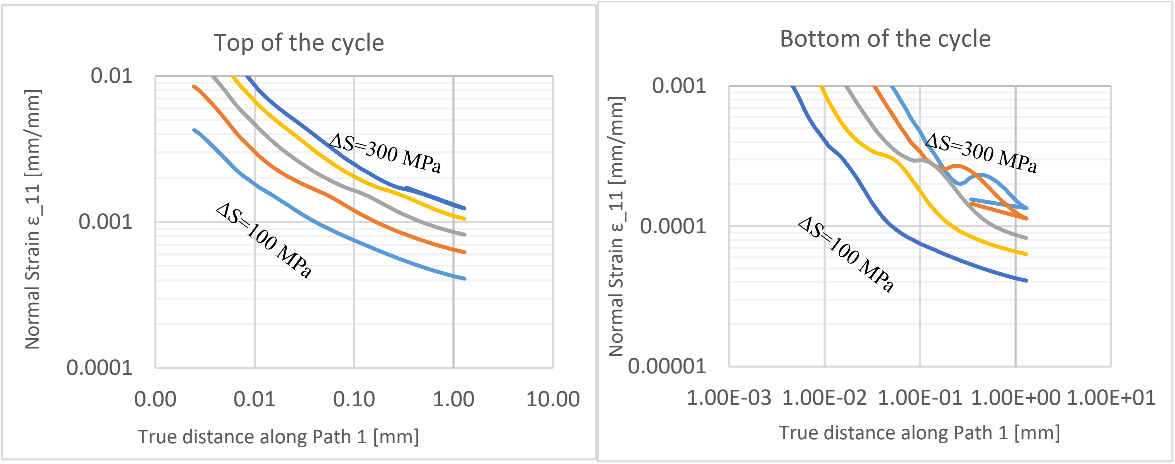

Case 2, LSS, Strain ε_{11} versus distance from the weld toe along Path 1 at the top and bottom of the cycle no:5 for different nominal stress level

APPENDIX B – PROPAGATED CRACK

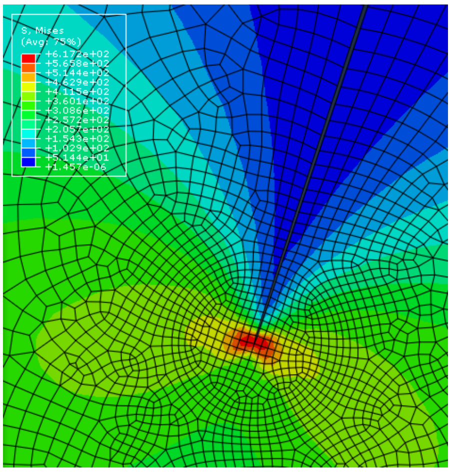

von Mises stress of Case 1, LSS top of the cycle under S=100 MPa nominal load a=0.1 mm, n=10

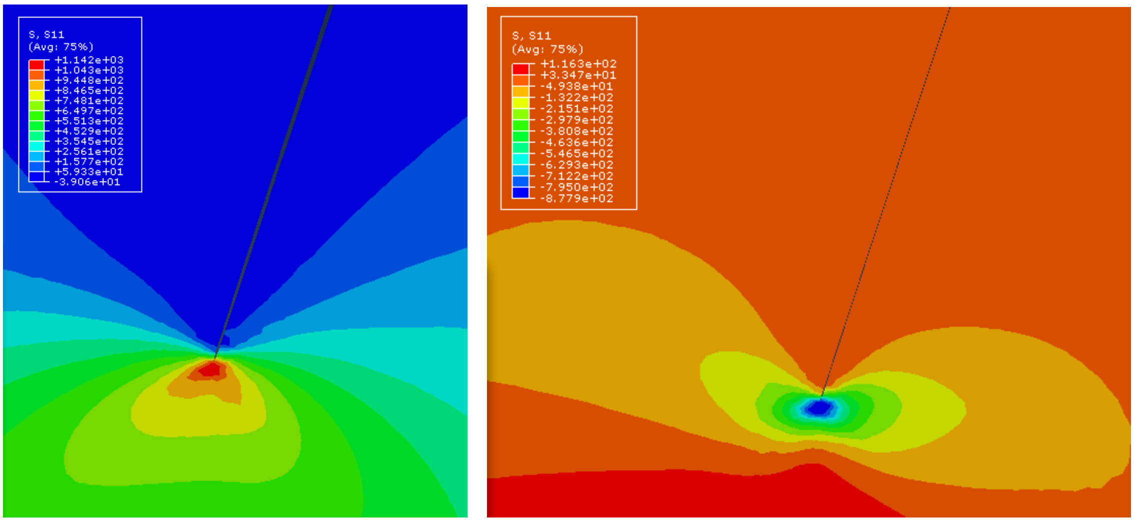

Normal stress distribution of Case1 LSS at top (left) and bottom (right) of the cycle under S=100 MPa nominal load a=0.1 mm, n=10

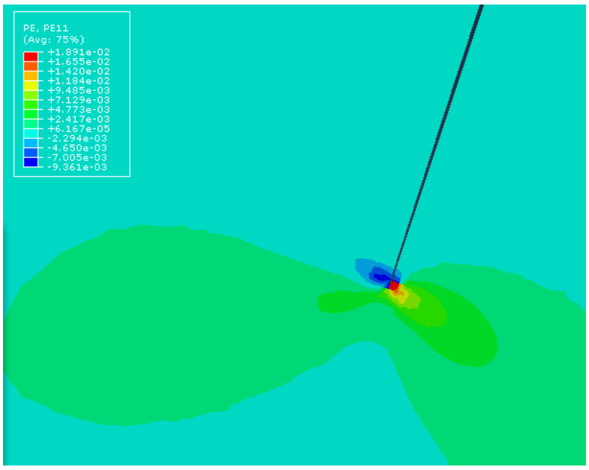

Plastic strain zone of Case 1 LSS at top of the cycle under S=100 MPa nominal load a=0.1 mm, n=10

APPENDIX C – P_{SWT} DAMAGE PARAMETER

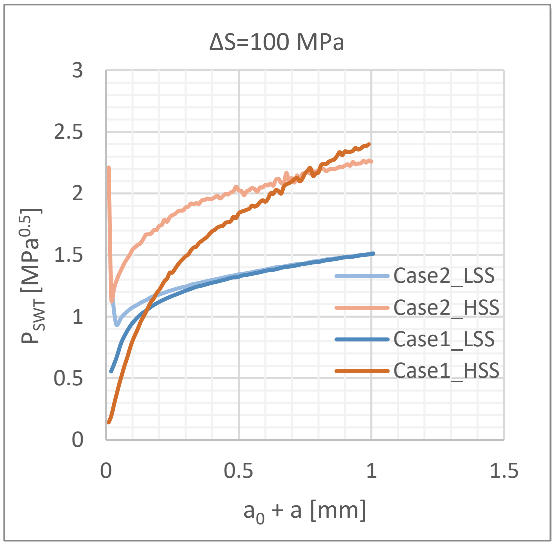

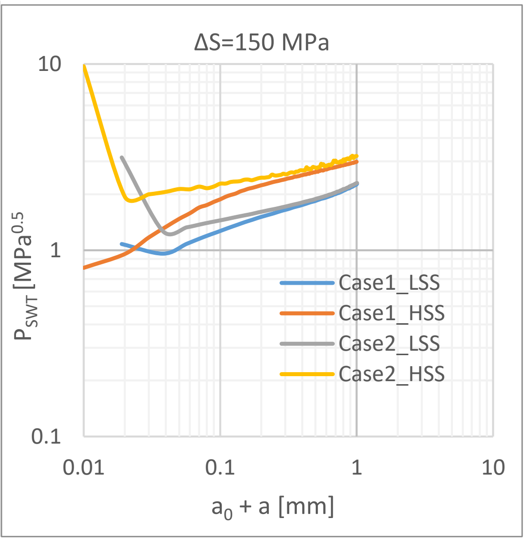

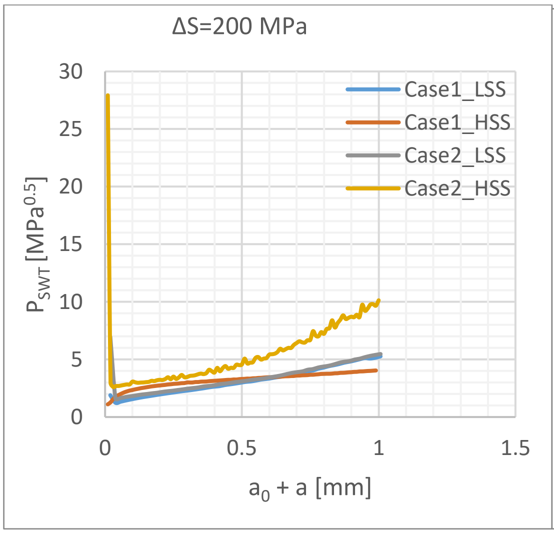

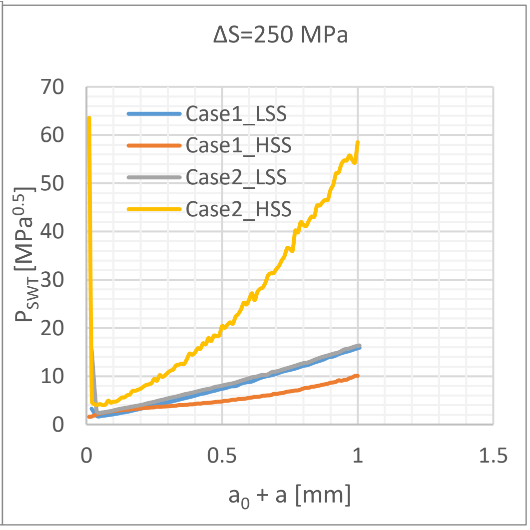

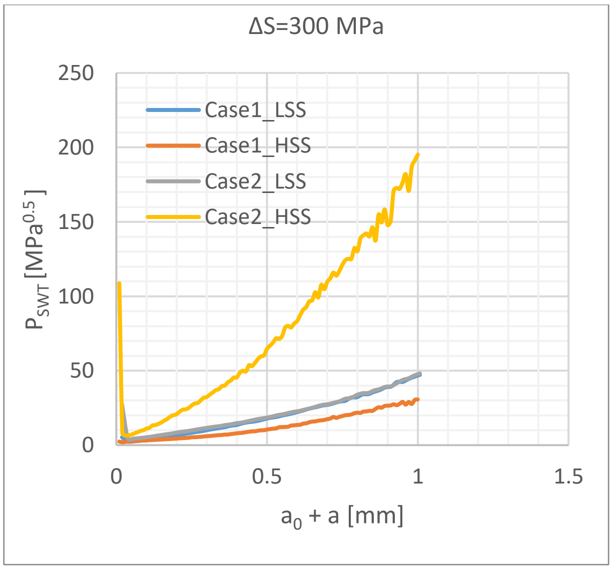

APPENDIX D – STRESS TRIAXIALITIES

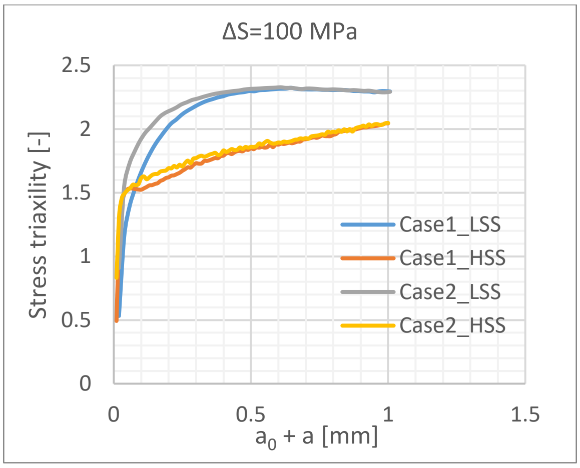

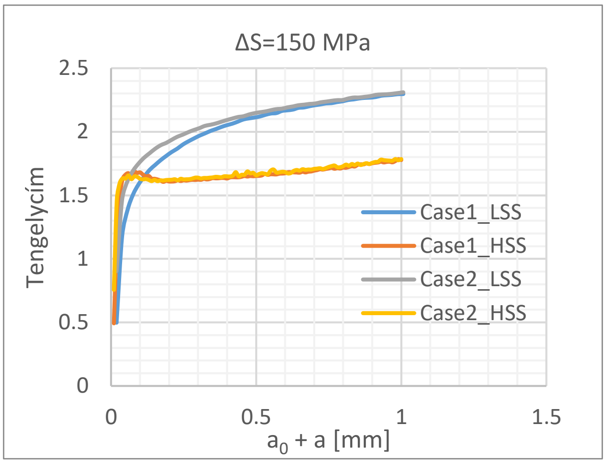

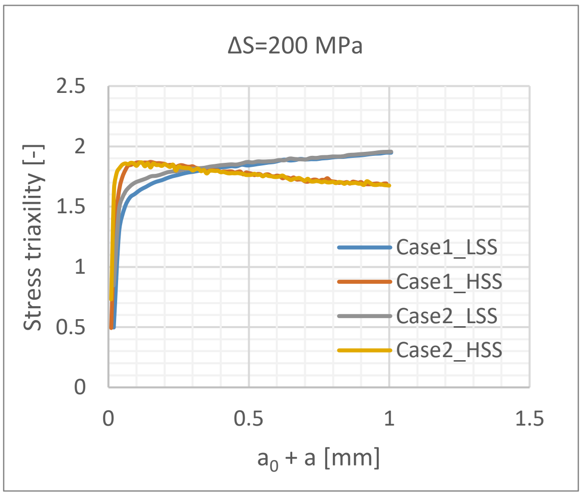

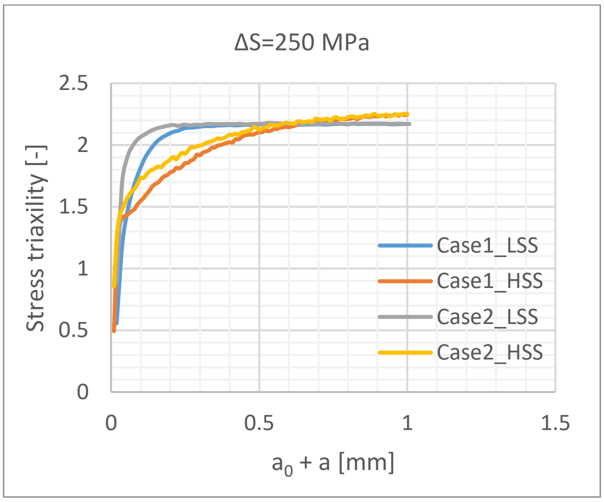

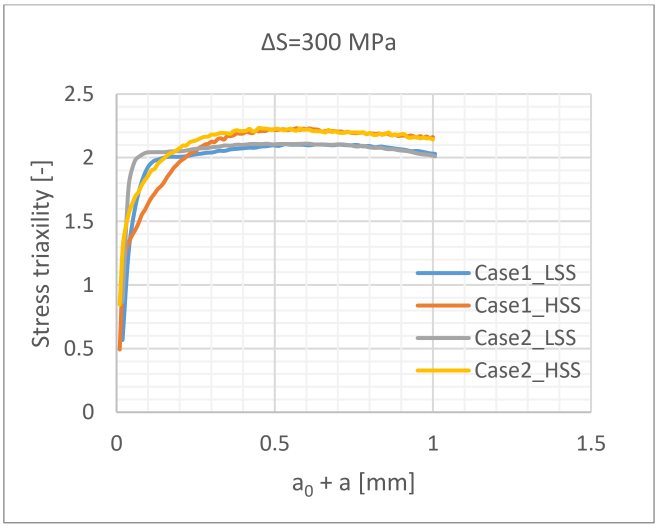

APPENDIX E – CRACK GROWTH RATES (CGR)

CGR under different load levels for same geometries vs effective crack length and stress intensity factor

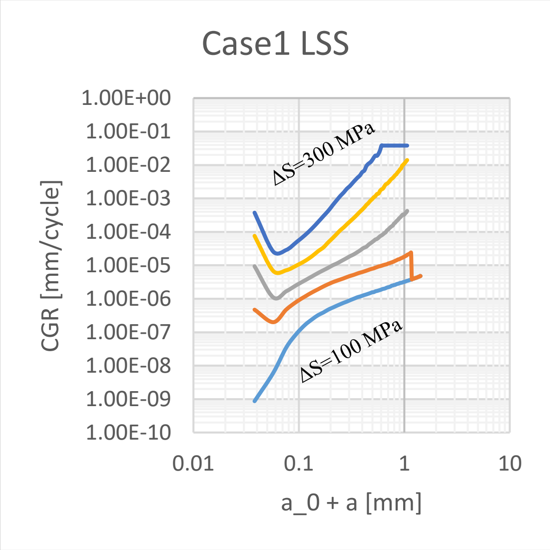

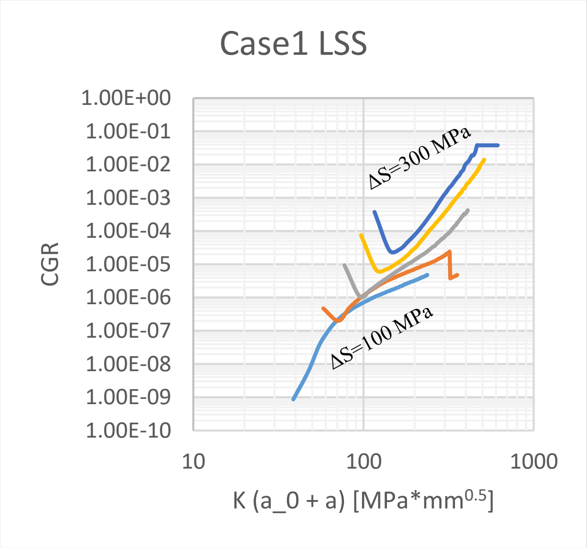

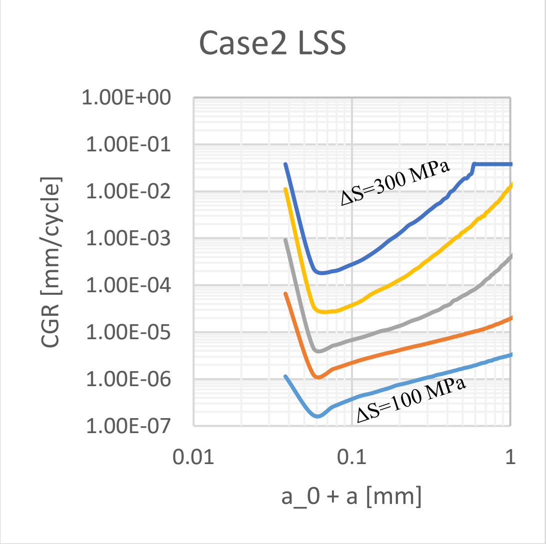

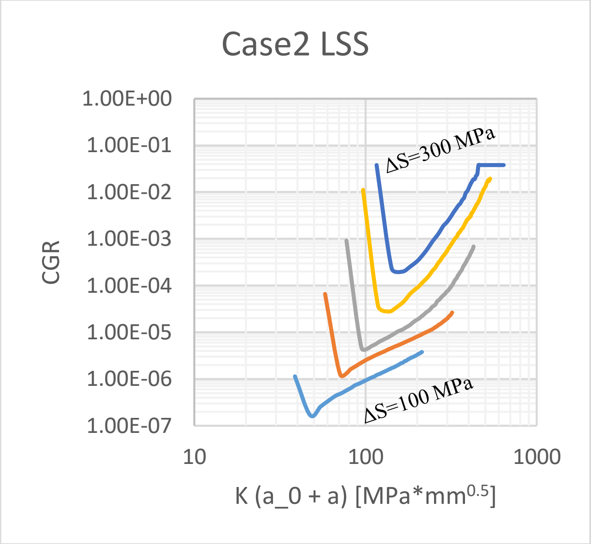

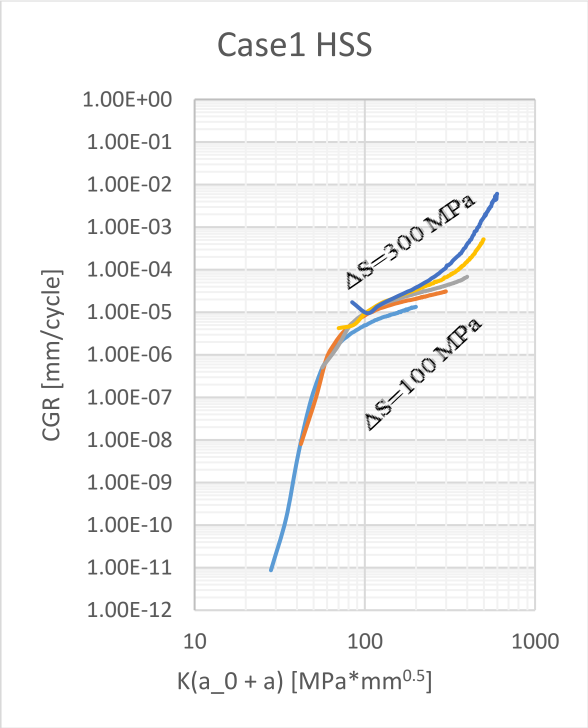
Case1 HSS

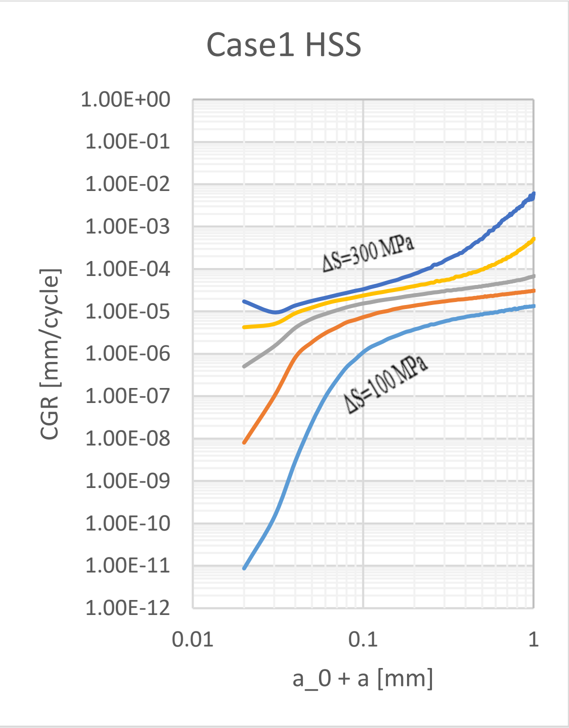
Case1 HSS

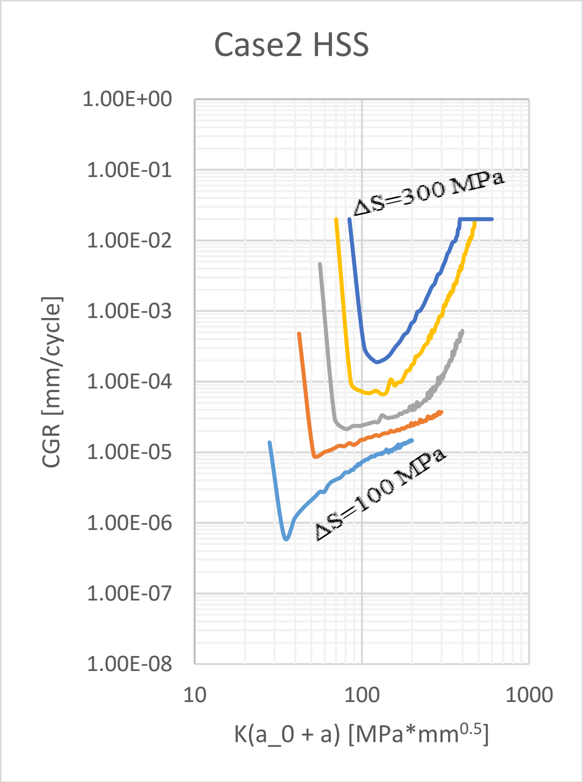
Case2 HSS

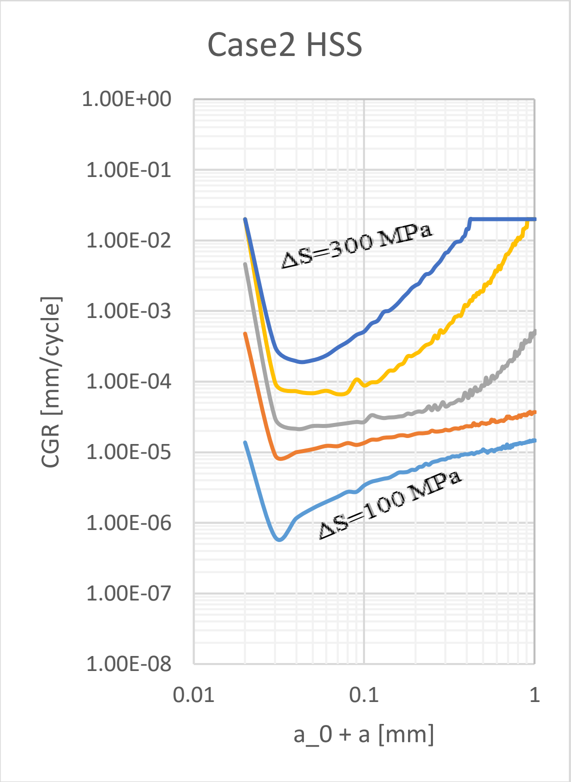
Case2 HSS

CGR under same load levels for different geometries vs effective crack length